

# Improvements on Mapping Soil Liquefaction at a Regional Scale

A dissertation  
submitted by

Jing Zhu

In partial fulfillment of the requirements  
for the degree of

Doctor of Philosophy

in

Civil & Environmental Engineering

TUFTS UNIVERSITY

February 2017

ADVISER: Professor Laurie G. Baise

## Abstract

Earthquake induced soil liquefaction is an important secondary hazard during earthquakes and can lead to significant damage to infrastructure. Mapping liquefaction hazard is important in both planning for earthquake events and guiding relief efforts by positioning resources once the events have occurred. This dissertation addresses two aspects of liquefaction hazard mapping at a regional scale including 1) predictive liquefaction hazard mapping and 2) post-liquefaction cataloging. First, current predictive hazard liquefaction mapping relies on detailed geologic maps and geotechnical data, which are not always available in at-risk regions. This dissertation improves the predictive liquefaction hazard mapping by the development and validation of geospatial liquefaction models (Chapter 2 and 3) that predict liquefaction extent and are appropriate for global application. The geospatial liquefaction models are developed using logistic regression from a liquefaction database consisting of the data from 27 earthquake events from six countries. The model that performs best over the entire dataset includes peak ground velocity (PGV),  $V_{S30}$ , distance to river, distance to coast, and precipitation. The model that performs best over the noncoastal dataset includes PGV,  $V_{S30}$ , water table depth, distance to water body, and precipitation. Second, post-earthquake liquefaction cataloging historically relies on field investigation that is often limited by time and expense, and therefore results in limited and incomplete liquefaction inventories. This dissertation improves the post-earthquake cataloging by the development and validation of a remote sensing-based method that can be quickly applied over a broad region after an earthquake and provide a detailed map of liquefaction surface effects (Chapter 4). Our method uses the optical satellite images before and after an earthquake event from the WorldView-2 satellite with 2 m spatial resolution and eight spectral bands. Our method uses the changes of spectral variables that are sensitive to surface moisture and soil characteristics paired with a supervised classification.

## **Acknowledgments**

First and foremost I want to thank my advisor, Professor Laurie Baise for all her contributions of time, ideas, and funding to make my Ph.D. experience productive and stimulating. The joy and enthusiasm she has for her research was always motivational for me. I would not have braved the journey to a Ph.D. without her immense patience and encouragement.

My sincere gratitude to the members of my committee, Laurie Baise, Elena Naumova, Magaly Koch, Eric Thompson, and Richard M. Vogel, for taking time and effort to read and approve my dissertation.

A special thanks to Eric Thompson for his endless input and advice on both research topics and career directions.

I would also like to thank my former office mates, Davene Daley, Bradford Berry, and James Kaklamanos, for all the good times and encouragement during later hours we shared together in the office room 318F.

This work was funded by the National Science Foundation under Grant No. 1300781, the United States Geologic Survey, Department of the Interior, under USGS award number G16AP00014 and FM Global; I gratefully acknowledge this support.

# Contents

<b>1</b>	<b>Introduction</b>	<b>2</b>
1.1	Liquefaction hazard mapping.....	2
1.2	Scope.....	4
<b>2</b>	<b>A geospatial liquefaction model for rapid response and loss estimation</b>	<b>6</b>
2.1	Introduction.....	7
2.2	Study areas.....	10
2.3	Explanatory variables .....	12
2.4	Database development .....	16
2.5	Model development.....	20
2.6	Results.....	22
2.7	Model Visualization.....	27
2.8	Port-au-Prince .....	31
2.9	Discussion.....	33
2.10	Conclusion .....	34
2.11	Acknowledgement .....	35
<b>3</b>	<b>An updated geospatial liquefaction model for global application</b>	<b>36</b>
3.1	Introduction.....	38
3.2	Data .....	41
3.3	Methods .....	50
3.4	Results.....	56
3.5	Discussion.....	75
3.6	Conclusion .....	78
3.7	Data and resources .....	79
3.8	Acknowledgement .....	80

<b>4</b>	<b>Mapping earthquake induced liquefaction surface effects from the 2011 Tohoku earthquake using satellite Imagery</b>	<b>81</b>
4.1	Introduction.....	83
4.2	Study area and data .....	86
4.3	Methods.....	89
4.3.1	Image preprocessing .....	89
4.3.2	Spectral variable selection.....	90
4.3.3	Change detection.....	91
4.3.4	Classification .....	93
4.3.5	Model development and accuracy assessment.....	94
4.3.6	Masking.....	95
4.4	Results and Discussion.....	96
4.4.1	Liquefaction characteristics .....	96
4.4.2	Change detection analysis.....	97
4.4.3	Maximum likelihood classification.....	101
4.4.4	Decision tree .....	102
4.4.5	Comparison of classifiers.....	103
4.4.6	Liquefaction maps.....	104
4.4.7	Discussion .....	106
4.5	Conclusion .....	110
<b>5</b>	<b>Summary</b>	<b>102</b>
	<b>Bibliography</b>	<b>116</b>

## List of Tables

1	Proxy-to-factor relationships .....	14
2	Summary of the earthquakes that contribute to the liquefaction database .....	20
3	Summary of region-specific models for Christchurch and Kobe .....	23
4	Summary of the pooled models (combining Kobe and Christchurch data) .....	25
5	Percentage of liquefaction occurrence within example probability ranges .....	27
6	Confusion matrices for thresholds of 0.1 and 0.2 for the regional model in Table 4 .....	27
7	Summary of earthquakes in the liquefaction database .....	43
8	Summary of all candidate explanatory variables .....	47
9	Coefficients of top performing coastal models and GLM-Zea15g. We heuristically assign zero to the predicted probability for both models when $PGV < 3$ cm/s. Similarly, we assign zero to the probability when $VS30 > 620$ m/s .....	64
10	Comparison of the AUCs of two updated models and GLM-Zea15g over individual earthquakes. Bolded numbers indicate the AUC for the better performing model in Model 1 and Model 2. When comparing three models, GLM-Zea15g outperforms the two updated models for six earthquakes .....	67
11	Confusion matrices for three thresholds (0.3, 0.4, and 0.5) for Model 1 presented in Table 4 .....	68
12	Parameters for relating model probabilities to areal liquefaction percent .....	78
13	Summary of the satellite images and their characteristics .....	88

14	Candidate spectral variables. The physical characteristics including soil characteristic and surface moisture that each variable is sensitive to are indicated by black circles.....	92
15	Accuracy assessment confusion matrix for the maximum likelihood classification .....	102
16	Accuracy assessment confusion matrix for the decision tree .....	103

## List of Figures

1	Topographic map of the Kobe, Japan region, showing earthquake epicenters (yellow stars), fault surface projections (black rectangles), and observed liquefaction features (red polygons). The faults represented by the two polygons are both part of the 1995 Hyogo-ken Nanbu source model from the ShakeMap Atlas (Wald 1996), while the 2003 earthquake is treated as a point source .....	11
2	Topographic map of the Kobe, Japan region, showing earthquake epicenters (yellow stars), fault surface projections (black rectangles), and observed liquefaction features (red polygons). The faults represented by the two polygons are both part of the 1995 Hyogo-ken Nanbu source model from the ShakeMap Atlas (Wald 1996), while the 2003 earthquake is treated as a point source .....	13
3	Topographic map of the Port-au-Prince, Haiti region, showing earthquake epicenters (yellow stars), fault surface projections (black rectangle; Allen et al. 2008), and observed ground failures (red circles) .....	13
4	Example measurement Map of candidate explanatory variables for the Christchurch region (a) Soil versus rock classification (b) VS30 (c) normalized distance (d) CTI (e) distance to river greater than order 3 (f) PGA.. .....	19
5	Maps of the observed liquefaction features and the predicted probability of liquefaction for (a) the Christchurch earthquake and (b) the Darfield earthquake. The predictions are computed with the coefficients reported for Christchurch Model 2 (Table 3) .....	21
6	Maps of the observed liquefaction features along with the predicted probability of liquefaction for the region-specific Christchurch model (Christchurch Model 2 from Table 3) for (a) the 1995 Hyogoken-Nanbu earthquake, and (b) the M 4.2 Kobe earthquake.....	24
7	Predicted probability of liquefaction using the best model derived from the combined Christchurch and Kobe data (regional model; Table 4) for (a) the Christchurch earthquake, (b) the Darfield earthquake, (c) the 1995 Hyogoken-Nanbu earthquake, and (d) the M 4.2 Kobe earthquake .....	26
8	Comparison of the ROC curves for the two liquefaction models summarized in Table 4. Points on earth ROC curve for thresholds of 0.1, 0.2, and 0.3 are labeled .....	28



9	The 2D image of the percentage of observed liquefaction with predicted probability contours from the regional model (Table 4) for (a) the Christchurch, (b) the Darfield, (c) the Hyogo-ken Nanbu, and (d) the 2003 Kobe earthquakes. The predicted probabilities assume CTI = 7 and VS30 = 200 m/s.....	29
10	The 2D image of the percentage of observed liquefaction in combined database with the predicted probability contours from the regional model (Table 4) when axes are (a) ND and PGA, (b) CTI and PGA, and (c) VS30 and PGA. For covariates not shown in each panel, the assumed values are: VS30 = 200 m/s, CTI = 7, and ND = 0.1 .....	30
11	Susceptibility map for Christchurch based on the regional model (Table 4). The values in the parentheses are X in equation (2) without the PGAM,SM term .....	32
12	Predicted probability of liquefaction from (a) the regional model and (b) the global model applied to the Port-au-Prince region. The models were developed from liquefaction observations in Kobe and Christchurch, and so this comparison checks the portability (or reliability) of the model.....	32
13	Maps of earthquakes in the liquefaction database from a) United States, b) Japan, c) New Zealand, and d) India, China and Taiwan .....	42
14	Percentage of liquefaction versus nonliquefaction as a function of PGV and VS30 for a) liquefaction events, b) events with insignificant or no liquefaction, and c) all events in the database .....	46
15	Maps of candidate explanatory variables: a) PGA, b) PGV, c) VS30 , d) dc, e) dr, f) dw, g) wtd, h) CTI, i) precip, and j) hwater for the San Francisco Bay area. PGA and PGV are shown for the 1989 Loma Prieta earthquake all other variables are event independent.....	51
16	Sampling nonliquefaction events using spatial buffers .....	52
17	Histograms of liquefaction (red bars) and nonliquefaction (green bars) and the probability of liquefaction observed from the data (gray circles) at intervals of a variable's value and the probability (blue line) predicted from a univariate model. The darkness of the gray dot increases with of the number of data points within the bin (the scale is different for each panel). In other words, the darkness of the point is an indication of weight.....	58
18	Observed percentage of liquefaction (colored bins) versus nonliquefaction as a function of dr and dc0.5 and comparison of probability contours (black lines) from a bivariate model a) without interaction term and b) with interaction term. Observed percentage of liquefaction (colored bins) versus nonliquefaction as a function of PGV and VS30 and comparison of probability contours (black lines) from a bivariate model c) without interaction term and d) with interaction term .....	61

19	Comparisons of ROC curves of GLM-Zeal5g and the best performing model (Model 1) with a one-to-one line representing random guessing .....	66
20	Probability maps predicted from the updated model (Model 1) for earthquakes in United States .....	70
21	Probability maps predicted from the updated model (Model 1) for earthquakes in Japan .....	71
22	Probability maps predicted from Model 2 for a) the 2008 Wenchuan, b) 1994 Northridge, c) 1999 Hector Mine, d) 1999 Chi-Chi, e) 2015 Nepal (Moss et al., 2015), and f) 2001 Bhuj earthquakes .....	72
23	Susceptibility maps for the San Francisco Bay, California area from a) the geospatial model (Model 1) and b) geology-based mapping (Witter et al., 2006). .....	74
24	Susceptibility maps for the Seattle, Washington area from a) the geospatial model (Model 1) and b) geology-based mapping (Palmer et al., 2004). .....	74
25	Sensitivity of ROC curves to a) spatial buffer and b) class imbalance with one to one lines (gray lines) representing random guessing .....	76
26	Areal percentage of liquefaction as a function of model probabilities. In each panel, the dots show the estimated liquefaction percent with 95% confidence intervals for binned predicted probabilities. Vertical lines indicate the bin boundaries. The black lines are curves fit to the data .....	77
27	a) Topographic map of the Urayasu city and b) Topographic map with mapped liquefaction polygons digitized from Toida and Yamazaki (2012). Site 1 is a parking lot in the Tokyo Disneyland. Site 2 is an open field near Akemi Elementary School .....	88
28	Illustration of a change vector (reproduced from Figure 1 in Malia, 1980) 92	
29	True color composite of the WV-2 image a) before the 2011 Tohoku earthquake, b) after the 2011 Tohoku earthquake, and c) overlain with validation data for a parking lot (lat 139.877, lon 35.629) in the Tokyo Disneyland. Liquefaction is indicated by the exposed dry sand that appears in yellow tones in the post-earthquake image .....	97
30	True color composite of the WV-2 image a) before the 2011 Tohoku earthquake, b) after the 2011 Tohoku earthquake, and c) overlain with validation data for an agricultural field (lat 139.917, lon 35.642). Liquefaction is indicated by the wet soil that appears in dark brown in the post-earthquake image .....	97
31	Maps of a) red, b) NIR, c) NDWI, c) brightness, d) greenness, f) wetness and g) mapped liquefaction from Toida and Yamazaki (2012) for the Disney Land parking lot site (Site 1). The high brightness areas and low wetness	

areas coincide with dry ejected sand on pavement. High means that the spectral variable value in the post-earthquake image is higher than that in the pre-earthquake image. Liquefaction at this site appears correlate to lower NDWI value and lower wetness value, which means low moisture content

- 99
- 32 Maps of a) red, b) NIR, c) NDWI, c) brightness, d) greenness, f) wetness and g) mapped liquefaction from Toida and Yamazaki (2012) for the agricultural field site (Site 2) . The low brightness and high wetness spots on the parking lot are coincident with wet ejected sand. High means that the spectral variable value in the post-earthquake image is higher than that in the pre-earthquake image. Liquefaction at this site appears correlate to higher NDWI value and higher wetness value, which means high moisture content  
100
- 33 Box and whisker plot of the change magnitude for liquefaction and nonliquefaction points for the entire dataset. In a box and whisker plot, the ends of the box are the upper and lower quartiles, and vertical black line inside the box marks the median. The whiskers are the two lines outside the box that extend to the highest and lowest observations. The vertical grey line indicates no change between the pre- and post-earthquake images.....101
- 34 Decision tree to classify liquefaction and nonliquefaction .....103
- 35 Maps of surface effects predicted using the proposed method in Urayasu City showing examples from three land cover types: road, parking lot, and bare soil.....105
- 36 Maps of subclasses from the branches (red=liquefaction branch separated by  $\text{change\_magnitude} \geq 2363$ ; yellow=liquefaction branch separated by  $\text{change\_wetness} < -634$  and  $\text{change\_magnitude} < 2363$  and  $\text{change\_magnitude} \geq 1101$ ; brown=liquefaction branch separated by  $\text{change\_NDWI} \geq 0.11$  and  $\text{change\_wetness} \geq -634$  and  $\text{change\_magnitude} < 2363$  and  $\text{change\_magnitude} \geq 1101$ ) of the decision tree for a) site 1 and b) site 2 .....105
- 37 Comparison of predicted liquefaction with digitized liquefaction from Toida and Yamazaki (2012) for three pavement areas .....107
- 38 Comparison of predicted liquefaction and mapped liquefaction form Toida and Yamazaki (2012) on a) post-earthquake WV-2 image and b) OpenStreetMap for an area with dense buildings. Same comparison on c) post-earthquake WV-2 image and d) OpenStreetMap for an area with tall buildings .....108
- 39 a) pre-earthquake WV-2 image, b) post-earthquake WV-2 image, and c) comparison of predicted liquefaction and mapped liquefaction from Toida and Yamazaki for an area where change of vegetation occurred between the pre- and post-earthquake images .....109

# Improvements on Mapping Soil Liquefaction at a Regional Scale

# **1 Introduction**

## **1.1 Liquefaction hazard mapping**

Earthquake induced soil liquefaction can lead to significant infrastructure damage due to lateral ground movements and vertical settlements. Mapping liquefaction hazard (e.g., liquefaction triggering and surface effects) at a regional scale is important in both planning for earthquake events and guiding relief efforts by positioning resources once the events have occurred.

Liquefaction hazard is generally evaluated on two scales: site specific scale and regional scale. On the site specific scale, the liquefaction hazard is most often evaluated using the simplified procedure based on soil data obtained from in-situ geotechnical soil testing as well as stratigraphy. The simplified procedure was originally developed using standard penetration test (SPT) N-values to quantify soil density (Seed and Idriss 1971), and has been adapted for cone penetration test (CPT) data (Juang and Jiang 2000; Robertson and Wride 1998), and shear-wave velocity ( $V_s$ ) data (Andrus and Stokoe II 2000). On a regional scale, liquefaction hazard is often mapped based on surficial geology maps. One of the first attempts at mapping the liquefaction susceptibility of soils was developed by Youd and Perkins (1978). The Youd and Perkins approach and subsequent liquefaction hazard mapping approaches (Youd and Hoose, 1978; Brankman and Baise, 2008) all use geologic characteristics such as age of deposition, depositional environment, geologic history and ground slope to classify surficial geologic units into quantitative susceptibility classes, such as high, moderate or low.

Liquefaction mapping can be classified into predictive liquefaction hazard mapping and post-liquefaction mapping catalogues. Prior to or immediately after an earthquake event, liquefaction hazard can be mapped using predictive methods. After a liquefaction event, liquefaction effects can be mapped and catalogued based on observations from field surveys or from remotely sensed images.

The objective of this dissertation is to improve current practice of regional liquefaction mapping in term of both predictive liquefaction hazard and post-liquefaction mapping catalogues. This is achieved by 1) the development of a geospatial prediction model for global application and 2) the development and validation of a mapping procedure that uses remotely sensed imagery to map liquefaction surface effects.

## 1.2 Scope

This dissertation is composed of three research papers. Following the introduction, Chapter 2 is a technical paper that proposes an approach that uses globally available geospatial proxies to predict the probability of liquefaction. The proposed method does not require detailed geologic maps and geotechnical data such as standard penetration test (SPT) or cone penetration test (CPT) results, and can be used for rapid response and loss estimation. The initial work summarized in Chapter 2 was based on mapped liquefaction surface effects from two earthquakes from Christchurch, New Zealand and two earthquakes from Kobe, Japan. Liquefaction surface effects were well mapped for each earthquake. Chapter 2 provides a proof-of-concept of the geospatial approach to regional liquefaction hazard mapping. Chapter 3 is a technical paper that extends the work in Chapter 2 and presents updated geospatial liquefaction models with improved performance and generality. This work improves on the previous model by 1) expanding the liquefaction database to 27 earthquake events across 6 countries, 2) addressing the sampling of nonliquefaction for incomplete liquefaction inventories, 3) testing interaction effects between explanatory variables, and 4) improving overall model performance. The updated models prove useful for global, near-real-time applications. Chapter 4 is a technical paper that proposes a method that applies change detection and classification techniques to remotely sensed imagery to document liquefaction surface effects. The motivation of the work presented in Chapter 4 comes from the challenge I faced in the development of the geospatial liquefaction models: the lack of spatially complete mapped liquefaction data catalogues. This work addresses the need for a low-cost and broadly applicable method to document liquefaction after an earthquake to complement and supplement field-based mapping. I develop a workflow that includes change detection using pre-event and post-event remotely sensed

imagery from the WorldView-2 satellite followed by a spectral classification, which can be used to detect liquefaction surface effects after an earthquake. The last chapter presents the summary and conclusions.



## 2 A Geospatial Liquefaction Model for Rapid Response and Loss Estimation<sup>1</sup>

### Abstract

We describe an approach to model liquefaction extent that focuses on identifying broadly available geospatial variables (e.g., derived from digital elevation models) and earthquake-specific parameters (e.g., peak ground acceleration, PGA). A key step is database development: we focus on the 1995 Kobe and 2010/2011 Christchurch earthquakes because the presence/absence of liquefaction has been mapped so that the database is unbiased with respect to the areal extent of liquefaction. We derive two liquefaction models with explanatory variables that include PGA, shear-wave velocity, compound topographic index, and a newly defined normalized distance parameter (distance to coast divided by the sum of distance to coast and distance to the basin inland edge). To check the portability/reliability of these models, we apply them to the 2010 Haiti earthquake. We conclude that these models provide first-order approximations of the extent of liquefaction, appropriate for use in rapid response, loss estimation, and simulations.

---

<sup>1</sup> Zhu, J., D. Daley, L. G. Baise, E. M. Thompson, D. J. Wald, and K. L. Knudsen (2015). A geospatial liquefaction model for rapid response and loss estimation, *Earthquake Spectra* 31, 1813-1837.

## 2.1 Introduction

Regional liquefaction hazard maps are valuable earthquake hazard products, yet they remain difficult to incorporate into rapid response, loss estimation, and emergency planning efforts. Current regional liquefaction mapping techniques rely heavily on surficial geologic maps to identify susceptible units (Youd and Perkins 1978, Holzer et al. 2006, 2009, Brankman and Baise 2008). Detailed (1:24K) Quaternary geology maps are an effective indicator of liquefaction in seismically active regions (Youd and Perkins 1978, Knudsen and Bott 2011). Some regions exposed to high seismic hazards have been able to invest in detailed geology-based liquefaction hazard maps, such as the San Francisco Bay Area (Holzer et al. 2006, 2009; Witter et al., 2006). But there are also many at-risk regions that have not been able to invest the resources necessary to develop these maps. Unfortunately, even where detailed geology-based liquefaction hazard maps exist, they are often not probabilistic and are not easily integrated into rapid response and loss estimation efforts. For rapid response and loss estimation, we need broadly available probabilistic liquefaction effects maps that can be integrated with event-specific shaking intensity maps such as those currently produced by the United States Geologic Survey (USGS) (ShakeMap; Worden et al. 2010) and produced immediately after an event occurs. Though some damaging earthquakes do not have losses due to liquefaction, it is useful to quickly identify those that do, and also to delineate the possible extent of the ground disruption. A map of areas of probable liquefaction is vital to critical lifeline utilities, port and harbor facilities, emergency managers, as well as financial industries (particularly insurance and reinsurance), since port and underground infrastructure damage can be both costly and can impact regional economies.

Throughout this paper, we use the term liquefaction to mean surface manifestations of liquefaction, and our goal is to predict the areal extent of liquefaction. Recent work by Knudsen and Bott (2011) investigated the use of geologic and geomorphic layers for predicting liquefaction and found that liquefaction

sites have common attributes such as geologic age, depositional environment, slope, elevation, and distance to water body. Specifically, liquefaction tends to occur in young sediments, near water bodies, and on low, flat ground. The work by Knudsen and Bott (2011) was primarily based on a compilation of liquefaction case histories collected by researchers developing liquefaction models from site-specific measurements (e.g., Cetin 2000, Olson 2001, Moss 2003, Faris 2004, Kayen 2011). Knudsen and Bott (2011) found that 90% of liquefied sites in seismically active areas were located in geologic materials that were either Historical or Late Holocene surficial deposits; 73% of liquefied sites were either in artificial fill or near streams; and 67% of liquefied sites were at less than 10 m elevation. While the Knudsen and Bott (2011) study provided quantitative support for geospatial liquefaction variables, the analysis had two deficiencies that we overcome in this paper. First, the case studies over-sample liquefaction cases (i.e., there are few observations of non-liquefaction) resulting in a sampling bias. Oommen et al. (2011) demonstrated that the probabilities that result from logistic regression are biased when the data exhibit a sampling bias (i.e., the data do not uniformly sample the population). Second, their analysis did not provide a predictive model.

We address the sampling bias issue discussed above by developing a liquefaction database from datasets that uniformly sample regions where liquefaction has and has not occurred. This marks a shift in liquefaction model development, which to date has focused on case history databases that are biased toward observations of liquefaction occurrence. This shift in modeling philosophy is possible because recent post-earthquake data collection efforts combine field mapping observations with satellite imagery to create continuous maps of liquefaction surface effects (e.g., Cubrinovski et al. 2011, Green et al. 2011b). An early example of this was the 1995 Hyogo-ken Nanbu earthquake in Kobe, Japan where liquefaction was documented continuously throughout the greater Kobe region in terms of observed surface effects as well as horizontal and vertical displacements (Hamada et al. 1995).

To develop a global geospatial liquefaction model, we identify and validate first-order proxies from broadly available geospatial data to obtain in-situ soil properties, such as the degree of saturation (or water table depth), depositional age, relative density, and grain size. Compared to the information that is available for a site-specific liquefaction assessment, the explanatory variables that we consider in this paper are relatively coarse proxies of the underlying physical parameters used to accurately model liquefaction. Thus, we do not expect to achieve a model that can explain the liquefaction features at a site-by-site scale. Rather, we seek a model that is unbiased with respect to the areal extent of liquefaction, which can therefore identify broad zones of heightened likelihood of liquefaction. This approach to liquefaction modeling is motivated by the need for a globally applicable liquefaction model and implicitly acknowledges that in order to achieve the desired spatial coverage some precision must be sacrificed relative to a traditional site-specific liquefaction analysis (e.g., Youd et al. 2001, Idriss and Boulanger 2008) or a detailed geologic analysis (e.g., Holzer et al. 2006, 2009; Witter et al., 2006).

In this paper, we model liquefaction data from the 2010-2011 Christchurch earthquakes and the 1995 Hyogo-ken Nanbu earthquake. Our modeling strategy is to develop the model in Christchurch and Kobe where we have relatively complete maps of liquefaction and then to check the portability (or reliability) of the model by applying it to the 2010 Port-au-Prince, Haiti earthquake. In Haiti, some liquefaction occurrences have been mapped, though the presence/absence of liquefaction is not known with certainty throughout much of the region. We begin by reviewing the different datasets included in our analysis and then we discuss the explanatory variables that we compute for each region. We then describe the general modeling strategy, present the results of our analysis, and discuss the uses and limitations of the resulting models.

## 2.2 Study Areas

Two of the three regions that we study in this paper are selected because the extent of liquefaction during recent earthquakes was accurately mapped with a combination of field mapping and aerial/remote imagery analysis. Christchurch, New Zealand and Kobe, Japan were both extensively mapped in a manner that constrained the spatial extent of liquefaction and nonliquefaction. We also include data from Port-au-Prince, Haiti, which was mapped in a more limited way, and so we only use these data to check the portability (or reliability) of our model (i.e., the data in Port-au-Prince are not used in the model building stage).

The city of Christchurch is located in the Canterbury Plains on the east coast of the South island of New Zealand (Figure 1). The Canterbury Plains are bounded by the foothills of the Southern Alps to the northwest (outside of map extent) and Banks Peninsula to the southeast; Banks Peninsula was formed by an extinct volcanic complex. The region originally included swamplands, beach dune sand, riverine deposits, estuaries, and lagoons that were drained during European settlement (Brown and Weeber 1992, Brown et al. 1995). Consequently, the near-surface soil is mainly inter-bedded, loose Holocene aged silt, sand, and gravel (Green et al. 2011b). The groundwater table approaches the ground surface near the coast and becomes gradually deeper toward the west. As a result, the groundwater table in the Christchurch city region is shallow (within 1.5 to 2.0 m of the ground surface; Cubrinovski et al. 2011), and the groundwater table in Darfield is deep (greater than 50 m; Environment Canterbury Regional Council 2012). Figure 1 displays the surface projection of the fault planes and epicenters for the two earthquakes that caused liquefaction in this region in 2010-2011. The epicenter of the **M** 7.0 September 3, 2010 earthquake was near the town of Darfield, 40 km west of Christchurch. Although this earthquake ruptured multiple fault segments (Elliott et al. 2012), we use a simplified single fault model (Allen et al. 2008) for the analysis in this paper. Figure 1 also includes the mapped extent of liquefaction for this event, which shows that no

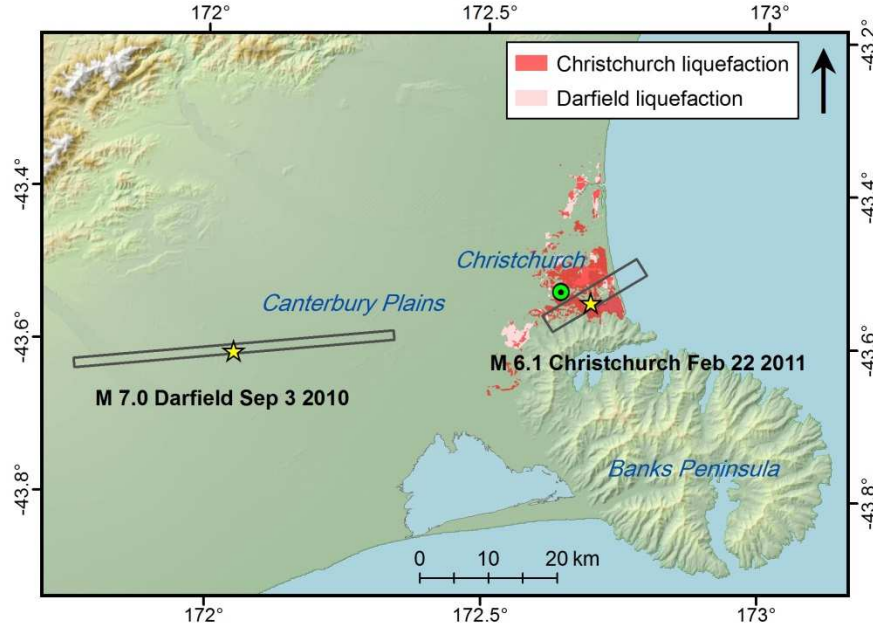


**Figure 1.** Topographic map of the Christchurch, New Zealand region, showing the earthquake epicenters (yellow stars), fault surface projections (black rectangles), and observed liquefaction features (colored polygons). We use the simplified fault model from Allen et al. (2008) for the 2010 earthquake and the Beavan et al. (2011) fault model for the 2011 earthquake.

liquefaction was observed near the source, whereas liquefaction was observed in the Christchurch region. The epicenter of the **M** 6.1 February 22, 2011 earthquake was in Port Hills, 10 km southeast of the center of Christchurch. Although the Christchurch event has a smaller magnitude as compared to the Darfield event, it resulted in more extensive liquefaction throughout the Christchurch region, as shown in Figure 1, due to the closer proximity of the epicenter to the city, and thus the stronger ground motion.

Relative to Christchurch, Kobe, Japan is located in a narrow (2-3 km wide) portion of the Osaka sedimentary Basin (Figure 2). It is confined between the Rokko Mountains and Osaka Bay. The sediment age generally decreases toward the coast and the coastal edge has been extensively filled, including several man-made islands such as Port and Rokko Islands. Most of the artificial land consists of sandy hydraulic fill (Huzita and Maeda 1985). The 1995 **M** 6.9 Hyogo-ken Nanbu earthquake caused extensive liquefaction of the artificial fill, greatly affecting port operations and commerce. We included a second, smaller **M** 4.2 Kobe event in our analysis, to ensure

that our dataset includes a set of observations from an event that did not cause liquefaction. This event occurred 5 km from Kobe on October 8, 2003. The epicenters of both events and the surface projection of the fault for the 1995 event (Wald 1996) are shown in Figure 2.

The city of Port-au-Prince lies in the Cul-de-Sac plain (Figure 3), a nearly flat coastal plain (about 12 km wide) that is underlain by alluvial and marine-estuarine sediments, and reclaimed land (Lambert et al. 1987). The plain is confined between two mountain ranges. The January 12, 2010 **M** 7.0 earthquake struck the Port-au-Prince region of Haiti 20 km west of the city of Port-au-Prince. The earthquake caused extensive damage, including liquefaction effects at the Port of Port-au-Prince. Many manifestations of liquefaction were observed in the vicinity of the North Wharf and in the alluvial plain surrounding the city of Leogane (Rathje et al. 2010). Post-earthquake geotechnical reconnaissance (Rathje et al. 2010, 2011, Green et al. 2011a) documented the locations of liquefaction-related ground failures shown in Figure 3. These observations were primarily along the coast and along the Riviere Grise in Port-au-Prince. In contrast to Kobe and Christchurch, the spatial extent of liquefaction is not mapped in Port-au-Prince; the mapped points are known ground failures, but we cannot assign spatial extent to the observed features or assess that failures did not occur in other locations.

## **2.3 Explanatory Variables**

There are three broad factors that contribute to the likelihood of liquefaction (Youd and Perkins 1978, 1987, Ishihara 1996): density, saturation (or water table depth), and dynamic load on the soil from an earthquake (both intensity and duration). Typically, the first two factors are measured on a site-specific basis using geotechnical logs and penetration data. However, in order to develop a model that is applicable for rapid response maps, loss estimation, and earthquake simulations, we must use simple proxies for these soil characteristics. In addition to the three primary factors listed above, liquefaction analyses often include the grain size distribution and geotechnical

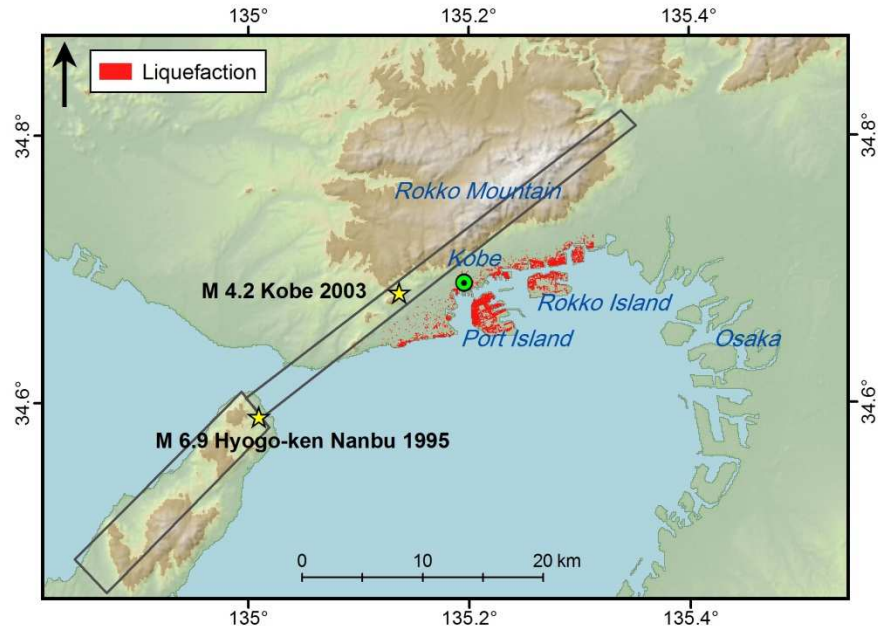


**Figure 2.** Topographic map of the Kobe, Japan region, showing earthquake epicenters (yellow stars), fault surface projections (black rectangles), and observed liquefaction features (red polygons). The faults represented by the two polygons are both part of the 1995 Hyogo-ken Nanbu source model from the ShakeMap Atlas (Wald 1996), while the 2003 earthquake is treated as a point source.

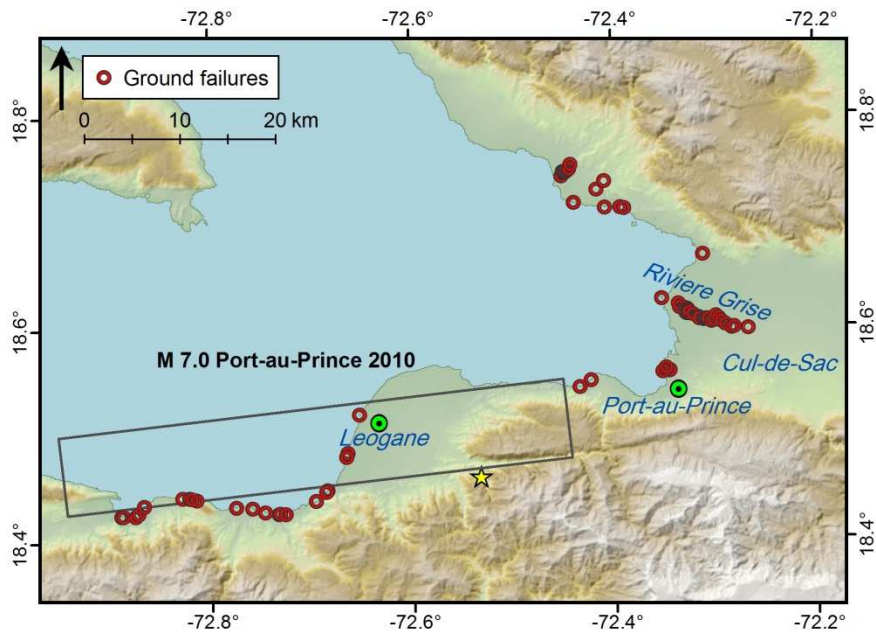


**Figure 3.** Topographic map of the Port-au-Prince, Haiti region, showing earthquake epicenters (yellow stars), fault surface projections (black rectangle; Allen et al. 2008), and observed ground failures (red circles).



index properties, such as plasticity index and water content. In this paper, we do not attempt to characterize these factors as part of the geospatial liquefaction model.

Table 1 summarizes the relationships between the geospatial proxies (the rows of the table) and the physical factors that affect liquefaction (columns). The dots in the cells indicate if the proxies are considered appropriate for the different factors. Solid dots indicate the factor/proxy pairs that we focus on in this paper. Note that many of the topographic/geospatial parameters may be predictors of both soil and hydrologic conditions. We discuss these factors and their inclusion in the modeling process in detail below.

**Table 1.** Proxy-to-factor relationships.

Proxy	Density	Saturation	Loading
Roughness (rock vs soil)	●		
$V_{S30}$ (from topographic slope)	●		
$d_c$	●	●	
ND	●	●	
Soil type (from satellite imagery)	○		
$d_{wb}$	○	○	
$z_{wb}$	○	○	
$d_r$	●	●	
CTI		●	
PGA from GMPE			●
PGA from ShakeMap			●
PGV from ShakeMap			○
PGA from simulations			○
Moment magnitude			○
Magnitude Scaling Factor (MSF)			●

● Relationship used in this paper.

○ Relationship not investigated in this paper.

We map soil density using a two-step process. The first step differentiates between soil and rock. Much of the area that experiences strong shaking is rock, where liquefaction cannot occur, and therefore it is important to handle the rock differently than soil. We use surface roughness to differentiate soil from rock, although topographic slope could also be used for this classification. We estimate the roughness as the standard deviation of the elevation in a 3x3 pixel window, which is a modification of the Riley et al. (1999) method.

The second step is to characterize soil density, which is related to the shear-wave velocity ( $V_s$ ) and geologic age. These two parameters are also not widely available at the global scale. Previous work by Wald and Allen (2007) and Allen and Wald (2009) found that topographic slope can be used as a first order proxy for the average  $V_s$  in the upper 30 m ( $V_{s30}$ ). We therefore adopt  $V_{s30}$  derived from the Wald and Allen (2007) approach as a soil density proxy. Within coastal regions, the distance from the coast ( $d_c$ ) generally correlates with the age of the sediment because older and denser sediments are generally located farther from the coast due to the transport and depositional process of marine sediments. Young, loose sediment is also found along large rivers. Because coastal sedimentary plains exhibit large variations in extent, we normalize the distance to the coast by the size of the basin; we define normalized distance (ND) as the distance to the coast divided by the sum of the distance to the coast and the distance to the inland edge of the sedimentary basin. We use ND as a second proxy for soil density/age, and it could also be considered a proxy for saturation because the water table generally becomes shallower at shorter distances to the coast.

Because we aim to develop a model that uses broadly available data, we do not consider parameters derived from surficial geology or geotechnical data. Although there is the potential that remotely sensed data can identify soil type (Kothari and Islam 1999, Chang and Islam 2000), we do not include a proxy for soil type in the model that we present in this paper.

Characterizing the degree of saturation or depth of the water table is one of the most important factors in predicting liquefaction of soils. Knudsen and Bott (2011) identified several candidate proxies for soil saturation, though most can simultaneously be considered proxies for density. The most promising proxies for saturation were: 1) distance to the closest water body ( $d_{wb}$ ), and 2) elevation above the closest water body ( $z_{wb}$ ). Since the distance to the coast is already included in the definition of ND, we include distance to river ( $d_r$ ) as a separate proxy. Additionally,

we include the compound topographic index (CTI; Beven and Kirkby 1979) as a proxy for saturation, which has been widely used in hydrology as a proxy for soil saturation. CTI is defined as the natural logarithm of the ratio of contributing area to the tangent of slope (Moore et al. 1991). In order to compute the contributing area, the flow direction at each pixel is estimated from the digital elevation model (DEM). The contributing area at a specific location is the number of upstream pixels. Thus, CTI increases on flat areas with large contributing areas.

We approximate the effects of earthquake loading with the peak ground acceleration (PGA). We consider two different estimates of PGA: 1) from a ground motion prediction equation (GMPE), a finite fault model, and  $V_{S30}$ , denoted as  $PGA_G$ ; and 2) from ShakeMap, which incorporates macroseismic data as well as available ground motion records with GMPE estimates (Worden et al. 2010), denoted  $PGA_{SM}$ . Earthquake duration is also an important factor for liquefaction. In other liquefaction models (e.g., Youd et al. 2001) the magnitude scaling factor (MSF) has been used as a proxy for earthquake duration. Due to the current limitations of our database (we only have a limited number of events to sample duration effects), we decided not to constrain the duration effects from our database, but to use the equation in Youd et al. (2001):

$$MSF = 10^{2.24/M^{2.56}} . \quad (1)$$

The inverse of MSF is termed the magnitude weighting factor (MWF; Chen and Harmsen, 2012). Others have used the term duration weighting factor (DWF), however we prefer the term MWF because the right-hand side of equation 1 includes  $M$  and not duration. To account for duration, we define a magnitude weighted PGA:  $PGA_{M,SM}$  is the product of MWF and  $PGA_{SM}$ ; and  $PGA_{M,G}$  is the product of MWF and  $PGA_G$ .

## 2.4 Database Development

Liquefaction surface effects are often mapped during geotechnical reconnaissance

conducted following an earthquake (e.g., Allen et al. 2010, 2011, Rathje et al. 2010). When field observations are supplemented with satellite imaging and remote sensing techniques, continuous areas of liquefaction can be mapped. Where liquefaction extent is mapped (e.g., Christchurch and Kobe events), we rasterize the polygons to 100 m pixels, and a pixel is classified as liquefaction if at least 30% of it liquefied. This threshold is selected to retain the same liquefaction to nonliquefaction ratio before and after rasterization. We add the candidate explanatory variables (see Table 1) as additional columns to the database. We derive explanatory variables from Shuttle Radar Topography Mission (SRTM) DEMs (Farr and Kobrick 2000, Werner 2001) with both 3 arc-sec (90 m) resolution and 30 arc-sec (900 m) resolution. Throughout this paper 3c refers to 3 arc-sec resolution and 30c refers to 30 arc-sec resolution.

We use the  $V_{S30}$  values provided by the global  $V_{S30}$  server (Wald and Allen 2007) at the 30c resolution. For the Christchurch region, the soil-versus-rock classification (based on the 3c roughness) is displayed in Figure 4a, the slope-based  $V_{S30}$  values are displayed in Figure 4b, and ND is displayed in Figure 4c. We add the 30c CTI from the USGS Hydro1k database (USGS, 1996) to the database, which is displayed in Figure 4d. Pixels that are partially located in the ocean are undefined in the Hydro1k database. Therefore, we fill the undefined pixels with the mean value of adjacent pixels. To provide a higher resolution alternative, we compute CTI from the 3c resolution DEM with the algorithm described previously.

The stream networks are computed from the DEM with the Tarboton et al. (1991) method. The flow direction and flow accumulation are computed after the DEM is corrected for pits and depressions. Stream networks are defined from flow accumulation assuming a threshold accumulation of  $4.5 \text{ km}^2$ . We apply the Strahler (1952) stream ordering method (based on the number of contributing branches in the stream network) and compute the distance to rivers ( $d_r$ ) for different minimum stream orders. For example,  $d_{r,3}$  is the distance to a stream of order three or greater, and is displayed in Figure 4e. To provide physically meaningful limits on the extent of the

DEM used to compute the higher resolution hydrologic parameters, we clip the DEM with the drainage basin boundaries in the USGS Hydro1k database (USGS, 1996).  $PGA_{SM}$  is shown for the Christchurch event in Figure 4f.

We compute the  $PGA_G$  with a GMPE appropriate for each region and a finite fault model for each event. For the Christchurch region, we use the Bradley (2010) model because it was developed specifically for the Christchurch region and finite fault models to compute the distance measures (Beavan et al. 2011, Allen et al. 2008). For both the Kobe and Port-au-Prince regions, we compute  $PGA_G$  with the Boore and Atkinson (2008) equations with the Atkinson and Boore (2011) update and the finite fault models reported in the ShakeMap Atlas (Allen et al. 2008; Wald 1996). The slope-derived  $V_{S30}$  are used for all  $PGA_G$  calculations.

The four earthquakes that are included in this database are sampled on a 100 m grid within the mapped region for each event and result in 183,887 data-associated pixels; 13,177 of these pixels are classified as locations of liquefaction occurrence. The number of rows (pixels) in the database is a function of the arbitrarily chosen grid size. Table 2 summarizes the number of pixels, areal percent of liquefaction, and areal percent of observations on soil for each event. We added the explanatory variables to this database with automated and semi-automated scripts in Python and R to ensure consistency and so that new earthquakes can be added to the database efficiently.

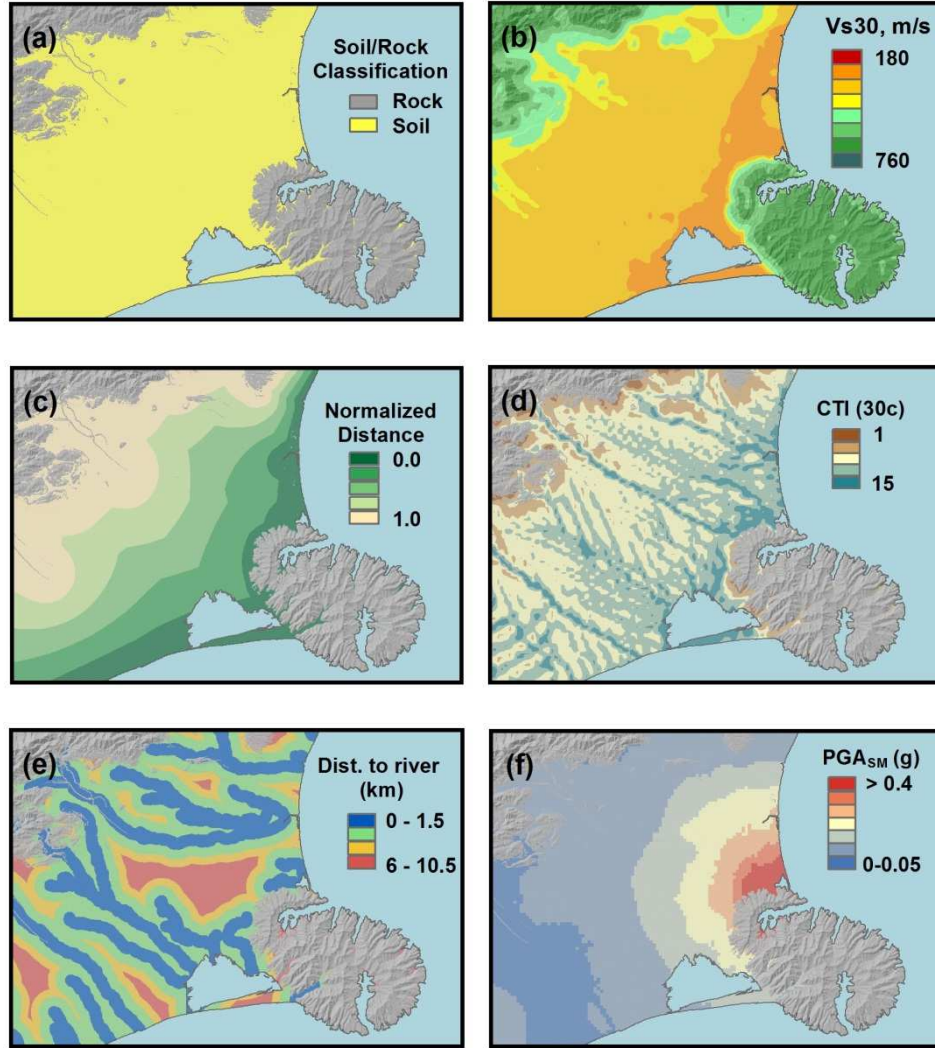


**Figure 4.** Map of candidate explanatory variables for the Christchurch region (a) Soil versus rock classification (b)  $V_{s30}$  (c) normalized distance (d) CTI (e) distance to river greater than order 3 (f) PGA.

The number of rows (pixels) in the database is a function of the arbitrarily chosen grid size. Table 2 summarizes the number of pixels, areal percent of liquefaction, and areal percent of observations on soil for each event. We added the explanatory variables to this database with automated and semi-automated scripts in Python and R to ensure consistency and so that new earthquakes can be added to the database efficiently.

**Table 2.** Summary of the earthquakes that contribute to the liquefaction database.

Earthquake	Year	Magnitude	Mapped Area (km <sup>2</sup> )	Percentage of liquefaction	Percentage of soil
Christchurch	2011	6.1	575.9	13.5	82.3
Darfield	2010	7.0	1060.6	4.0	90.4
Hyogo-ken Nanbu	1995	6.9	101.2	11.3	68.4
Kobe	2003	4.2	101.2	0.0	68.4

## 2.5 Model Development

The explanatory variables summarized in Table 1 include both continuous and categorical variables while liquefaction occurrence is binary. Logistic regression is a convenient approach for fitting a model that describes the relationship between a binary outcome and a set of continuous or categorical independent variables. For model development, we follow the generalized linear model framework with the logit link function, yielding

$$P(X) = \frac{1}{1+e^{-X}}, \quad (2)$$

where  $X = \beta_0 + \beta_1 x_1 + \dots + \beta_k x_k$  is the set of  $k$  explanatory variables and  $P(X)$  is the probability of liquefaction given the predictor variable. The regression coefficients  $\beta_0, \beta_1, \dots, \beta_k$  are estimated with the maximum likelihood method. For the regression, we include only those data classified as soil (see Figure 5a) and assign the probability of liquefaction to zero apriori for locations classified as rock. Akaike's information criterion (AIC; Akaike, 1973) is useful for guiding model selection

$$AIC = -2 \ln(L) + 2p, \quad (3)$$

where  $L$  is maximized likelihood function, and  $p$  is the number of estimated parameters. AIC is a relative value and should only be used to compare models that are fit to the same data set. Lower values of AIC indicate a better or more useful model. The basic idea is that the negative log likelihood is penalized by the number of parameters to guard against the tendency to overfit the data with unwarranted parameters.

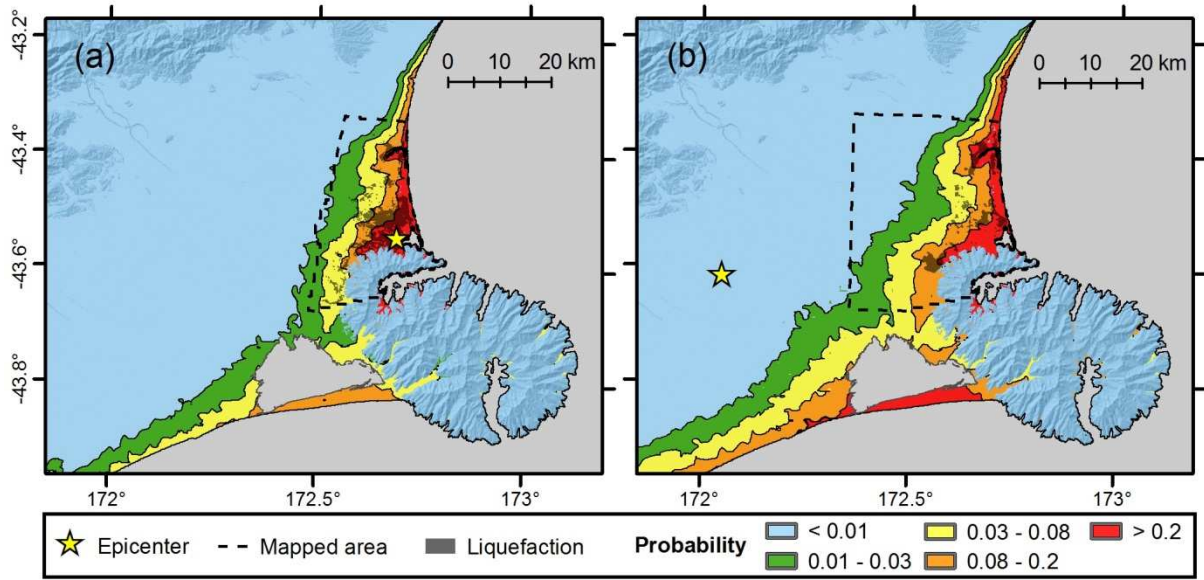


**Figure 5.** Maps of the observed liquefaction features and the predicted probability of liquefaction for (a) the Christchurch earthquake and (b) the Darfield earthquake. The predictions are computed with the coefficients reported for Christchurch Model 2 (Table 3).

We evaluate the significance of the regression coefficients with the Wald test statistics (Z value), which is the ratio of the estimate of the coefficient to its standard error. The Wald test statistic follows the standard normal distribution under the hypothesis that an individual coefficient is zero. Because the Wald test follows a normal distribution, we can conclude that model parameters are significantly different than zero at the 95% confidence level if the absolute value of the test statistic is greater than two.

With a binary response variable, plots of observed versus predicted values, or plots of residuals as a function of various explanatory or response variables are not easy to interpret because the predictions are probabilities while the observations are binary. One approach to addressing this problem is to select a threshold probability value to convert the predicted probabilities into binary classifications (probabilities greater than the threshold are a classification of liquefaction occurrence). Useful performance metrics for binary classifications include the true positive rate (TPR) and the false positive rate (FPR), which can be computed for an assumed threshold. TPR is defined as the ratio of positive cases (i.e., liquefaction occurrence) that were correctly



predicted to the total number of positive cases. FPR is defined as the ratio of negative cases (i.e., liquefaction nonoccurrence) that were falsely predicted to the total number of negative cases. Receiver operating characteristic (ROC) curves plot TPR versus FPR (Swets 1973). To construct the ROC curves, we loop over thresholds from zero to one, and compute TPR and FPR for each threshold. A model that perfectly predicts the binary response would have  $TPR = 1$  and  $FPR = 0$ . The closer the ROC curve comes to this ideal case (i.e., the top-left edge of the plot), the better the model performance. Thus, the area under the ROC curve (AUC) is a scalar measure that quantifies the accuracy of the probabilistic classifier, because as the AUC increases the ROC curve approaches the top-left edge of the plot. The AUC limits are from 0.5 (random classification) to 1.0 (perfect accuracy).

Our modeling approach uses a combination of goodness-of-fit parameters such as AIC, p-values, and AUC and our knowledge of the physical process that leads to liquefaction to determine which explanatory variables to include. For example, we did not include elevation as an explanatory variable although its p-value and the model's AIC indicate that it is statistically significant because elevation would not extrapolate well outside of coastal environments. Additionally, we give preference to explanatory variables that perform well when regressed in Christchurch and assessed in Kobe (i.e., the analysis of region-specific models in the next section).

## **2.6 Results**

In order to understand regional and event specific differences in model development, we begin by developing region-specific models. For the Christchurch region, we include both the Darfield and Christchurch earthquakes. Most observed liquefaction features during the Christchurch event were within 12 km of the coast and where PGA was high (0.2 g-0.6 g). In contrast, the epicenter of the Darfield event was 52 km west of Christchurch and yet liquefaction occurred along the coast at a distance of over 40 km from the epicenter where PGA is relatively low (0.1 g-0.2 g). This indicates that

the liquefaction pattern in this region is strongly controlled by soil properties. If we were to only include the Christchurch event in the regression, the resulting model would be largely driven by PGA because the liquefaction features all occurred in locations that experienced the largest PGAs.

In the subsequent discussion, we define the top performing model as the one with the lowest AIC. We consider several candidate models in each region, with a focus on simple four-parameter models. We also wish to initially focus on comparisons of different soil proxies, and so we only consider  $\text{PGA}_{\text{M,SM}}$  as the intensity covariate. Table 3 shows the parameters and coefficients for the top three four-parameter models for each region. Comparisons of regression results with PGA and  $\ln(\text{PGA})$  show that  $\ln(\text{PGA})$  performs better. Similarly,  $\ln(V_{S30})$  outperforms  $V_{S30}$ . The explanatory variables of the top performing four-parameter model in Christchurch are  $\ln(\text{PGA}_{\text{M,SM}})$ ,  $d_{r3}$ , and ND. A quick consistency check is to inspect the sign of the estimated coefficients to see that the resulting relationship with the likelihood of liquefaction is correct: the likelihood of liquefaction decreases with increasing values of  $V_{S30}$ , ND, and  $d_r$ ; the likelihood of liquefaction increases with increasing values of CTI and  $\text{PGA}_{\text{M,SM}}$ .

**Table 3.** Summary of region-specific models for Christchurch and Kobe.

		Model 1		Model 2		Model 3	
Christchurch	Intercept	2.053	Intercept	0.316	Intercept	25.45	
	ln(PGA <sub>M, SM</sub> )	1.267	ln(PGA <sub>M, SM</sub> )	1.225	ln(PGA <sub>M, SM</sub> )	2.476	
	$d_{r3}$	-0.239	CTI (30c)	0.145	$d_{r3}$	-0.323	
	ND	-9.191	ND	-9.708	ln( $V_{S30}$ )	-4.241	
Kobe	Intercept	-0.780	Intercept	1.608	Intercept	11.78	
	ln(PGA <sub>M, SM</sub> )	1.813	ln(PGA <sub>M, SM</sub> )	1.836	ln(PGA <sub>M, SM</sub> )	1.678	
	CTI (30c)	0.287	$d_{r3}$	-0.028	CTI (30c)	0.669	
	ND	-8.958	ND	-9.993	ln( $V_{S30}$ )	-2.936	

Checking the portability or reliability of a model is an important step because it evaluates model performance with a new scenario. This directly addresses whether or not the model is overfit to the limited available data. When we apply the region-specific Christchurch models to Kobe, Model 2 outperforms Model 1 and so we

conclude that the  $d_{r3}$  term works well in Christchurch but that CTI is more stable across different regions. Therefore, we prefer Model 2. Figure 5 gives the maps of the predicted probability of liquefaction for the Christchurch region from the preferred four-parameter model, while Figure 6 gives the probabilities of this model in Kobe. The pattern of liquefaction is well represented by the Christchurch model for the Hyogo-ken-Nanbu earthquake (Figure 6a) even though the liquefaction occurred in very different sediments in Kobe (fill) than in Christchurch (native soils) and the scale and shape of the coastal sedimentary basins are significantly different. Additionally, the overall probabilities are much smaller for the small Kobe event for which no liquefaction was observed (Figure 6b).

In Christchurch, many of the liquefaction features were observed over historic river channels (Orense et al., 2011). The location of these channels is a strong geologic predictor of liquefaction. The  $d_r$  parameter that we consider in this paper is based on river networks predicted from the DEM rather than mapped current or historic river channels and therefore cannot provide a model that accounts for historic river channels.

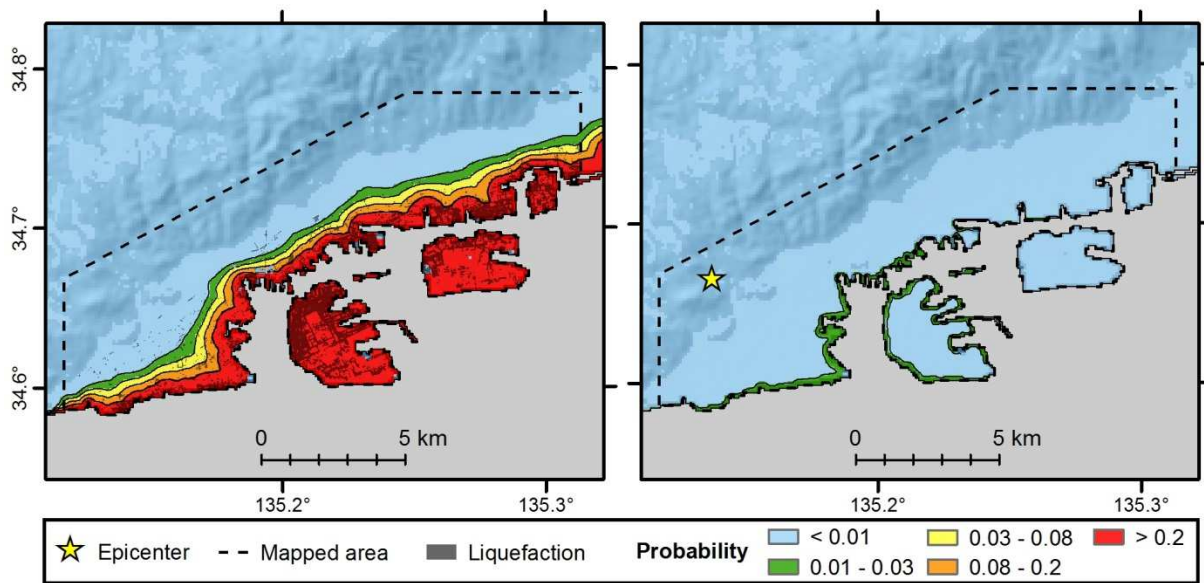


**Figure 6.** Maps of the observed liquefaction features along with the predicted probability of liquefaction for the region-specific Christchurch model (Christchurch Model 2 from Table 3) for (a) the 1995 Hyogoken-Nanbu earthquake, and (b) the M 4.2 Kobe earthquake.

To strengthen the model and optimize the coefficients across the regions, we combined the Christchurch and Kobe datasets, and used the combined datasets in regression to develop two different pooled models (Table 4). The reason for presenting two “top models” is that the top performing model includes ND, which is only appropriate for coastal sedimentary basins and can only be computed in a semi-automated fashion. Thus, there is a top-performing “global” model, which does not include ND. The AIC and AUC values both indicate that the regional model is more accurate.

**Table 4.** Summary of the pooled models (combining Kobe and Christchurch data).

	AIC	AUC	Coefficient	Estimate	Std. Error	Wald test
Global Model	74627	0.804	Intercept	24.10	0.4687	51.42
			$\ln(\text{PGA}_{\text{M,SM}})$	2.067	0.0241	85.74
			CTI (30c)	0.355	0.0062	57.24
			$\ln(V_{S30})$	-4.784	0.0829	-57.72
Regional Model	63339	0.892	Intercept	15.83	0.3868	40.92
			$\ln(\text{PGA}_{\text{M,SM}})$	1.443	0.0235	61.47
			CTI (30c)	0.136	0.0068	20.00
			ND	-9.759	0.1042	-93.69
			$\ln(V_{S30})$	-2.764	0.0676	-40.89

Figure 7 shows the predicted probability from the regional model derived from the pooled database for all four earthquake events. Visual inspection of Figure 7 indicates that the pattern of liquefaction is well represented by the model for each event as well as the differences in the extent of liquefaction between the events for these two regions.

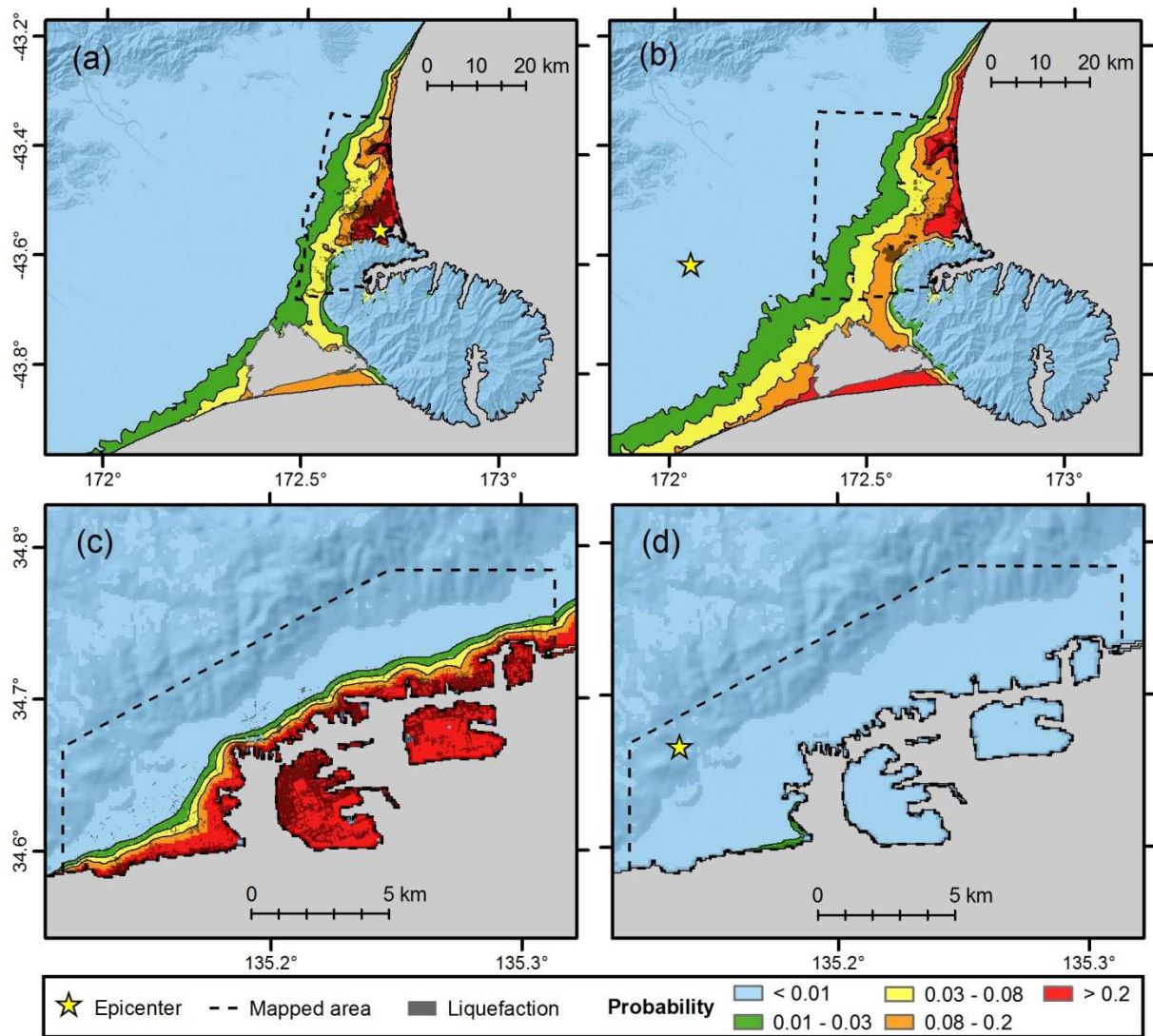


**Figure 7.** Predicted probability of liquefaction using the best model derived from the combined Christchurch and Kobe data (regional model; Table 4) for (a) the Christchurch earthquake, (b) the Darfield earthquake, (c) the 1995 Hyogoken-Nanbu earthquake, and (d) the **M** 4.2 Kobe earthquake.

A more quantitative check on the predicted probabilities is to report the frequency of observed liquefaction features within a range of predicted probabilities. Table 5 presents this information for each event and the results show that there is a strong relationship between the predicted probability and the observed percentage of liquefaction, which is an empirical estimate of spatial extent.

**Table 5.** Percentage of liquefaction occurrence within example probability ranges.

Probability range	Observed percentage of liquefaction			
	Christchurch 2011	Darfield 2010	Kobe 1995	Kobe 2003
> 20%	55.3%	21.9%	39.7%	N/A
8% - 20%	22.1%	11.3%	13.8%	N/A
3% - 8%	9.3%	2.3%	2.3%	N/A
< 3%	1.1%	0%	0.2%	0%

As discussed previously, ROC curves and the AUC are additional quantitative performance measures for a binary response variable. The ROC curves for the two models in Table 4 are plotted in Figure 8. Additionally, the plot shows the points on the curves that correspond to threshold probabilities of 0.1, 0.2, and 0.3. Figure 8 quantifies the improvement that can be gained by using the regional model over the global model in terms of FPR and TPR. Table 6 provides the confusion matrices for threshold probabilities of 0.1 and 0.2, which provides some additional information. Here, the class imbalance in the data is clearly illustrated: most of the predictions and observations are of nonliquefaction. Figure 8 and Table 6 illustrate the effects of adjusting the threshold: as the threshold gets larger, the TPR decreases while the FPR increases. Thus, the threshold should be selected to achieve an appropriate balance of these competing factors.

**Table 6.** Confusion matrices for thresholds of 0.1 and 0.2 for the regional model in Table 4.

Threshold Predicted		$P = 0.1$		$P = 0.2$	
		L	NL	L	NL
Actual	L	6.9	1.4	4.7	3.6
	NL	18.2	73.5	7.7	84.0

## 2.7 Model Visualization

The summary tables, ROC curves, and confusion matrices that we have previously presented to assess the goodness-of-fit of the candidate liquefaction models are relatively abstract and do not necessarily communicate the fit of the model as effectively as a scatterplot of the observed and predicted values can for a continuous

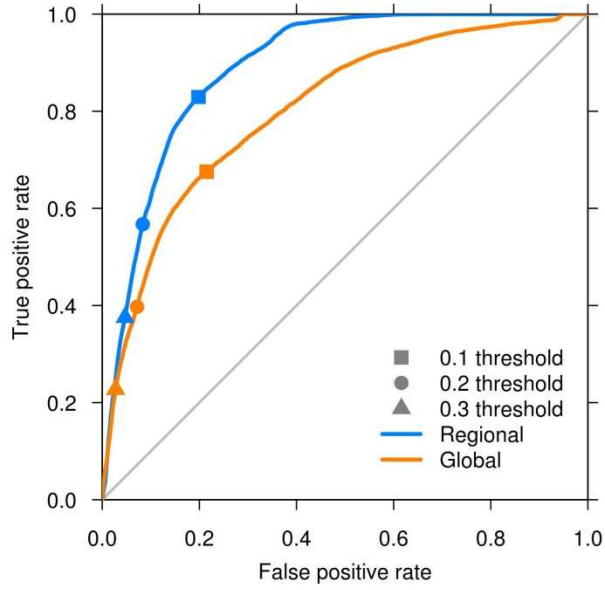


**Figure 8.** Comparison of the ROC curves for the two liquefaction models summarized in Table 4. Points on earth ROC curve for thresholds of 0.1, 0.2, and 0.3 are labeled.

response variable. To create an analogous plot for these data, we construct a 2D image where the axes are two of the explanatory variables and the color is the percentage of the points that liquefied in each pixel (pixels are only shown for pixels with five or more observations). The observations are compared to the predicted probabilities by displaying the model predictions as contour lines on the same image. Figure 9 provides this type of plot for (a) Christchurch, (b) Darfield, (c) Hyogo-ken Nanbu, and (d) the 2003 Kobe earthquakes. The two explanatory variables in these plots are  $PGA_{M,SM}$  and  $ND$ ; the probability contours are from the regional model (Table 4 and Figure 7) assuming a constant values for  $30c\ CTI = 7$  and  $V_{S30} = 200\ m/s$ . The model is multidimensional; therefore, certain variables need to be held constant so that it can be viewed in two-dimensions. From Figure 9, we can see that each earthquake samples a different range of  $ND$  and  $PGA_{M,SM}$  and the model captures the general trends in the data. In the combined database (Figure 10),  $PGA_{M,SM}$  ranges from 0.002 g to 1 g.  $ND$  ranges from 0 to 1;  $CTI$  ranges from 2 to 15. Figure 9 shows how each of the events contribute to constraining the model across the parameter space. For example, the 2003 Kobe event helps to constrain the low  $PGA_{M,SM}$  range of the model and the

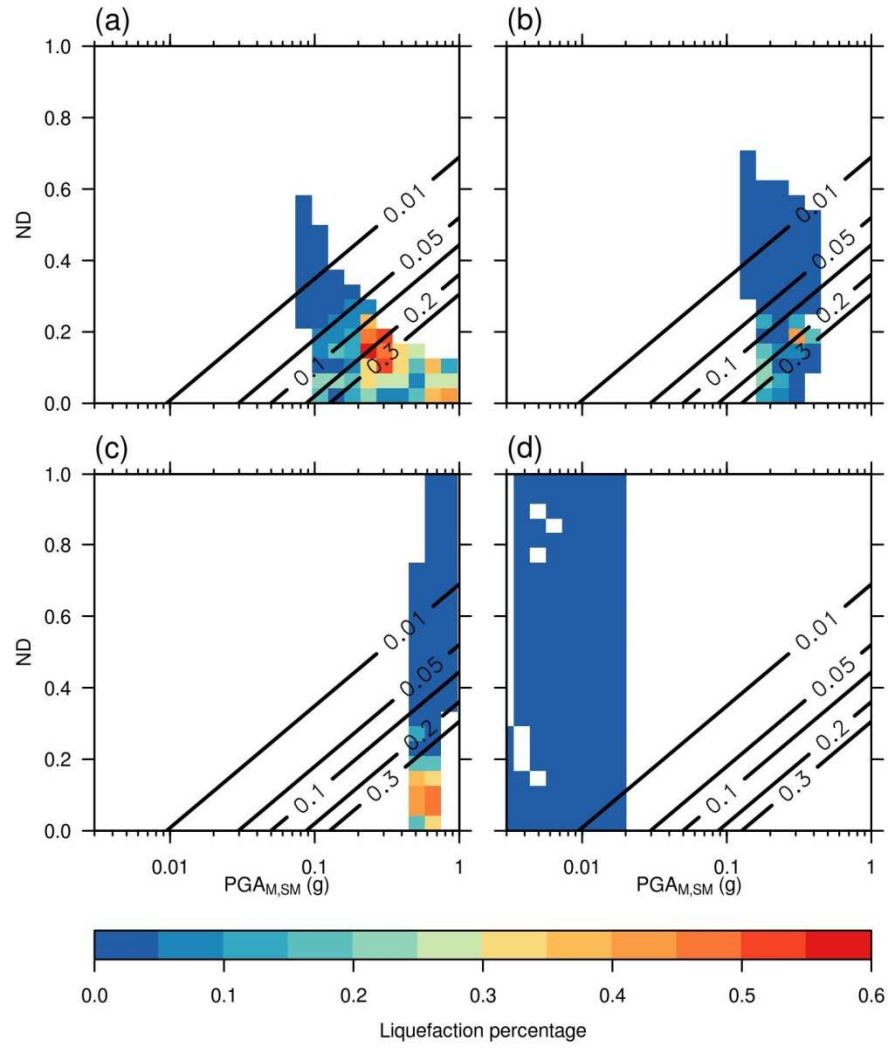


**Figure 9.** The 2D image of the percentage of observed liquefaction with predicted probability contours from the regional model (Table 4) for (a) the Christchurch, (b) the Darfield, (c) the Hyogo-ken Nanbu, and (d) the 2003 Kobe earthquakes. The predicted probabilities assume  $CTI = 7$  and  $V_{S30} = 200$  m/s.



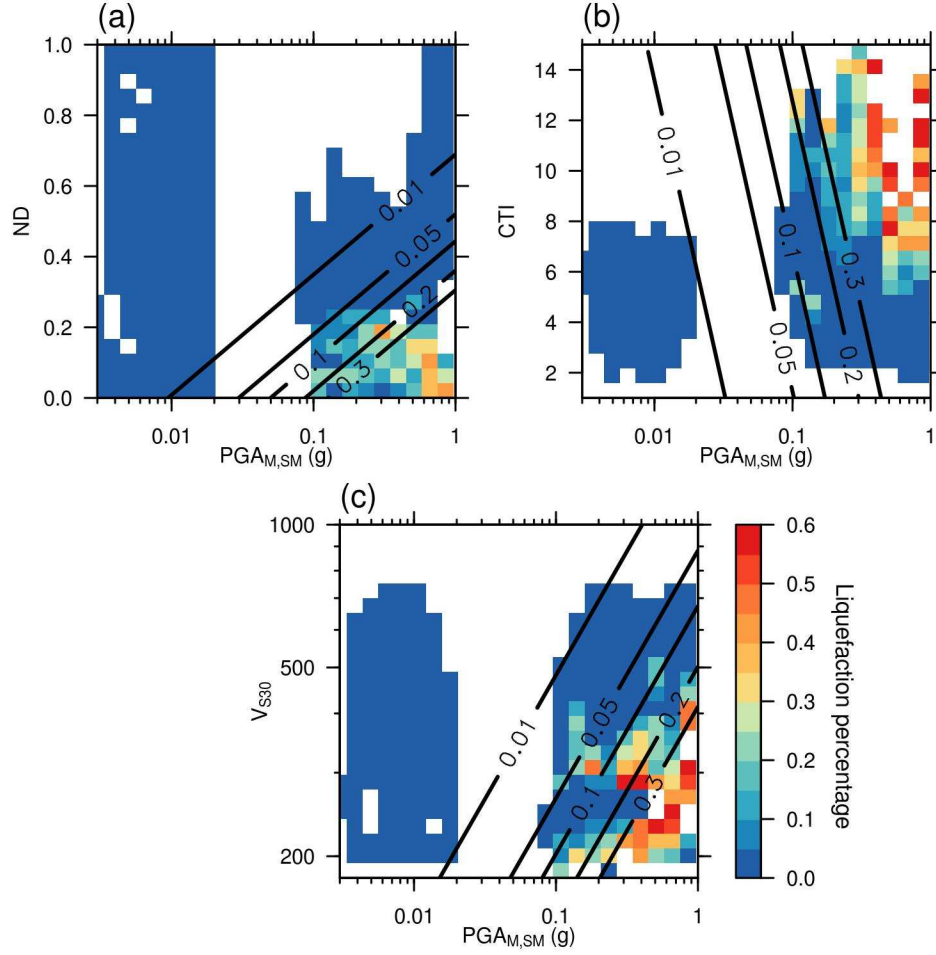


**Figure 10.** The 2D image of the percentage of observed liquefaction in combined database with the predicted probability contours from the regional model (Table 4) when axes are (a) ND and PGA, (b) CTI and PGA, and (c)  $V_{S30}$  and PGA. For covariates not shown in each panel, the assumed values are:  $V_{S30} = 200$  m/s, CTI = 7, and ND = 0.1.

Darfield event helps to constrain the high ND/high PGA range of the model. Together the four events cover the parameter space as shown in Figure 10; Figure 10 shows (a) ND, (b) CTI, and (c)  $V_{S30}$  as a function of  $PGA_{M,SM}$ . The assumed values of the unshown variables are:  $V_{S30} = 200$  m/s, CTI = 7, and ND = 0.1. Figure 10 confirms that the model identifies the observed patterns of where liquefaction occurs relative to the explanatory variables.

The probability of liquefaction is a function of the set of explanatory variables  $X$  in equation (2), which includes the event-specific shaking intensity. However, maps of susceptibility, which are independent of a specific earthquake scenario are also useful.

To create a susceptibility map, we simply compute  $X$  without the intensity ( $PG_{M,SM}$ ) term. The resulting number is not an estimate of the probability of liquefaction, but simply combines the susceptibility terms together with the coefficients that were determined by our regression analysis. Since the absolute values are not meaningful, we present the susceptibility as three classes (low, moderate, and high) in Figure 11 for the Christchurch region.

## 2.8 Port-au-Prince

To test the portability of the regional and global models in Table 4, we compare the predicted probabilities of liquefaction to the mapped liquefaction features in Port-au-Prince. Figure 12a shows the regional model and Figure 12b shows the global model. The models predict high probabilities along the coast, which is also where most of the observed liquefaction was documented. It is important to note the overall, or “macro,” interpretation of the extent of liquefaction for rapid response and loss estimation; the extent of liquefaction in Port-au-Prince is relatively moderate compared to the Christchurch and Hyogo-ken Nanbu earthquakes as predicted by the geospatial liquefaction model. Note that the model predicts large probabilities in some regions where no liquefaction was observed, but it is not clear if this should be interpreted as poor prediction since we do not know with certainty that liquefaction did not occur in these regions. The primary misfit for observed liquefaction that we observe in Figure 12a is along the Riviere Grise (location is labeled in Figure 3) where many liquefaction events were documented but not predicted by the regional model. Along the river, there are a total of 39 liquefaction-related ground failures: 17 are ground cracks, 5 are landslides, 12 are lateral spreads, and 5 are sand blows. This indicates that lateral spreading is the dominant driving mechanism of liquefaction surface effects along the Riviere Grise, while it may not be as dominant in the Christchurch and Kobe events.

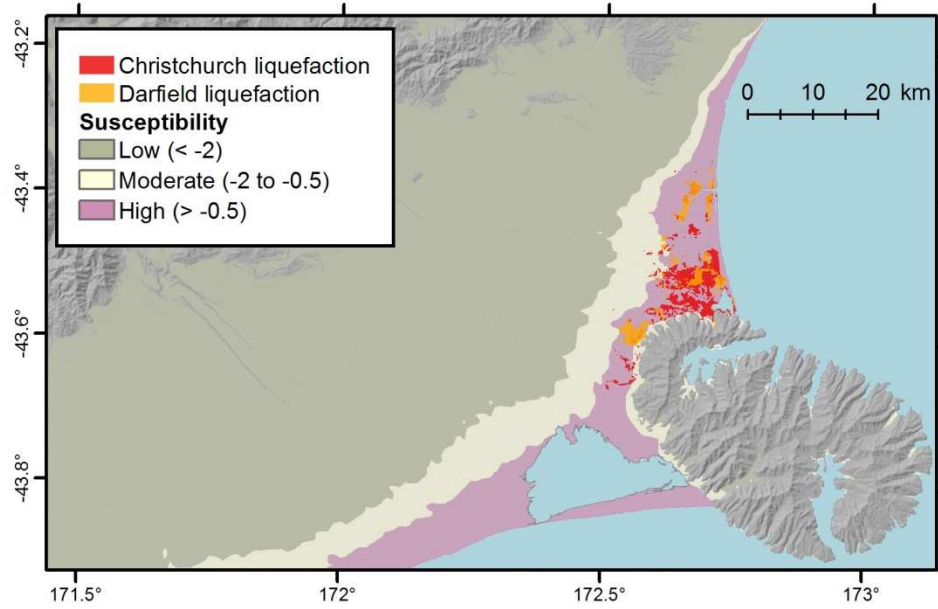


**Figure 11.** Susceptibility map for Christchurch based on the regional model (Table 4). The values in the parentheses are  $X$  in equation (2) without the  $PGA_{M,SM}$  term.

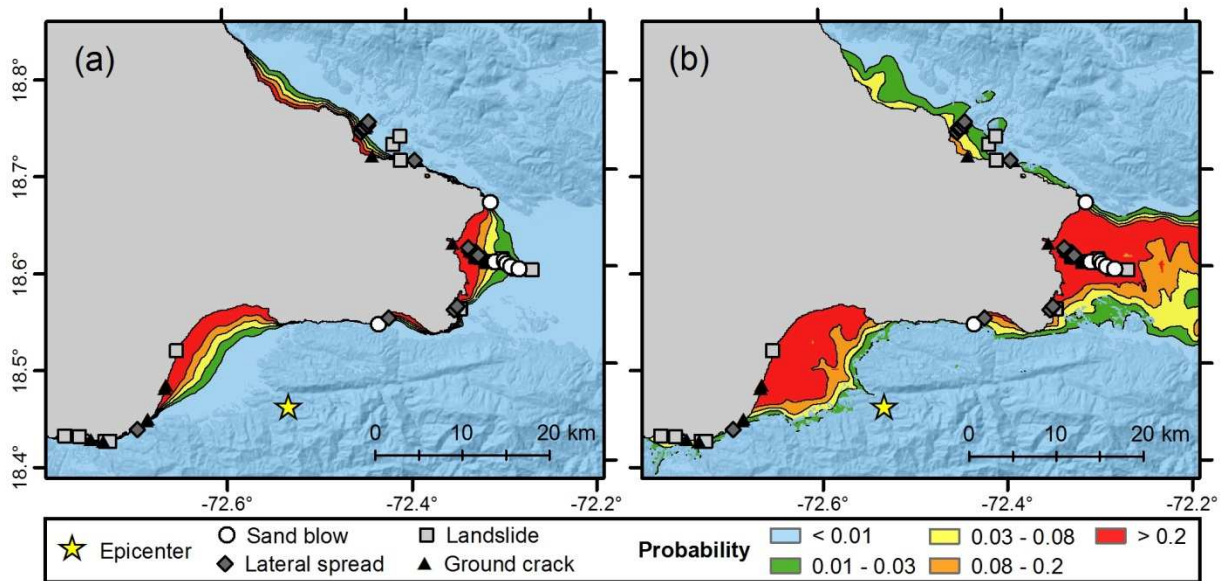


**Figure 12.** Predicted probability of liquefaction from (a) the regional model and (b) the global model applied to the Port-au-Prince region. The models were developed from liquefaction observations in Kobe and Christchurch, and so this comparison checks the portability (or reliability) of the model.

The global model is shown in Figure 12b. As the AUC and AIC values in Table 4 indicate, the global model is less accurate in the Kobe and Christchurch regions. The advantage of a global model, however, is that it does not depend on ND. As seen in Figure 12b, the probabilities predicted by the global model are higher than the regional model along the Riviere Grise where many liquefaction observations were made. The global model, however, also predicts relatively high probabilities of liquefaction in the sediments near the epicenter of the earthquake and in the sediments of the Cul-de-Sac plain where liquefaction was not documented; the geotechnical reconnaissance did not document the presence or absence of liquefaction in these areas so we cannot conclude that these probabilities are incorrect.

## 2.9 Discussion

The preferred models derived from the combined Kobe and Christchurch data (Table 4) represents a substantial departure from existing liquefaction models. The regional model includes ND as an explanatory variable, which is only defined for coastal sedimentary basins; therefore, we also provide a global model that does not include ND, which is thus applicable across a broader range of geologic environments, as demonstrated by the application of these models to Port-au-Prince, Haiti. We recognize, however, that there is still more work that needs to be done to incorporate the effects of major rivers on liquefaction surface effects. The TRP and FPR values reported in Figure 8 for these models should be used as a guideline for the level of accuracy that can be expected when applied to an appropriate geologic environment. Additional regions and events must be added to the liquefaction database before the river proxies can be more accurately constrained.

Fine-tuning of the model will require building a broader database for model development. Once we have a broader database, we can include parameters that help regionalize the model. For example, we understand that CTI,  $d_r$ , and  $d_{wb}$  may be sensitive to regional parameters such as annual precipitation. CTI in a region with low

annual precipitation may have a different meaning from that in a region with high annual precipitation. Future work will assess annual precipitation as a correction factor for CTI in different regions, and adding a seasonality component to the saturation variable. Although there is some literature identifying remotely sensed proxies for soil type, we have not investigated their use in this work. Future work will identify appropriate soil type proxies for the geospatial liquefaction model.

## **2.10 Conclusions**

The liquefaction database compiled for the analysis in this paper includes observations of the presence/absence of liquefaction and geospatial explanatory variables from two earthquakes in Kobe, Japan and two earthquakes in Christchurch, New Zealand. The liquefaction maps are rasterized to ensure that the samples are unbiased with respect to the spatial extent of liquefaction. We develop both region-specific and broadly applicable liquefaction models from this database. The geospatial explanatory variables are identified as proxies for three primary factors that contribute to the likelihood that soils will liquefy: density, saturation, and shaking (as summarized in Table 1). Our best-performing models (Table 4) are based on surface roughness, slope-derived  $V_{S30}$ , CTI, ND, and PGA (from ShakeMap). Both models perform well across all four earthquakes, capturing the general spatial distribution and the extent for the individual earthquakes as well as the major differences in the spatial extent between the different events. These models can be applied for use in rapid response, loss estimation, or scenario simulations to predict the probability of liquefaction. Due to the manner in which the database was developed, the probability predicted by this model can be interpreted as the spatial extent of liquefaction. We provide two alternative models because the most accurate model includes ND as an explanatory variable, which is only applicable in coastal sedimentary basins. Thus, we provide a second, less accurate model that is not restricted to coastal sedimentary basins. When

we check the portability of the models in Port-au-Prince, Haiti, the global model outperforms the regional model because it predicts heightened probabilities of liquefaction along Riviere Gris. We conclude that the improved accuracy that the regional model achieves in terms of AIC and AUC can only be realized in regions that are coastal sedimentary basins where the river network is not the primary contributing factor to the soil density and saturation. As we see in Port-au-Prince, the global model is more appropriate in such cases.

The proposed models are relatively easy to implement for post-earthquake rapid response, loss estimation, and scenario events. All of the explanatory variables in the global and regional models are static, in the sense that they do not vary with time, except for PGA. Thus, these variables only need to be computed once for a given region. Then for a given earthquake, the probability of liquefaction can be computed at any point for which the PGA can be estimated, either from GMPEs, simulations, or ShakeMaps.

## **2.11 Acknowledgements**

This material is based upon work supported by the National Science Foundation under Grant No. 1300781. We would like to thank our colleague at Tufts Rich Vogel who suggested the use of CTI as a measure of saturation. In addition, we thank David Perkins Jonathan Godt, and two anonymous reviewers for providing valuable comments. This work has benefitted from discussions with Harold Magistrale and Yufang Rong.

### 3 An Updated Geospatial Liquefaction Model for Global Application<sup>2</sup>

#### Abstract

We present an updated geospatial approach to estimation of earthquake induced liquefaction from globally available geospatial proxies. Our previous iteration of the geospatial liquefaction model was based on mapped liquefaction surface effects from four earthquakes in Christchurch, New Zealand and Kobe, Japan paired with geospatial explanatory variables including slope-derived VS30, compound topographic index, and magnitude adjusted peak ground acceleration from ShakeMap (Zhu et al., 2015). The updated geospatial liquefaction model presented herein improves the performance and the generality of the model. The updates include 1) expanding the liquefaction database to 27 earthquake events across 6 countries, 2) addressing the sampling of nonliquefaction for incomplete liquefaction inventories, 3) testing interaction effects between explanatory variables, and 4) overall improving model performance. While we test 14 geospatial proxies for soil density and soil saturation, the most promising geospatial parameters are slope-derived VS30, modeled water table depth, distance to coast, distance to river, distance to closest water body, and precipitation. We found that peak ground velocity (PGV) performs better than peak ground acceleration (PGA) as the shaking intensity parameter. We present two models which offer improved performance over Zhu et al. (2015). We evaluate model performance using the area under the curve under the Receiver Operating Characteristic (ROC) curve (AUC) and the Brier score. The best performing model in a coastal setting uses distance to coast but is problematic for regions away from the coast. The second best model, using PGV, VS30, water

---

<sup>2</sup> Zhu, J., L. G. Baise, E. M. Thompson (submitted). An Updated Geospatial Liquefaction Model for Global Application, *Bull. Seism. Soc. Am.*

table depth, distance to closest water body, and precipitation, performs better in noncoastal regions and thus is the model we recommend for global implementation.



### 3.1 Introduction

Soil liquefaction can lead to significant infrastructure damage after an earthquake due to lateral ground movements and vertical settlements. Regional liquefaction hazard maps are important in both planning for earthquake events and guiding relief efforts by positioning resources once the events have occurred. Most liquefaction hazard mapping techniques rely on detailed geologic maps and geotechnical data such as standard penetration test (SPT) or cone penetration test (CPT) results, fines content, and water table depth (Holzer et al. 2006, 2009; Brankman and Baise, 2008), which are not always available in at-risk regions or with sufficient density and coverage.

We have developed a regional liquefaction mapping approach that relies on broadly available geospatial parameters (Baise et al. 2012, Zhu et al. 2013, Zhu et al. 2014, Zhu et al. 2015). The motivation of the work comes from the rapid response and loss estimation communities, where there is a need to predict regional liquefaction extent for any earthquake around the globe. Our work builds on previous work, such as Youd and Perkins (1978), that characterized the relationship between geologic depositional environments and liquefaction susceptibility, and Wald and Allen (2007) that identified a first-order approximation of soil conditions from topography. As a direct precursor to our work, Knudsen and Bolt (2011) found that liquefaction occurrences commonly coincide with simple geospatial features such as topographic slope and distance to the closest river. In our previous work (Zhu et al. 2015), we developed a liquefaction occurrence/nonoccurrence database that was unbiased with respect to the spatial extent (i.e., complete coverage of liquefaction and nonliquefaction occurrence over the mapped area) using data from Christchurch, New Zealand and Kobe, Japan. We tested geospatial parameters as proxies for earthquake loading, soil density, and soil saturation and developed a logistic model

(hereafter termed GLM-Zea15g for geospatial liquefaction model by Zhu et al.; the “g” specifies the global model from that paper) to predict the probability of liquefaction after an event. The model provides a first-order estimate of the spatial coverage of liquefaction from simple geospatial parameters and can be implemented for loss estimation and rapid response. Recent work by Matsuoka et al. (2015) has followed a similar approach for a Japanese liquefaction dataset, but their work relies on the geomorphological classification map of Japan, which is not available globally.

While the results of Zhu et al. (2015) demonstrate the feasibility of the geospatial approach for predicting regional liquefaction extent, further improvements and refinements can be achieved with additional data and analysis. GLM-Zea15g was derived from liquefaction inventories in two regions, both of which were coastal sedimentary basins, with an additional qualitative comparison to the liquefaction that occurred in Port-au-Prince, Haiti. For empirical model development, the quality of a database greatly influences the performance of the model. Increasing the number of samples and sampling a broader range of explanatory variables improves the generality of the model and therefore improves the performance when applying it to make future prediction (Hastie et al., 2001). The results in recent updates to the empirical correlations of liquefaction with in-situ soil indices such as the SPT, CPT, and shear-wave velocity (Cetin et al., 2004; Boulanger and Idriss, 2015; and Kayen et al., 2013) consistently show that an expanded case history database with increased sample size and diversity from different earthquake regions can result in an improved model with reduced overall model uncertainty; for example, a model may perform well when developed and assessed with all large magnitude earthquakes, but it may perform surprisingly poorly if it is then applied to small magnitude earthquakes. Although these geotechnical liquefaction models are most relevant for site specific studies, the lessons learned also apply to our

development of a regional geospatial liquefaction model.

The objective of this paper is to improve the performance of the geospatial liquefaction model, especially for generalization across broad geographic regions. The Zhu et al. (2015) dataset was intentionally limited to spatially complete inventories so that the probabilities from the model could inherently represent the spatial extent of the surface expression of liquefaction. In the updated efforts presented herein, we expand the liquefaction database for testing and improving the model. We have compiled liquefaction data from journal articles and reconnaissance reports, from 23 additional earthquakes from U.S., Japan, China, Taiwan, and India. We have added a combination of datasets with extensive mapped liquefaction as well as specific events from underrepresented geologic regions (inland earthquakes or dry regions) and events with little to no liquefaction. For example, the Northridge and Hector Mine, California, earthquakes provide samples in relatively dry areas that rarely experience liquefaction due to the arid climate. We have included earthquakes where no liquefaction was observed to further explore the parameter space.

In order to expand the database, we include inventories that are not spatially complete. The majority of the added events were documented as incidences of liquefaction (either as points or limited polygons) without information on spatial completeness. This is an artifact of the data collection efforts from these historical events. The majority of the data collected is from field investigations without the more systematic coverage provided with remote sensing techniques. The spatially incomplete nature of the newly added data restricts our ability to preserve the actual class imbalance (i.e., ratio of liquefaction occurrence to non-occurrence), and class imbalance has a strong influence on the probabilities of the model (Oommen et al., 2011; Zhu et al., 2015; Thompson et al., 2016). To address the lack of observations of nonliquefaction in many of the newly added inventories, we use a sampling scheme to sample nonliquefaction data, which is

similar to one that has been successfully applied in landslide hazard mapping by Van Den Eeckhaut et al. (2012) to address the incompleteness of landslide inventories. By addressing class imbalance, we significantly expanded our database which in turn provides the opportunity to constrain a more complex functional form with additional model parameters.

In this paper, we first provide the details of the expanded liquefaction database, including the geospatial parameters that we compile as candidate explanatory variables. We then describe the modeling process and present two alternative models. We evaluate our models in terms of mapped liquefaction extent and Receiver Operating Characteristic (ROC) curves and quantitatively compare the models using statistical goodness of fit measures. Additionally, we compare the model results to prior regional susceptibility studies in San Francisco and Seattle.

## **3.2 Data**

### **3.2.1 Liquefaction Database**

The expanded liquefaction database includes 27 earthquakes from the U.S., Japan, New Zealand, China, Taiwan, and India. Figure 1 shows maps with the locations of the earthquake epicenters. The details of each event included in the database are summarized in Table 1. It is important to note that the liquefaction database consists of inventories from earthquakes that triggered liquefaction as well as earthquakes with insignificant or no liquefaction. Building a well distributed database of liquefaction and nonliquefaction locations across a multi-dimensional parameter space and geographic space is important for developing a useful and general model. We ensure a well-distributed database by sampling a variety of earthquakes in terms of magnitude as well as geologic setting.

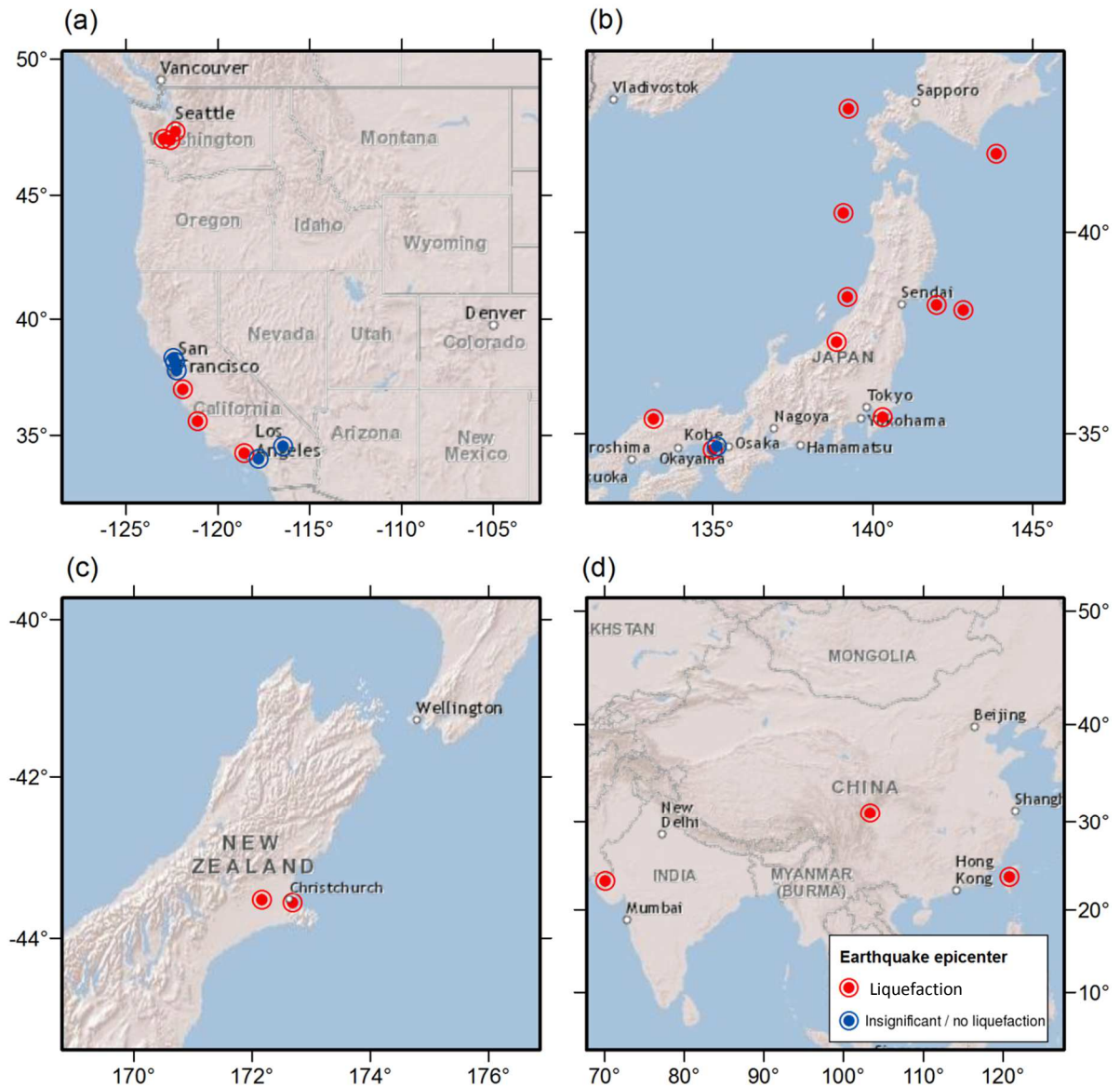


Figure 1. Maps of earthquakes in the liquefaction database from a) United States, b) Japan, c) New Zealand, and d) India, China and Taiwan.

Table 1. Summary of earthquakes in the liquefaction database.

no.	Earthquake	Date	Mw	Liquefaction # of points	Liquefaction Area of polygons (km <sup>2</sup> )	Spatial Category	Liquefaction Occurrence	Coastal or Noncoastal	Reference
1	Christchurch	2011/02/22	6.1	-	71.53	Complete	Yes	Coastal	CGD*
2	Darfield	2010/09/04	7	-	69.18	Complete	Yes	Coastal	CGD*
3	Hyogo-ken Nanbu	1995/01/17	6.9	1883	11.44	Complete	Yes	Coastal	Wakamatsu (2011)
4	Kobe	2003/10/08	4.2	-	-	Complete	No§	Coastal	
5	Loma Prieta	1989/10/17	6.9	123	7.72	Incomplete	Yes	Coastal	Tinsley et al. (1998)
6	Puget Sound	1949/04/13	6.9	153	-	Incomplete	Yes	Coastal	Chleborad et al. (1998)
7	Puget Sound	1965/04/29	6.7	229	-	Incomplete	Yes	Coastal	Chleborad et al. (1998)
8	Nisqually	2001/02/28	6.8	69	-	Incomplete	Yes	Coastal	Bray et al. (2001)
9	Northridge	1994/01/17	6.6	36	-	Incomplete	Yes	Noncoastal	Stewart et al. (1994), Stewart et al. (1996), Moehle et al. (1994)
10	San Simeon	2003/12/22	6.6	10	0.02	Incomplete	Yes	Coastal	Holzer et al. (2005)
11	Hokkaido Nansei-oki	1993/07/12	7.7	376	4.19	Incomplete	Yes	Coastal	Wakamatsu (2011)
12	Chiba-ken Toho-oki	1987/12/17	6.5	67	7.39	Incomplete	Yes	Coastal	Wakamatsu (2011)
13	Miyagi-ken-oki	1978/06/12	7.6	50	0.29	Incomplete	Yes	Coastal	Wakamatsu (2011)
14	Niigata	1964/06/16	7.6	124	71.64	Incomplete	Yes	Coastal	Wakamatsu (2011)
15	Nihonkai Chubu	1983/05/26	7.7	12	54.44	Incomplete	Yes	Coastal	Wakamatsu (2011)
16	Niigata-ken Chuetsu	2004/10/23	6.6	313	14.7	Incomplete	Yes	Coastal	Wakamatsu (2011)
17	Tottori-ken Seibu	2000/10/6	6.7	120	2.61	Incomplete	Yes	Coastal	Wakamatsu (2011)
18	Tokaichi-oki	2003/09/26	8.3	139	0.02	Incomplete	Yes	Coastal	Wakamatsu (2011)
19	Tohoku	2011/03/11	9.1	-	107.07	Locally Complete	Yes	Coastal	MLITT (2011)
20	Chi-Chi	1999/09/21	7.6	170	2.52	Incomplete	Yes	Noncoastal	Chu et al. (2004)
21	Bhuj†	2001/01/26	7.6	-	377.4	Complete	Yes	Noncoastal	Singh et al. (2002)
22	Yountville	2000/09/03	5.0	-	-	Complete	No§	Coastal	
23	Piedmont	2015/08/17	4.0	-	-	Complete	No§	Coastal	
24	Napa	2014/08/24	6.0	2	-	Complete	No§	Coastal	GEER (2014)
25	Chino Hills	2008/7/29	5.4	-	-	Complete	No§	Coastal	GEER (2008)
26	Hector Mine	1999/10/16	7.1	-	-	Complete	No§	Noncoastal	
27	Wenchuan	2008/05/12	7.9	116	-	Incomplete	Yes	Noncoastal	Cao et al. (2010)

\* Canterbury Geotechnical Database (see Data and Resources)

† Not included in the model development.

§ Insignificant to no liquefaction.

As evident from Figure 1, the majority of the events are located in coastal areas. We define a coastal event as one where the liquefaction occurrences are on average within 20 km of the coast, or for earthquakes with insignificant or no liquefaction, epicentral distances less than 50 km. Based on these criteria, there are five noncoastal events with observed liquefaction in this database: the 1994 Mw6.6 Northridge (#9), 2001 Mw7.7 Bhuj (#21), 1999 Mw7.6 Chi-Chi (#20), 1999 Mw7.1 Hector Mine earthquake (#26 – an earthquake with insignificant or no liquefaction), and 2008 Mw7.9 Wenchuan (#27) events. The data from the Bhuj earthquake were only used for verification, but not included in the model development, because they were from a remote sensing study (Singh et al., 2002) that lacks validation. Although the Northridge earthquake led to shaking in the coastal environment, the mean distance to coast for the liquefaction observations was 25 km. A sixth noncoastal event, the 2015 Mw7.8 Nepal earthquake is used for verification but not included in the database. The low number of noncoastal events is not entirely surprising because the majority of tectonically active regions are coastal, and liquefaction is known to occur in coastal sediments (e.g. artificial fill, beach deposits, alluvial and marine sands) as documented by Youd and Perkins (1978) and numerous well-studied earthquakes such as 1989 Loma Prieta (Tinsley et al., 1998), 1995 Hyogo-ken Nanbu (Hamada et al., 1995), and 2011 Tohoku (MLITT, 2011). Because the database is biased toward coastal events, we will investigate the portability of our results outside of the coastal setting in the Results (Models subsection).

For the purpose of this paper, events can be classified as complete or incomplete datasets. This is an important distinction in terms of how the datasets are sampled for liquefaction and nonliquefaction points. A complete dataset includes events like the 1995 Kobe (#3) and the 2010-2011 Darfield and Christchurch (#1, 2) earthquakes that are extensively mapped as polygons of liquefaction occurrence. In a complete dataset, nonliquefaction points can be sampled anywhere within the mapped extent that is not

covered by a liquefaction polygon. For our purposes, complete datasets also include well studied events where liquefaction is insignificant or absent. Examples of this case are the 2003 M4.2 Kobe event (#4) and the 2014 M6.0 Napa (#24) event. These earthquakes with insignificant or no liquefaction provide complete datasets that are very important for providing coverage of the parameter space. The first four earthquakes (#1-4) in the database were used for developing the prior model (Zhu et al., 2015). Except for the 2010-2011 Darfield and Christchurch (#1, 2) and some Japanese events (#3, #11-18) where we have access to data in digital format (see Data and Resources; Wakamatsu, 2011), we obtained the rest of the data in Table 1 by digitizing published liquefaction maps (see Table 1 for references).

To illustrate the benefit of adding the earthquakes with insignificant or no liquefaction to the database, we illustrate the data space represented by plotting the proportion of liquefaction occurrences as a function of peak ground velocity (PGV) and the slope-derived time-averaged shear-wave velocity to 30 m depth ( $V_{S30}$ ) in Figure 2. To construct this figure, we sampled the liquefaction inventories using the same sampling method described in the Sampling section. In this figure, white cells indicate no data points in the interval. As shown in Figure 2a, when the database only contains earthquakes with extensive liquefaction, there are almost no data where PGV is less than 3 cm/s. The lack of data at low PGV may result in false model predictions for small events (low PGV) where liquefaction is not expected to occur. After adding the earthquakes with insignificant or no liquefaction, the data space for low PGV values is sufficiently filled, and the boundary between liquefaction and nonliquefaction becomes better differentiated.

As discussed above, the liquefaction data can be divided into two groups based on the spatial completeness and this categorization impacts how liquefaction and nonliquefaction points are sampled. The group that is spatially complete consists of the four events used for developing the prior model (# 1-4) and the insignificant-to-no



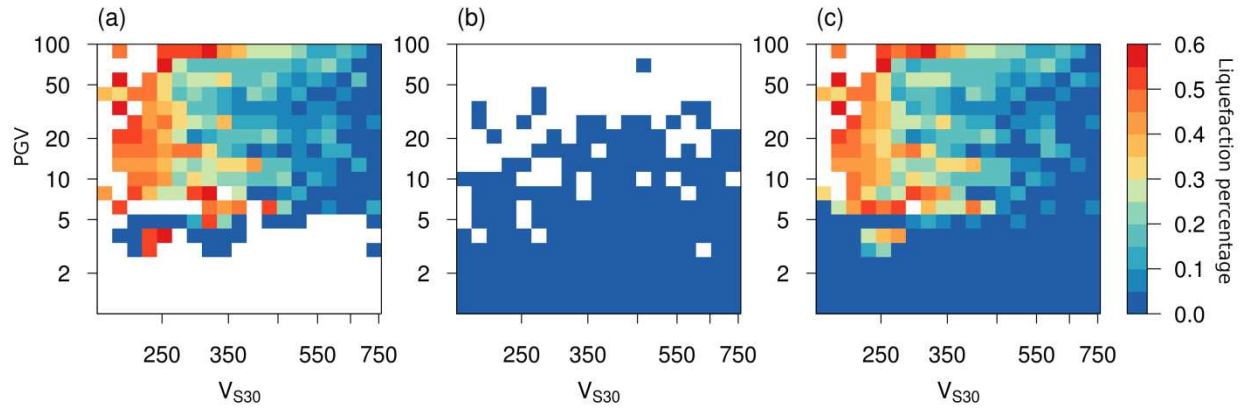


Figure 2. Percentage of liquefaction versus nonliquefaction as a function of PGV and  $V_{S30}$  for a) liquefaction events, b) events with insignificant or no liquefaction, and c) all events in the database.

liquefaction complete events (#22-26). The 2011 Tohoku earthquake (#19) was spatially complete in a limited region (MLITT, 2011) but not for the entire affected area, so we treated it as an incomplete dataset. For this group, liquefaction observations are represented by polygons and the mapped extent associated with the liquefaction data is documented. Because the regions were well studied as evidenced by the reconnaissance reports and the post-event literature, we can assume that the liquefaction was completely mapped, and therefore, nonliquefaction can be assumed outside the liquefaction polygons and within the mapped extent. This type of data is only available for a few events, generally where remote sensing has been incorporated into the post-earthquake data collection or in well studied regions like the San Francisco Bay area in the U.S. or large urban regions in Japan where the field reconnaissance was extensive.

Unfortunately, the majority of events in Table 1 (# 5-21) are spatially incomplete and result from limited field investigations described in the literature. In general, the available data are mapped liquefaction occurrences, predominately represented by points (limited polygons may exist for some local areas) with limited information

about the extent of mapping. As a result, additional assumptions are required in order to obtain liquefaction nonoccurrence data, as discussed in the Methods (see the Sampling subsection).

### 3.2.2 Geospatial Predictors

In parallel to the liquefaction/nonliquefaction occurrence data, we assemble a database of explanatory variables for use in building the liquefaction models. We consider explanatory variables that can approximate some of the governing factors for whether liquefaction will or will not occur: soil density, soil saturation, and earthquake loading. We only consider variables that can be easily derived at a global scale, and so some factors that affect the occurrence of liquefaction (e.g., soil plasticity) are not considered in our approach. Table 2 summarizes the explanatory variables we have tested for the geospatial liquefaction model, which is expanded from those tested in Zhu et al. (2015). The spatial resolution for all variables is 30 arc-sec.

Table 2 Summary of all candidate explanatory variables.

Variable description	Variable name	Density	Saturation	Load
Shear wave velocity over the first 30 m (slope derived)	$V_{S30}$	•		
Elevation	$elev$	•		
Topographic Slope	$slope$	•		
Roughness	$rough$	•		
Topographic position index	TPI	•		
Terrain roughness index	TRI	•		
Distance to the nearest coast	$dc$	•	•	
Compound topographic index	CTI		•	
Global water table depth	$wtd$		•	
Distance to the nearest river	$dr$		•	
Distance to the nearest water body	$dw$		•	
Elevation above the nearest water body	$hwater$		•	
Mean annual precipitation	$precip$		•	
Aridity index	AI		•	
PGA	PGA			•
PGV	PGV			•
Magnitude	Mw			•
Magnitude scaling factor	MSF			•

Soil density is an important liquefaction susceptibility factor; loose soils are more susceptible than dense soils. Wald and Allen (2007) have demonstrated that soil density is correlated with topographic gradient using California, Taiwan, Utah, and the Mississippi Embayment as test cases. Although recent work has demonstrated that the Wald and Allen (2007) correlations are less effective in some regions (e.g., Magistrale et al., 2012), the method is still appropriate for broad applicability and is used globally with the USGS ShakeMap to estimate soil amplification after earthquakes (Worden et al., 2010). We use the digital elevation model (DEM) from the Global multi-resolution terrain elevation data 2010 (GMTED2010; See Data and Resources). Several geospatial variables were computed directly from the elevation data, such as slope and  $V_{S30}$ . Slope is calculated using the *gdgradient* command in Generic Mapping Tools software (see Data and Resources).  $V_{S30}$  is estimated from slope using the method described in Wald and Allen (2007). We use the coefficients for active tectonic regions because all the earthquakes in the database are in active tectonic regions.

Because surface texture is often used in landform classifications, we consider three roughness indices (roughness, topographic position index [TPI], and terrain roughness index [TRI]). Roughness is defined as the largest inter-cell difference of a central pixel and its eight surrounding cell. TPI is defined as the difference between a central pixel and the mean of its eight surrounding cells. TRI is defined as the mean difference between a central pixel and its eight surrounding cells. They are computed from the DEM using the *gdaldem* command in the Geospatial Data Abstraction Library (GDAL; see Data and Resources) based on the definitions described in Wilson et al. (2007). As with the gradient, these roughness measurements are dependent on the resolution of the digital elevation model that they are derived from.

Soil saturation is an important parameter in liquefaction analyses as the soil has to be saturated or partially saturated in order to liquefy. As water flows downhill and accumulates in streams, rivers, lakes, and oceans, soil saturation is generally correlated with proximity to water bodies and regional climate conditions. We used saturation proxies that are derived from topography, climate data, and groundwater models. We compute distance to river ( $dr$ ) using the rivers from the HydroSHEDS database (see Data and Resources), which were derived from topography. We compute the distance to the nearest coast ( $dc$ ) from a global dataset computed by NASA's Ocean Color Group (see Data and Resources). The distance to the nearest water body ( $dw$ ) is calculated as the minimum value of  $dr$  and  $dc$ . We derive elevation above the nearest water body ( $hwater$ ) from the river layer and elevation data. We use the compound topographic index (CTI; Beven and Kirkby, 1979) from the HydroSHEDS database (see Data and Resources). CTI, also referred to as the Wetness Index, is a function of the flow accumulation and the topographic slope.

In addition to the saturation proxies derived from topography, we also include globally available climate information as an input to our estimation in order to differentiate the soil saturation across different climate regions such as the relative dry region affected by the 1999 M 7.1 Hector Mine earthquake (no liquefaction) versus the wet region affected by the 2001 M6.8 Nisqually earthquake (extensive liquefaction). The mean annual precipitation for the former region is approximately 200 mm, whereas the mean annual precipitation for the later region is approximately 1200 mm. We consider mean annual precipitation ( $precip$ ) from the WordClim database (see Data and Resources) and aridity index (AI) from the CGIAR-CSI Global Aridity dataset (see Data and Resources). The global precipitation dataset was developed by interpolating from over 40,000 weather stations across the world and averaging over the 1959-2000 time periods. To incorporate the recent efforts of large scale groundwater modeling, we use a global dataset of water table depth ( $wtd$ ) from Fan et

al. (2013), who modeled groundwater flow using a model constrained by climate, terrain and sea level and calibrated it with over 1.5 million published records of water table depths.

Finally, earthquake magnitude and intensity parameters are important in liquefaction analyses because ground shaking of a contractive soil can lead to pore water pressure increase which is a necessary component of liquefaction. The effects of earthquake loading are modeled by ground shaking parameters and proxies for earthquake duration. For ground shaking parameters, we consider peak ground acceleration (PGA) and peak ground velocity (PGV) from ShakeMap (see Data and Resources), which provides near real-time estimates of ground shaking that incorporates macroseismic data as well as available ground motion records with ground motion prediction equation (GMPE) estimates (Worden et al., 2010). To approximate earthquake duration, we consider the magnitude scaling factor (MSF) in Youd et al. (2001).

To demonstrate the typical patterns that these geospatial explanatory variables exhibit, maps for eight potential explanatory variables for the San Francisco Bay area and two shaking variables for the 1989 Loma Prieta earthquake are shown in Figure 3. Parameters such as  $V_{S30}$ ,  $wtd$ , CTI, and  $hwater$  are correlated with topography and show similar patterns. Also, parameters like  $dr$  and  $dc$  vary slowly and provide soil saturation proxy at a lower resolution as compared to parameters such as CTI or  $wtd$  which vary much more locally.

### 3.3 Methods

#### 3.3.1 Sampling

To create the liquefaction database with liquefaction occurrence and nonoccurrence, as well as all relevant geospatial explanatory variables, sampling grids are populated at 100 m spacing for each earthquake region in a local Cartesian coordinate system. A

grid pixel is labeled as liquefaction when there is a liquefaction point inside the pixel or 30% of the grid pixel is covered by a liquefaction polygon. The 30% threshold is selected to rasterize polygons because we found that for the spatially complete data the 30% threshold retains the same liquefaction to nonliquefaction ratio before and after the rasterization (Zhu et al., 2015). Because the

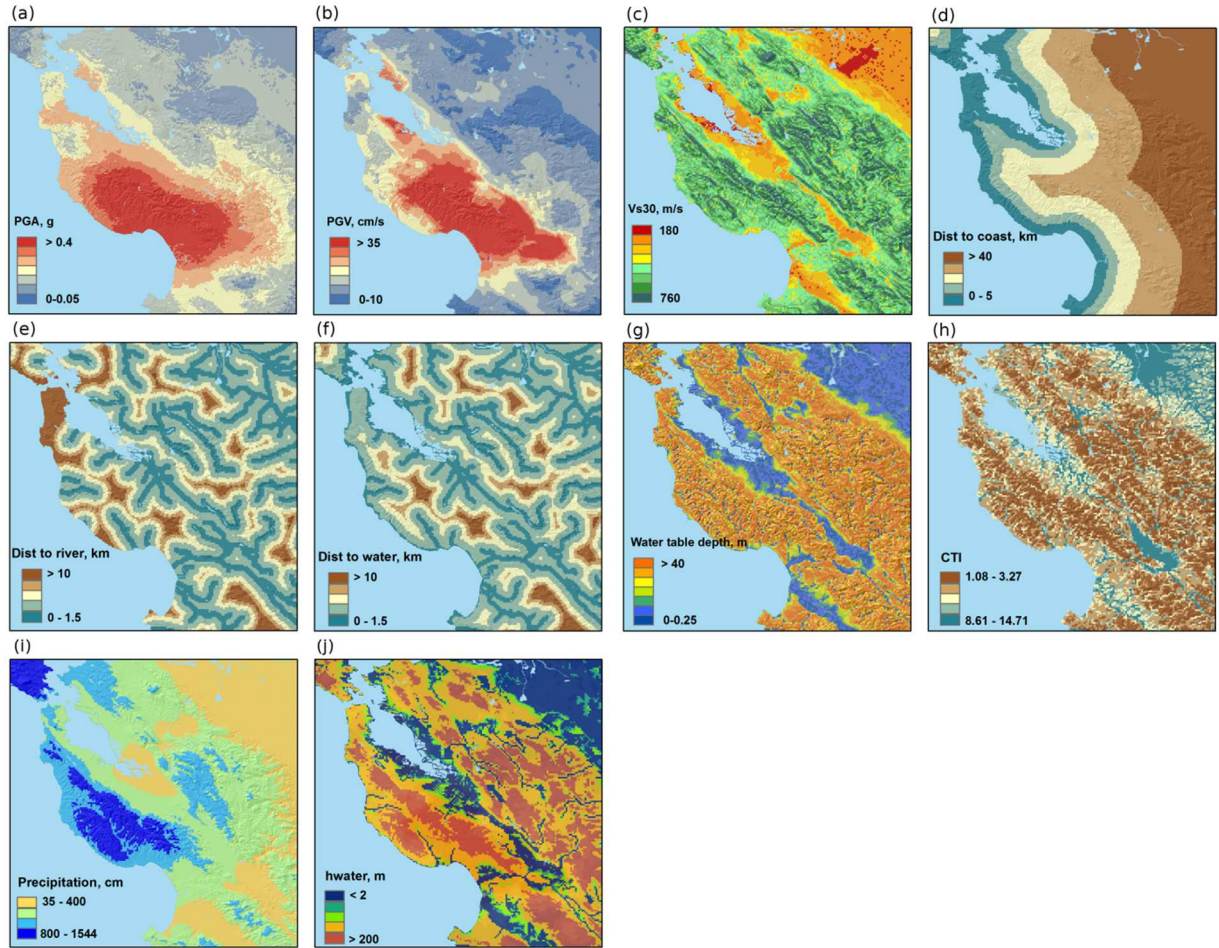


Figure 3. Maps of candidate explanatory variables: a) PGA, b) PGV, c)  $V_{S30}$ , d)  $dc$ , e)  $dr$ , f)  $dw$ , g)  $wtd$ , h) CTI, i)  $precip$ , and j)  $hwater$  for the San Francisco Bay area. PGA and PGV are shown for the 1989 Loma Prieta earthquake all other variables are event independent.

absence of liquefaction is generally not documented in earthquake inventories, we developed a strategy to sample “nonliquefaction” data. For a complete dataset where the liquefaction data are documented within a mapping extent, we randomly sample nonliquefaction from the pixels not covered by a liquefaction polygon. For an incomplete dataset where the mapping extent is unknown, we apply circular buffers around known liquefaction locations to sample nonliquefaction (illustrated in Figure 4). This allows for holes in the sampled regions, which will be determined by the distribution of the liquefaction locations and the buffer size. We use a nonsampling buffer immediately around each liquefaction point because we do not know the spatial extent of the recorded liquefaction feature. The sampling region is defined as the area outside of the nonsampling buffer and within the sampling region. After testing a range of buffer widths (see the Sensitivity analyses of sampling choices subsection in Discussion), we sample nonliquefaction pixels within an area that is 1 km to 15 km from an observed liquefaction pixel. Figure 4 is a schematic illustration of the spatial

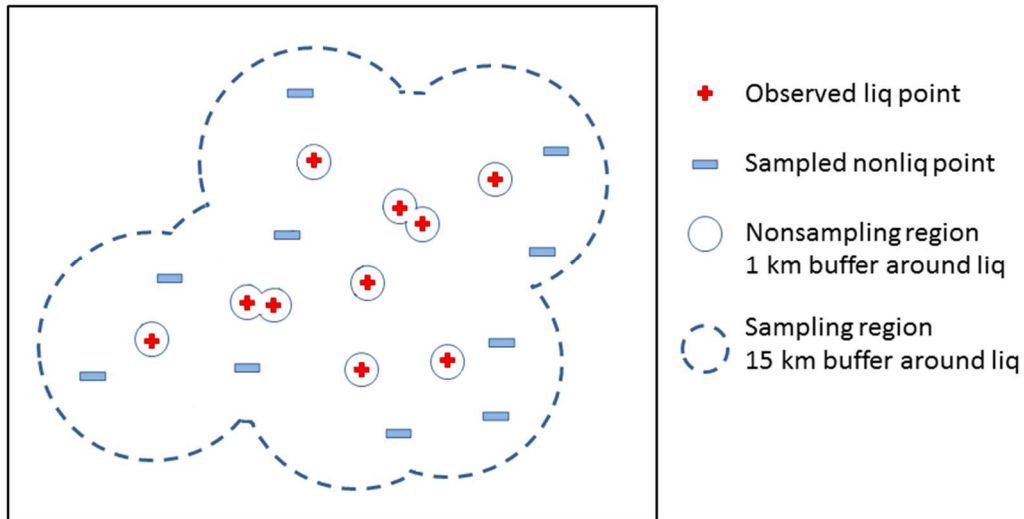


Figure 4. Sampling nonliquefaction events using spatial buffers.

buffer, with a solid circle showing the boundary of the inner buffer and the dashed line showing the boundary of the outer buffer. For events with insignificant or no liquefaction, the sampling region is determined by the area where the ShakeMap intensities are available.

### 3.3.2 Logistic Model

We use logistic regression to model the probability of liquefaction. Logistic regression is a statistical approach that can be used to describe the relationship of several independent variables to a binary dependent variable. The use of the logistic equation ensures that the resulted probability lies in the range between zero and one:

$$P(X) = \frac{1}{1+e^{-X}}, \quad (1)$$

where  $X = \beta_0 + \beta_1 x_1 + \dots + \beta_k x_k$ ,  $x_1, x_2, \dots, x_k$  are the explanatory variables, and  $\beta_0, \beta_1, \dots, \beta_k$  are the coefficients estimated from the regression. We use the maximum likelihood method to obtain these estimates (Kleinbaum and Klein, 2010).

### 3.3.3 Sampling Strategy

Because the events in the database were mapped with different levels of detail (polygons vs. points), the number of data points for an event in the database does not necessarily correlate with the extent of liquefaction occurred. An event that includes mapped polygons results in considerably more data points than an event that only includes liquefaction points. For example, the 2011 Christchurch earthquake has 8867 data points, while the 1989 Loma Prieta event has 789 liquefaction points. To prevent a specific event from dominating the regression results, we randomly sample 1000 liquefaction points from each event for model development. For an event where the



number of liquefaction points is less than 1000, we use all the liquefaction points available for that event. To improve model stability and avoid overfitting, we resample 50 times for each model and average the model coefficients. Investigation of the variability of model performance and coefficients across different random samples constrains the sensitivity to the sampling scheme.

In Zhu et al. (2015), we chose to use an imbalanced dataset (approximately 1:13 liquefaction:nonliquefaction) because we aimed to develop a probability estimator that predicts the areal extent of liquefaction. In other words, we wanted the resulting probability to correlate with spatial extent (e.g., areas labeled 10% probability of liquefaction will contain about 10% liquefaction by area). This is only possible for complete inventories. As discussed in the Introduction, class imbalance significantly influences the resulting probabilities from logistic regression models. However, in the current approach, we include incomplete datasets in order to improve the generality of the model. As a result, the class imbalance in the current database no longer represents the actual class imbalance. As an alternative approach, we can optimize the model as a model classifier (i.e., discriminating between occurrences and nonoccurrences). Many studies have shown that for several classifiers, a balanced dataset provides improved overall classification performance compared to an imbalanced data set (Weiss and Provost, 2001; Laurikkala, 2001; Estabrooks et al., 2004). To minimize the effect of class imbalance and optimize the database for the development of a classifier, we sample equal numbers of liquefaction and nonliquefaction points (e.g., 1000 points each). For events with insignificant or no liquefaction, we sample 1000 nonliquefaction points. Sampling so that the full database has a 1:1 class balance is another reasonable approach, but it is not the choice we made. For events with insignificant or no liquefaction, the sampling region is the region where the ShakeMap intensities are available. In the Discussion (Interpretation of Probabilities) section, we

evaluate the interpretation of the probabilities in terms of expected spatial extent of liquefaction to understand the impact of using a balanced sample.

### **3.3.4 Modeling Strategy**

Our goal is to develop a model that not only fits the available data well, but will fit new data that was not used to develop the model. Thus, we select a simple model that reflects as much of the underlying physics of the problem as possible. Our modeling strategy involves four stages: (1) exploratory data analysis, (2) interaction assessment, (3) base model selection (i.e., an initial model that does not account for saturation), and (4) a stepwise assessment of alternative saturation parameterizations. Exploratory data analysis is carried out first because we think it is important to understand the distributions and relationships between the liquefaction/nonliquefaction data and explanatory variables. We plot the histograms of the liquefaction and nonliquefaction points (for a single set of sampled observations) as well as the estimated probability of liquefaction over the range of each candidate variable. We use this to identify gaps in the data space as well as variables that are strongly predictive.

Next, we assess interaction effects of individual pairs of candidate variables. This is addressed prior to the final model selection because if there is evidence of interaction involving certain variables, then the interaction term (e.g., the product of two interacting variables) has to be considered in the model selection stage. We then establish a base model by selecting variables that show strong correlations with the probability of liquefaction. We prefer using a base model to guide the model selection rather than completely relying on the performance measures. Finally, we test the base model with additional candidate variables to determine if their combinations can improve the model performance.

In the model selection stage, we evaluate candidate functional forms on a dataset sampled from the entire database using the described sampling method. There are

various ways to measure the performance of a statistical prediction model. We use the Brier score (Brier, 1950) to quantify how close predictions are to the actual outcome and AUC to quantify discrimination (do liquefied locations have higher predicted probabilities than those that did not?). The Brier score measures the mean squared difference between predicted probabilities and actual outcomes. The Brier score for a model can range from 0 for a perfect model to 0.25 for a non-informative model. Useful performance metrics for binary classifications include the true positives rate (TPR), which measures the fraction of positive cases that are correctly classified, and false positive rate (FPR), which measures the fraction of negative cases that are misclassified as positive. The ROC curve has proved a useful tool for evaluating empirical liquefaction models (Oommen et al., 2010; Maurer et al., 2015). A ROC curve is a plot of the TPR against FPR at various probability thresholds. For a given threshold, a model that perfectly predicts the binary response would have  $TPR = 1$  and  $FPR = 0$ . The closer the ROC curve comes to this ideal case (i.e., the top-left edge of the plot), the better the model performance. Thus, AUC is a scalar measure that quantifies the accuracy of the probabilistic classifier, because as the AUC increases the ROC curve approaches the top-left edge of the plot. The AUC limits are from 0.5 (random classification) to 1.0 (perfect accuracy).

## **3.4 Results**

### **3.4.1 Data Exploration**

We create a regression dataset from the entire database using the described sampling method. In order to explore the data and understand the correlation between individual explanatory variables and the liquefaction and nonliquefaction data, we present histograms of liquefaction (red) and nonliquefaction (green) data over the range of each candidate variable (including transformations) in Figure 5. On the same plots, the

ratio of liquefaction points within each bin is shown as a gray dot where the darkness of the gray dot increases with the number of data points within the bin (the scale is different for each panel). In other words, the darkness of the point is an indication of weight. The blue curve represents a univariate logistic model fit to the data.

In the plots, shaking parameters such as PGA and PGV are transformed by taking their natural logarithm, because their distributions are well represented by a lognormal distribution. Similarly, we use the natural logarithm of  $V_{S30}$ . We notice the distributions of a few variables are sharply skewed, such as  $dc$ ,  $wtd$ ,  $elev$ , TRI and *roughness*, with a greater density of data having values close to zero. As a result of the skew, the occurrence of liquefaction is more sensitive to changes in small values than large values. Therefore, we prefer to apply a square root transformation to increase the weights of small values. In the model selection, we consider the variables both with and without transformation.

In Figure 5,  $\ln(\text{PGA})$ ,  $\ln(\text{PGV})$ ,  $\ln(V_{S30})$ ,  $dw$ , and precipitation show strong correlations with the probability of liquefaction. We observe that  $\ln(\text{PGV})$  is more evenly distributed than  $\ln(\text{PGA})$  and  $\ln(\text{PGV})$  shows a stronger correlation with the estimated probability of liquefaction from data. The estimated probability of liquefaction seems negatively correlated with  $\ln(\text{PGA})$  and  $\ln(\text{PGV})$  when PGA is beyond 0.3 g and PGV is beyond 50 cm/s. Magnitude, or a function of magnitude, sometimes is considered as a factor to scale PGA (e.g., Youd et al., 2001). However, with our sampling scheme the relationship between the probability of liquefaction and magnitude cannot be reliably estimated because the number of points that are sampled for an event is independent from the magnitude (i.e., 1000 liquefaction points if available and 1000 nonliquefaction points). The relationship between the estimated probability of liquefaction and magnitude that appears in Figure 5 appears to be an artifact of our sampling, and cannot be reliably used for prediction. This also appears to be the case for MSF, which is a function of magnitude.

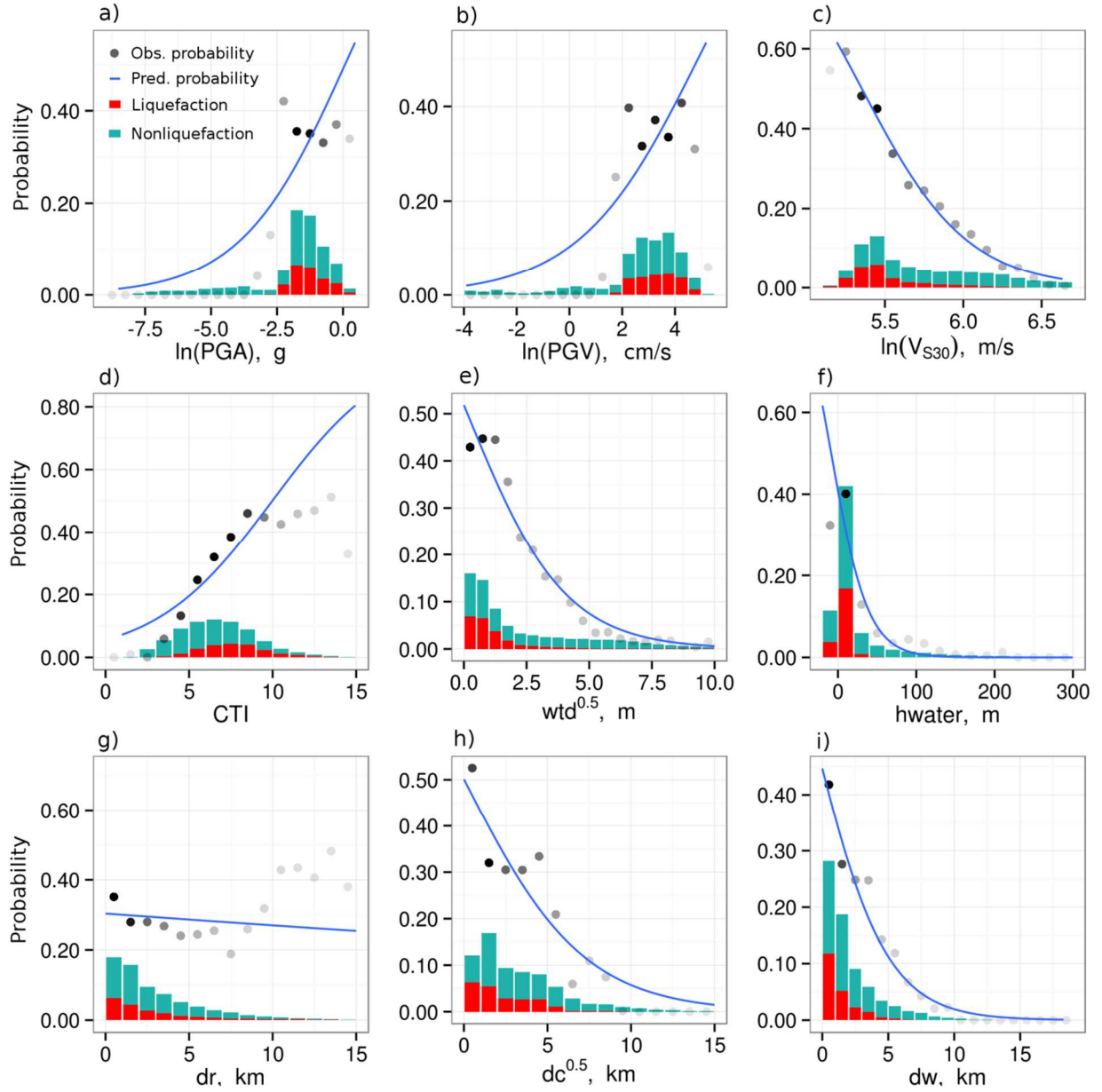
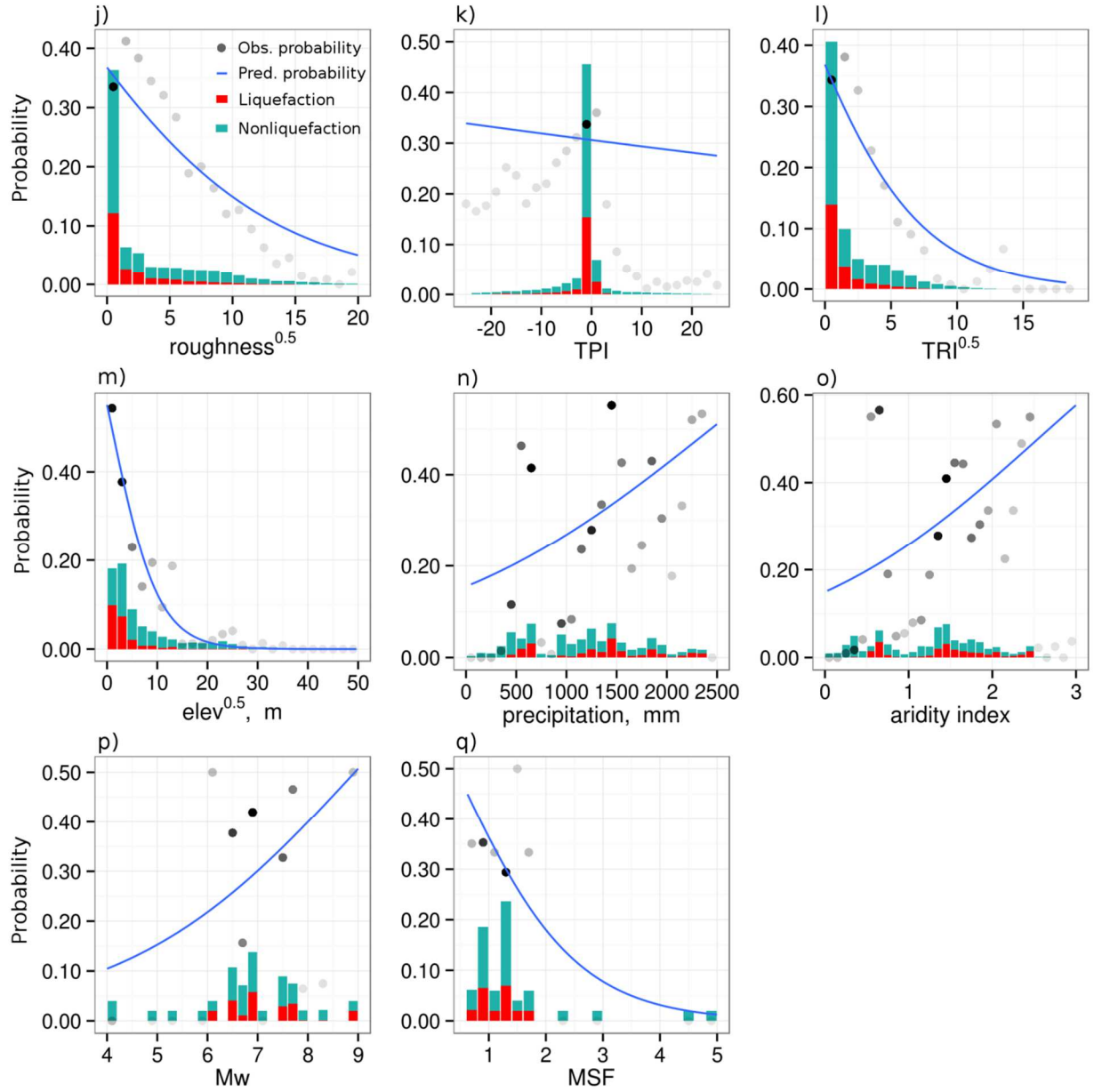


Figure 5. Histograms of liquefaction (red bars) and nonliquefaction (green bars) and the probability of liquefaction observed from the data (gray circles) at intervals of a variable's value and the probability (blue line) predicted from a univariate model. The darkness of the gray dot increases with of the number of data points within the bin (the scale is different for each panel). In other words, the darkness of the point is an indication of weight.



### 3.4.2 Interaction Assessment

In Figure 6, we assess the interaction effects between variables. We construct a two-dimensional (2-D) image where the axes are two of the explanatory variables and the color is the percentage of points that liquefied in each bin (bins are only shown for five or more observations). The bin width is chosen such that each explanatory variable is divided evenly into 19 bins. The observations (colored bins) are compared to the predicted probabilities (black lines) from bivariate models with or without interaction terms, which are represented as probability contour lines on the same image. When this plot is constructed for two explanatory variables without interaction terms, then the probability contour lines are straight. The interaction term allows for the probability contours to curve. Thus, if we add the interaction term and the contour lines are still essentially linear (and unchanged from the model without the interaction term) then we judge the interaction term to not be significant enough to include in the model.

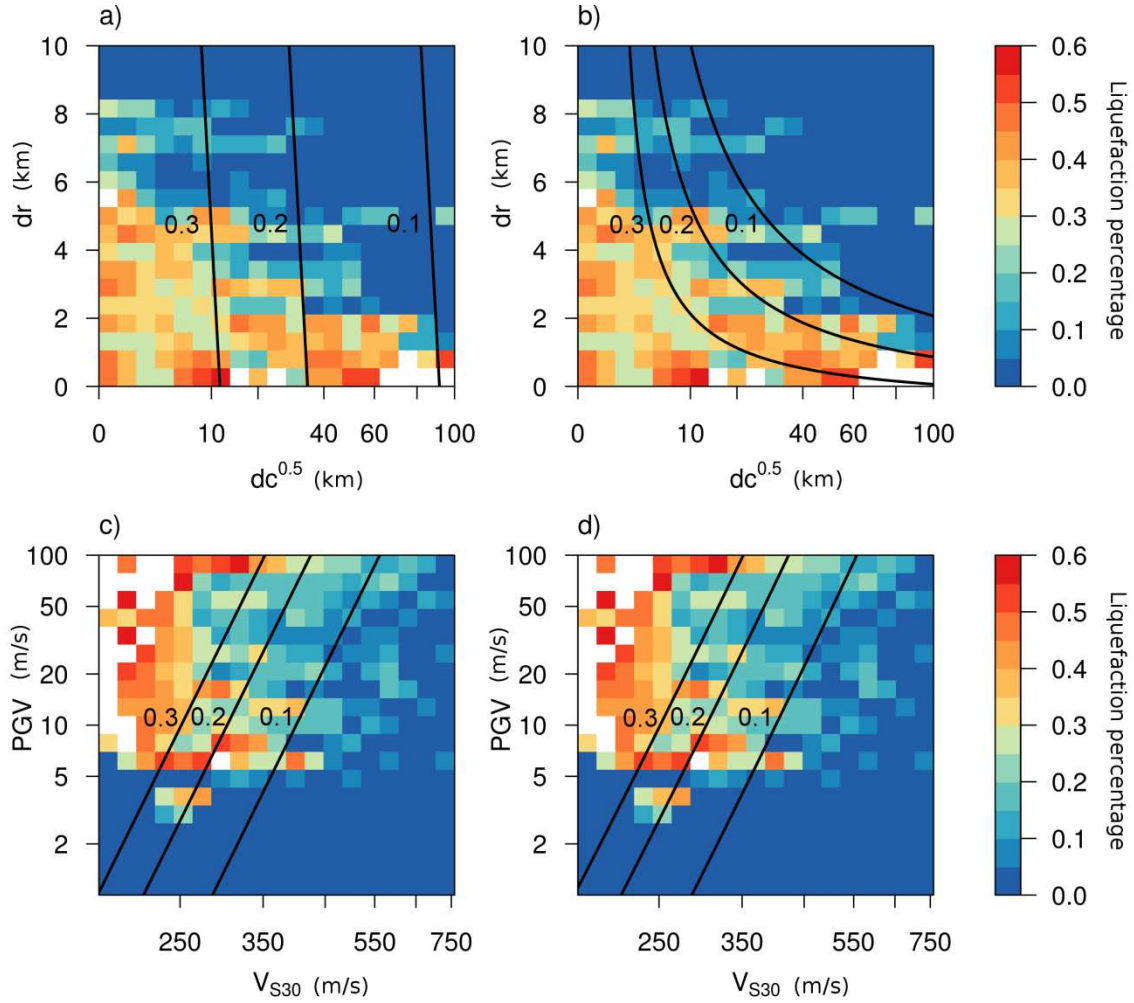


Figure 6 Observed percentage of liquefaction (colored bins) versus nonliquefaction as a function of  $dr$  and  $dc^{0.5}$  and comparison of probability contours (black lines) from a bivariate model a) without interaction term and b) with interaction term. Observed percentage of liquefaction (colored bins) versus nonliquefaction as a function of PGV and  $V_{S30}$  and comparison of probability contours (black lines) from a bivariate model c) without interaction term and d) with interaction term.

In this exploration, we only consider multiplicative interaction terms. We use the interaction between  $dc$  and  $dr$  as an example. When  $dc$  is small,  $dr$  has little effect on



the probability of liquefaction. When  $dc$  is large, the probability of liquefaction significantly decreases as  $dr$  increases. Note that  $dr$  does not appear to be a good predictor when it is evaluated alone (Figure 5g), but it becomes valuable when combined with  $dc$ . As shown in Figure 6b, after adding the interaction term, the probability contour lines become curved and fit the distribution of data better. This makes sense as we expect both saturation and soil density to change as the river approaches the coast. As a second example, we expect possible interaction effects between  $V_{S30}$  and PGV. When PGV is less than 3 cm/s, the probability of liquefaction is zero, and change in  $V_{S30}$  has no effect on the probability of liquefaction. We find adding the  $PGV \times V_{S30}$  interaction term does not help because the interaction terms does not create curvature in the model contours as shown in Figure 6. Instead, we heuristically assign zero to the predicted probability for both models when  $PGV < 3$  cm/s. Similarly, we assign zero to the probability when  $V_{S30} > 620$  m/s.

### 3.4.3 Model equations

After exploring individual candidate variables and their interaction effects, we select three variables to form a base model, which include  $\ln(PGV)$ ,  $\ln(V_{S30})$ , and precipitation. We choose these variables because they show strong correlation with the probability of liquefaction (Figures 5b, 5c, and 5n) and also can be linked to factors such as earthquake shaking, soil density, and regional climate, which are the primary contributors to the physical process of liquefaction. In addition, the model first relies on a preliminary classification based on PGV and  $V_{S30}$  as discussed above. As discussed above, we heuristically assign zero to the predicted probability for both models when  $PGV < 3$  cm/s. Similarly, we assign zero to the probability when  $V_{S30} > 620$  m/s.

A potential concern with the selection of PGV over the more traditional use of PGA with the MSF correction is that it does not explicitly account for the number of cycles of loading (or duration, which is generally correlated with magnitude). Within this context, we would like to note that the saturation of PGV scaling with magnitude is less severe than that for PGA. Thus, one could make the case that since PGV is more sensitive to magnitude than PGA, it indirectly accounts for the additional loading due to the longer durations associated with larger magnitudes. Another concern with the use of PGV is that GMPEs in some regions (especially stable continental regions and subduction zones) rarely include coefficients for evaluating PGV. We still prefer the use of PGV, however, because 1) it performs best when compared to our expanded database, 2) our assessment includes any additional uncertainty in PGV predictions, and 3) inclusion of PGV in GMPEs is becoming relatively standard in modern GMPEs and so we expect this issue to diminish with time.

Another significant contributor to the physical process of liquefaction is soil saturation; however, there were several candidate variables for soil saturation that show good correlation with the probability of liquefaction. Therefore, we focus on assessing the improved performance of the base model when saturation proxies are added as explanatory variables. We assess the performance of the model using the AUC and Brier score calculated from a sampled dataset. We use the same sampled dataset for all three models so that we can directly compare performance. The coefficients of the best performing model (Model 1) are given in Table 3. We also include the coefficients of the global model in Zhu et al. (2015), which uses magnitude-scaled PGA from ShakeMaps ( $PGA_{M,SM}$ ) to account for shaking load. The model performance as summarized by the AUC and Brier scores (shown in Table 3) was comparable across the current dataset: Model 1 has the highest AUC (0.801) as compared to Model 2 (0.788) and GLM-Zea15g (0.755); Model 1 has the lowest Brier score (0.162) as compared to Model 2 (0.166) and GLM-Zea15g (0.232).

Table 3. Coefficients of top performing coastal models and GLM-Zea15g. We heuristically assign zero to the predicted probability for both models when  $PGV < 3$  cm/s. Similarly, we assign zero to the probability when  $V_{S30} > 620$  m/s.

	GLM-Zea15g	Model 1	Model 2	Units
Intercept	24.10	12.435	8.801	
$\ln(PGV)$		0.301	0.334	cm/s
$\ln(V_{S30})$	-4.784	-2.615	-1.918	m/s
<i>precip</i>		5.556E-4	5.408E-4	mm
$\ln(PGA_{M, SM})$	2.067			g
$\sqrt{dc}$		-0.0287		km
<i>dr</i>		0.0666		km
CTI	0.355			
<i>dw</i>			-0.2054	km
<i>wtd</i>			-0.0333	m
$\sqrt{dc} * dr$		-0.0369		
AUC (All events*)	<b>0.755</b>	<b>0.801</b>	<b>0.788</b>	
Brier score (All events*)	<b>0.232</b>	<b>0.162</b>	<b>0.166</b>	
AUC (Noncoastal)	<b>0.655</b>	<b>0.793</b>	<b>0.811</b>	
Brier score ((Noncoastal)	<b>0.106</b>	<b>0.091</b>	<b>0.104</b>	

\*All events in Table 1 except the 2011 Bhuj earthquake.

### 3.4.4 Goodness of fit

The liquefaction data in the database are primarily derived from earthquakes that have occurred in coastal environments. There are not many earthquakes with observed liquefaction that occur far from the coast. Although Model 1 was developed from a database including both coastal and noncoastal earthquakes, it performs best in the coastal setting. Model 1 relies on the distance to coast parameter as a proxy for saturation and soil density, and we find this proxy can be problematic for the noncoastal setting because as the distance to coast increases, the predicted probabilities approach zero. Therefore, we present a second model (Model 2 in Table 3), which is selected from five top performing models and performs best in noncoastal events (defined earlier): 2008 Wenchuan, 1999 Chi-Chi, 1994 Northridge, and 1999 Hector Mine. Model 2 uses *wtd* and *dw* as the saturation proxies.

To compare the models in Table 3 and make sure that they are not biased toward a specific event, we summarize the AUCs of models on individual events in Table 4. Events with no liquefaction are excluded in the table because both liquefaction and nonliquefaction are needed in order to compute AUC. Both updated models perform well on 16 earthquakes (out of 21 liquefaction earthquakes) with AUC values greater than 0.6. We compare the AUCs of the two updated models, and bolded numbers in the table shows the AUC of the better performing model in the two updated models for each event. Although Model 1 performs better than Model 2 overall, Model 2 outperforms Model 1 on all noncoastal events. Model GLM-Zea15g outperforms updated models for the 2003 San Simeon, 2004 Niigata, 2003 Tokachi, and 2001 Bhuj events. Both updated models perform poorly ( $AUC < 0.6$ ) for the 2008 Wenchuan, 2001 Bhuj and 1994 Northridge events. For the 1965 Puget Sound event, many liquefaction cases with low probabilities from Model 1 occurred in the artificially filled areas that were not well captured by the geospatial parameters. In Figure 7, we compare the ROC curve of the updated model with the previous model in Zhu et al. (2015). The AUC of the updated Model 1 and GLM-Zea15g is 0.801 and 0.755, and the brier score of the updated Model 1 and GLM-Zea15g is 0.162 and 0.232, suggesting that the new model provides improved accuracy over the old model.

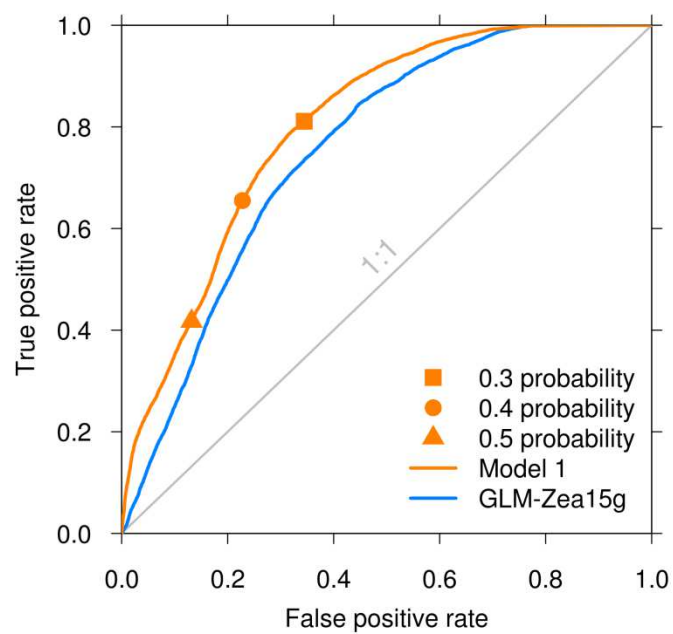


Figure 7. Comparisons of ROC curves of GLM-Zea15g and the best performing model (Model 1) with a one-to-one line representing random guessing.

Table 4. Comparison of the AUCs of two updated models and GLM-Zea15g over individual earthquakes. Bolded numbers indicate the AUC for the better performing model in Model 1 and Model 2. When comparing three models, GLM-Zea15g outperforms the two updated models for six earthquakes.

Earthquake	GLM-Zea15g	Model 1	Model 2
1989 Loma Prieta	0.620	<b>0.886</b>	0.848
1995 Kobe	0.808	<b>0.862</b>	0.821
2000 Tottori	0.771	<b>0.806</b>	0.775
2011 Christchurch	0.847	<b>0.801</b>	0.770
1978 Miyagi	0.742	0.791	<b>0.801</b>
2003 San Simeon	0.786	0.757	<b>0.775</b>
2010 Darfield	0.642	<b>0.725</b>	0.692
2001 Nisqually	0.684	0.703	<b>0.751</b>
2004 Niigata	0.728	0.678	<b>0.700</b>
2011 Tohoku	0.532	<b>0.677</b>	0.656
1993 Hokkaido	0.711	0.673	<b>0.720</b>
1964 Niigata	0.668	<b>0.667</b>	0.628
1983 Nihonkai	0.647	0.643	<b>0.649</b>
1987 Chiba	0.613	0.608	<b>0.657</b>
1999 Chi-Chi*	0.568	0.603	<b>0.660</b>
1949 Puget Sound	0.578	0.601	<b>0.610</b>
2003 Tokachi	0.578	0.561	<b>0.571</b>
1965 Puget Sound	0.529	<b>0.558</b>	0.548
1994 Northridge*	0.469	0.535	<b>0.547</b>
2008 Wenchuan*	0.546	0.527	<b>0.551</b>
2001 Bhuj*	0.638	0.515	<b>0.537</b>

\*noncoastal events (average distance to coast of liquefaction features > 20 km)

To convert the model to a classifier, we must select a threshold value to convert from predicted probability to a classification of liquefaction or nonliquefaction. Lower thresholds yield higher true positive rates and higher false positive rates. The threshold value could be determined based on the highest acceptable false positive rate. Using the top performing model (Model 1), we present confusion matrices for three thresholds in Table 5. A confusion matrix summarizes statistics for four possible outcomes when comparing a prediction from a binary classifier to an observation: true positive (top left cell; correct

positive prediction), true negative (bottom right cell; correct negative prediction), false positive (bottom left cell; incorrect positive prediction) and false negative (top right cell; incorrect negative prediction). For example, using 0.3 as the threshold, 24.2% of data liquefied and are correctly classified as liquefaction. 5.6% of the data liquefied and are incorrectly classified as nonliquefaction. Using 0.3 as the threshold gives a true positive rate (TPR; the fraction of positive cases that are correctly classified) of 0.81 whereas as a threshold of 0.4 give a true positive rate of 0.65 and a threshold of 0.5 reduces the true positive rate further to 0.42. The false positive rate (FPR; the fraction of negative cases that are incorrectly classified as liquefied) is 0.34 with a threshold of 0.3, 0.23 with a threshold of 0.4, and 0.13 with a threshold of 0.5. These differences in TPR and FPR for different thresholds help to illustrate the effectiveness of the classifier and the meaning of the mapped categories when we use this model to map the probability of liquefaction for an event (Figure 8 and Figure 9). A threshold of 0.3 is more conservative in that it overpredicts liquefaction, whereas, a threshold of 0.4 is a more balanced classifier.

Table 5. Confusion matrices for three thresholds (0.3, 0.4, and 0.5) for Model 1 presented in

Table 4.

Threshold		P = 0.3		P = 0.4		P = 0.5	
Predicted		L	NL	L	NL	L	NL
Actual	L	24.2	5.6	19.6	10.3	12.5	17.4
	NL	24.1	45.9	16.0	54.0	9.2	60.8
		TPR=	0.81	TPR=	0.65	TPR=	0.42
		FPR=	0.34	FPR=	0.23	FPR=	0.13

### 3.4.5 Probability maps

In addition to the performance metrics, it is also important that the model predicts the spatial distribution of liquefaction for the earthquake event. Figure 8 and Figure 9 show the predicted probability maps (using Model 1) for three U.S. and five Japan earthquakes where the observed liquefaction points are shown in black. The spatial pattern of liquefaction for each event is well represented by the model. Consistent with the confusion matrix, the orange and red categories (threshold  $>0.3$  and threshold  $>0.5$ ) show a consistent pattern with the observed liquefaction. We find for earthquakes with very large magnitude such as the 2011 Tohoku earthquake, the model predicts larger area of high probabilities than the area where liquefaction was observed. This might be related to the fact that the observed probability of liquefaction saturates as a function of  $\ln(\text{PGV})$  for large PGV values, but the predicted probability does not (Figure 5b). The saturation is more severe when using  $\ln(\text{PGA})$  as the shaking parameter.

In Figure 10, we show the probability maps calculated using Model 2 for the four noncoastal earthquakes in the database (2008 Wenchuan, 1994 Northridge, 1999 Hector Mine, and 1999 Chi-Chi). We also show the model applied to the 2001 Bhuj and 2015 Nepal earthquakes, which are not in the database as a further verification of the model. The model performs well on the 1999 Hector Mine and the 2015 Nepal events. For the 2008 Wenchuan earthquake, the liquefaction generally occurred near rivers, which coincide with low probability (0.1-0.3) and some medium probability (0.3-0.5) areas predicted by the model. For the 1994 Northridge earthquake, in the epicentral region in the San Fernando Valley, the model appears to overpredict because the liquefaction data in our database for this region is incomplete. Besides the ground failures in the region that are shown in the figure and included in our database, liquefaction was also found to contribute to many liquefaction-related structural failures (Stewart et al., 1994). In the Granada Hills area on the north of the San Fernando Valley where many ground failures were observed, the model predicts

low



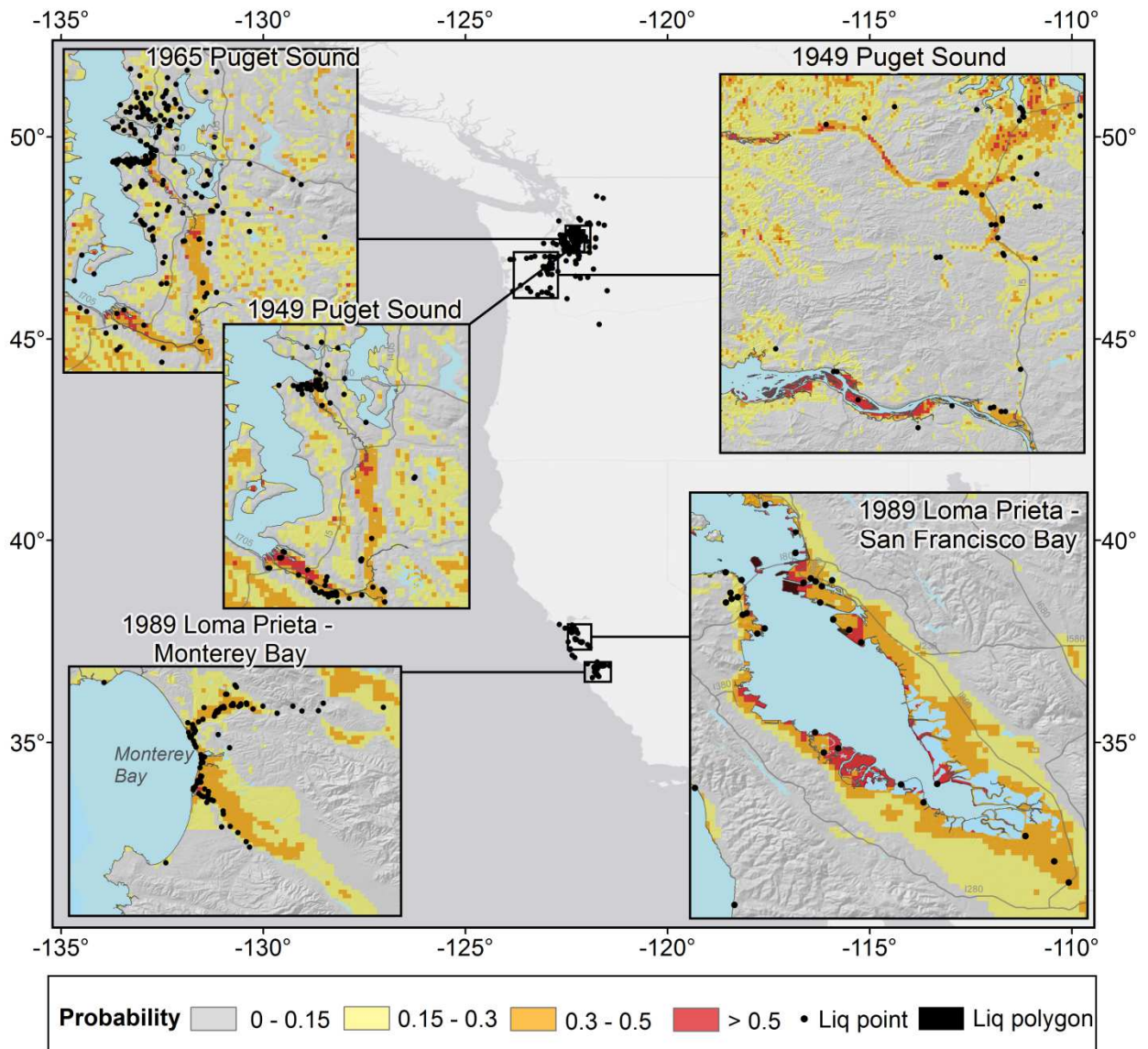


Figure 8. Probability maps predicted from the updated model (Model 1) for earthquakes in United States.

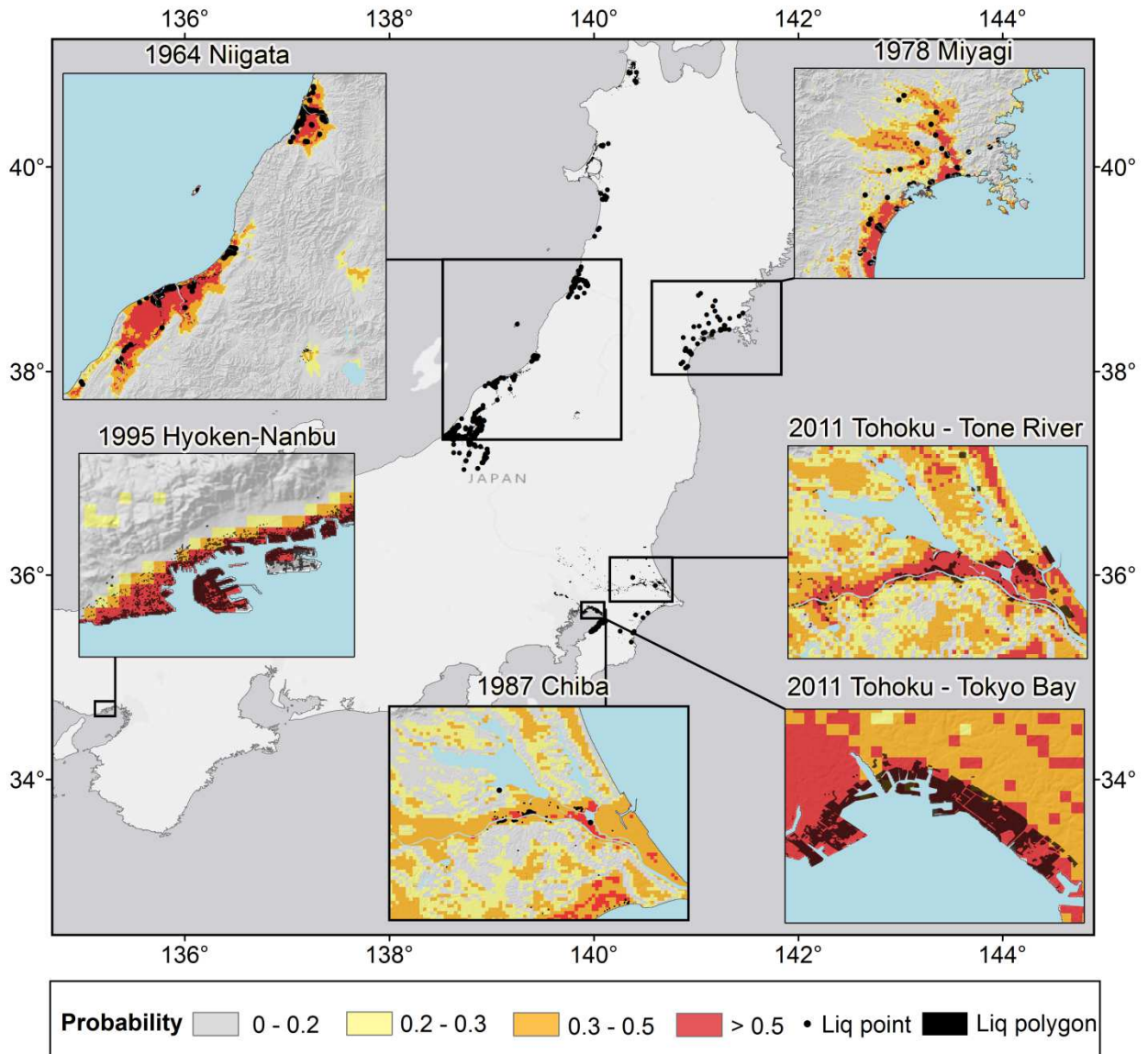


Figure 9. Probability maps predicted from the updated model (Model 1) for earthquakes in Japan.

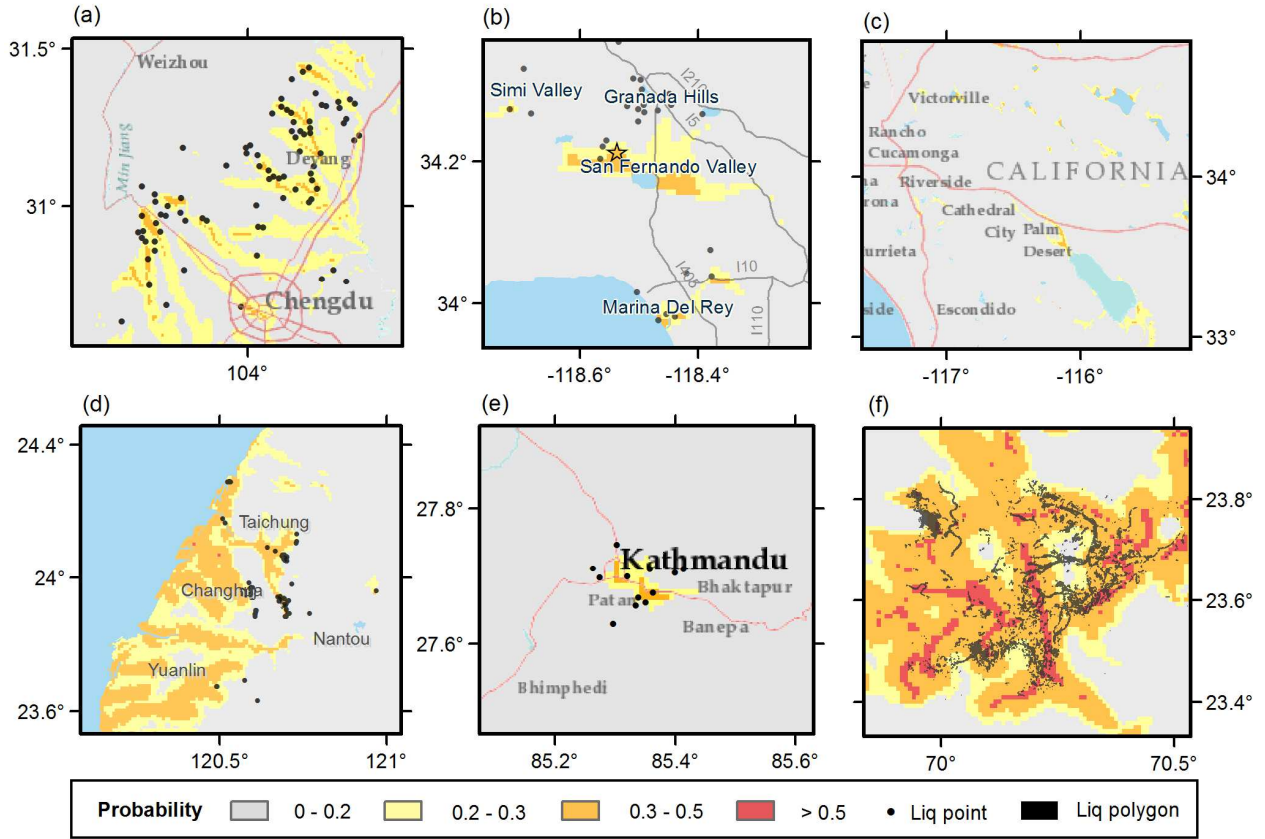


Figure 10. Probability maps predicted from Model 2 for a) the 2008 Wenchuan, b) 1994 Northridge, c) 1999 Hector Mine, d) 1999 Chi-Chi, e) 2015 Nepal (Moss et al., 2015), and f) 2001 Bhuj earthquakes.

probabilities as a result of the relatively deep water table depth ( $>10\text{m}$ ). The observed ground failures in the area might be a result of dynamic ground compaction of loose unsaturated surface material not liquefaction (Stewart et al., 1994). Outside of the San Fernando Valley, the model predicts high probabilities in Simi Valley on the west and the coastal area near Marina De Rey on the south, which agree with the liquefaction observations. For the 1999 Chi-Chi event, many observed liquefaction points lie in the area with medium probability. The model overpredicts for coastal areas, where very few liquefaction occurrences were observed. For the 2001 Bhuj event, model

prediction in general agrees with the extent of liquefaction estimated from change detection on remote sensing data. Notwithstanding the above limitations in identifying individual locations of liquefaction observations, it is our interpretation that the aggregate performance of the events in Figure 10 is encouraging for a number of reasons: 1) these are the most challenging events that the model is likely to face due to the fact that liquefaction occurred in noncoastal areas whereas the majority of the events in the database are located in coastal areas, 2) the extent of the observations correlates well with the extent/amplitude of the modeled probabilities (i.e., the model indicates the overall extent of liquefaction for an event even if the exact locations are not identified), and 3) with the exception of prior models developed by our research team, there are currently no feasible alternative models of liquefaction that can be applied globally, and we have shown that this update is a significant improvement over our prior models elsewhere in this paper.

#### **3.4.6 Application for susceptibility**

Maps of liquefaction susceptibility which are independent of a specific earthquake scenario may also be useful for regional liquefaction risk estimation. The probability of liquefaction is a function of the set of explanatory variables  $X$  in equation (1), which includes the event-specific shaking intensity. To create a susceptibility map, we simply compute  $X$  without the intensity (PGV) term. The resulting number is not an estimate of the probability of liquefaction, but simply combines the susceptibility terms together with the coefficients that were determined by our regression analysis. Thus, the absolute values are not directly meaningful. We calculate the susceptibility using Model 1, and present the susceptibility as three classes (low, moderate, and high) in Figure 11 for the San Francisco region as compared to a geology-based susceptibility map (Witter et al., 2006). Figure 12 shows a similar comparison between



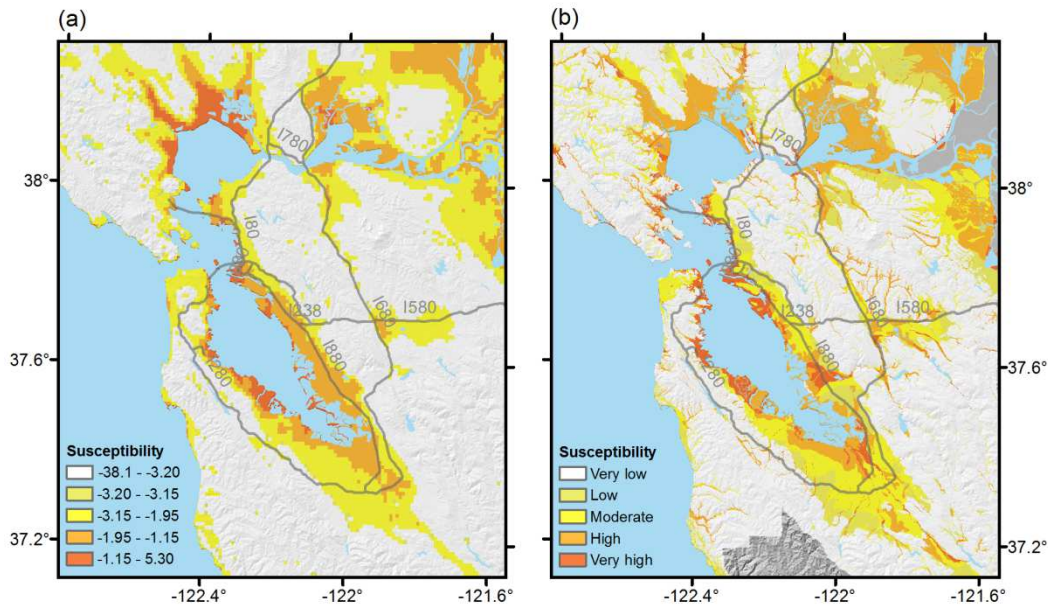


Figure 11. Susceptibility maps for the San Francisco Bay, California area from a) the geospatial model (Model 1) and b) geology-based mapping (Witter et al., 2006).

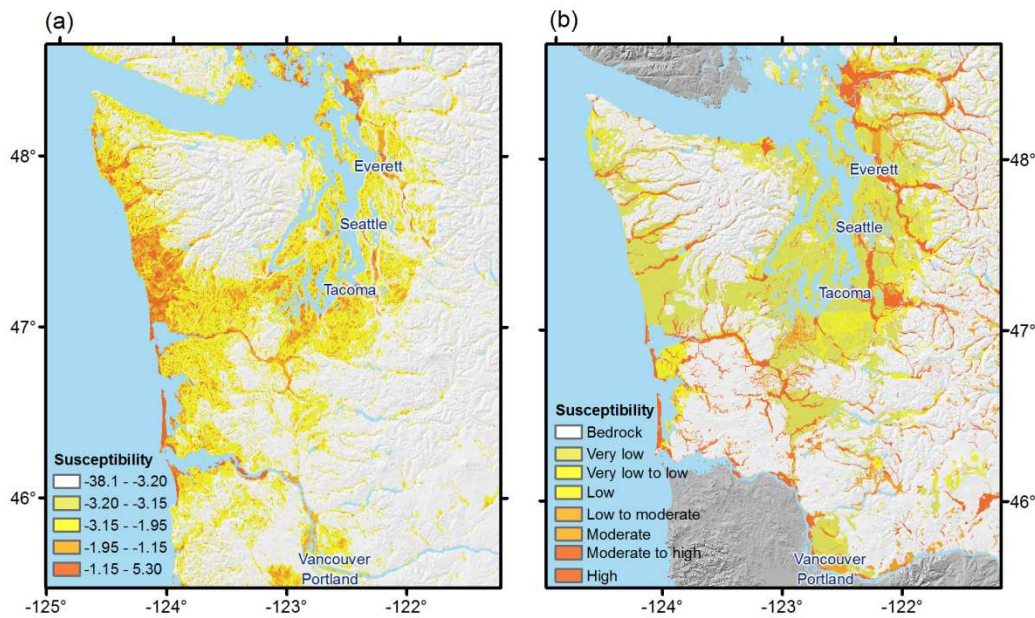


Figure 12. Susceptibility maps for the Seattle, Washington area from a) the geospatial model (Model 1) and b) geology-based mapping (Palmer et al., 2004).

a geospatial susceptibility map versus a geology-based susceptibility map for Seattle (Palmer et al., 2004). Although there are some differences between our model and the

geology-based susceptibility maps, we are able to capture similar trends and believe that these geospatial susceptibility maps can be useful as preliminary information for regional-scale planning.

### **3.5 Discussion**

#### **3.5.1 Sensitivity Analyses of Sampling Choices**

In this study, we apply a sampling method<sup>7</sup> in order to combine complete and incomplete datasets into a single database. The resulting method results in a balanced dataset (50:50). To fully understand the implications of our sampling method, we perform sensitivity analyses regarding choices such as the width of the spatial buffer and the class imbalance. Note that in the sensitivity analyses we use a different dataset than what is described in the methods section, which was used for regression. We use a testing dataset that is independent of the sampling method, which consists of all data points from the “complete” datasets as defined in Table 1. For example, 0.5 – 10 km means we sample nonliquefaction points within the area that is greater than 0.5 km and less than 10 km from observed liquefaction. We develop models using data that are sampled using different buffer widths. We compare the performance of the models in terms of the ROC curve in Figure 13a, and find the AUCs of the models are not sensitive to the buffer widths. The ROC curves in Figure 13 are different from the ROC curve in Figure 7 because different testing data are used. Figure 13 shows that the model performs well on spatially complete events that are used for testing. Similarly, we study the sensitivity of model performance to the class imbalance as shown in Figure 13b. We compare the models that are developed using the data sampled using different liquefaction/nonliquefaction ratios, and we find the AUCs of the models are not sensitive to the class imbalance.

### 3.5.2 Interpretation of the Predicted Probabilities

The predicted probability from the developed models can be converted to a classification by applying a threshold as demonstrated with the confusion matrix presented in Table 5. This is useful for predicting liquefaction for a new event. Optimal thresholds can be chosen based on the acceptable false predictions. Another way to interpret the probability is to predict the spatial extent of liquefaction within a probability class. In the development of the Zhu et al. (2015) model, which used spatially complete data, the predicted probabilities agreed well with the spatial extent. Figure 14 assesses the relationship between the areal percentage of liquefaction computed with the complete events in the expanded inventory database and the predicted probabilities from GLM-Zea15g and Models 1 and 2. For each model, we bin the predicted probability and compute the liquefaction percent, which is plotted in

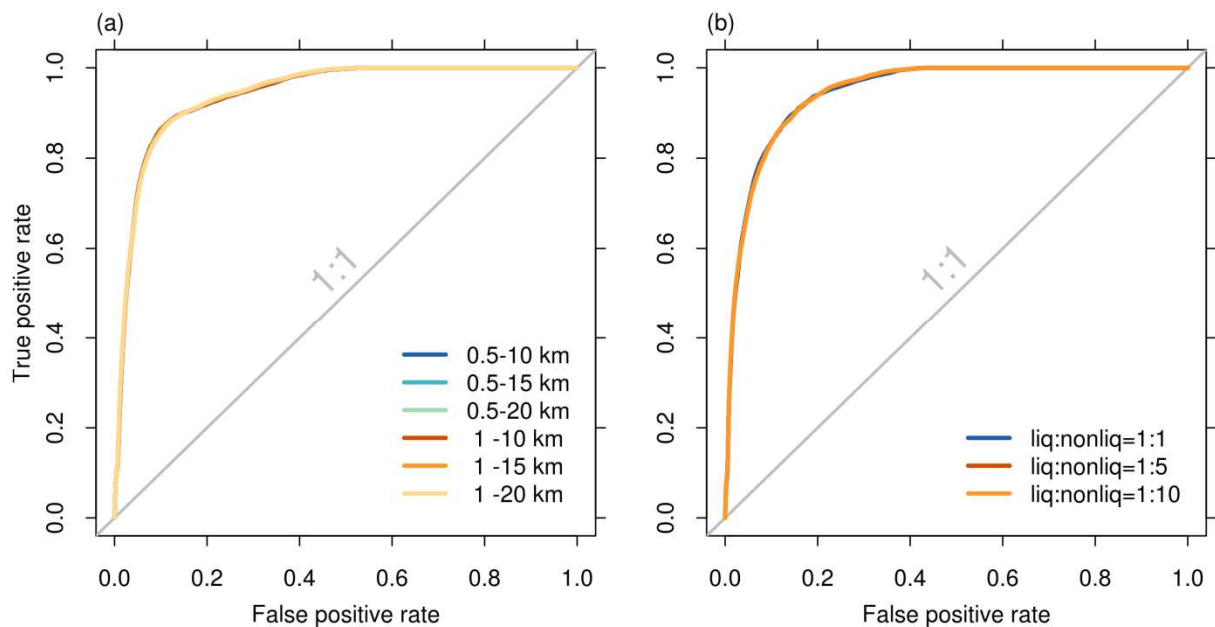


Figure. 13 Sensitivity of ROC curves to a) spatial buffer and b) class imbalance with one to one lines (gray lines) representing random guessing.

Figure 14 in the center of each bin, and the 95% confidence interval is illustrated as a vertical line. For GLM-Zea15g, we show a linear model with a 0 intercept and a slope of 0.81. This means that the expanded database indicates that the probabilities from the GLM-Zea15g model should be multiplied by 0.81 to estimate liquefaction percent. Note that we have included more events with insignificant or no liquefaction, which explains why the slope of this line is not unity even though that was the target of GLM-Zea15g. For Model 1 and Model 2, we fit a logistic function which has the same form as Equation 1 except that in this case we found that squaring the denominator improves the fit

$$L(P) = \frac{a}{(1+be^{-cP})^2} \quad (2)$$

where  $L$  is the areal liquefaction percent,  $P$  is the predicted probability, and the parameters  $a$ ,  $b$ , and  $c$  are given in Table 6. Equation 2 can either be used to convert the predicted probability to liquefaction percent or to define simplified classes. For example, to define a class where the percent liquefaction is between 10 and 20% from the probabilities predicted by Model 2, one would plug in the value of 10 and 20 for  $L(P)$  into Equation 2 and solve for  $P$  with the Model 2 coefficients from Table 6, which would yield probabilities of 0.37 to 0.47.

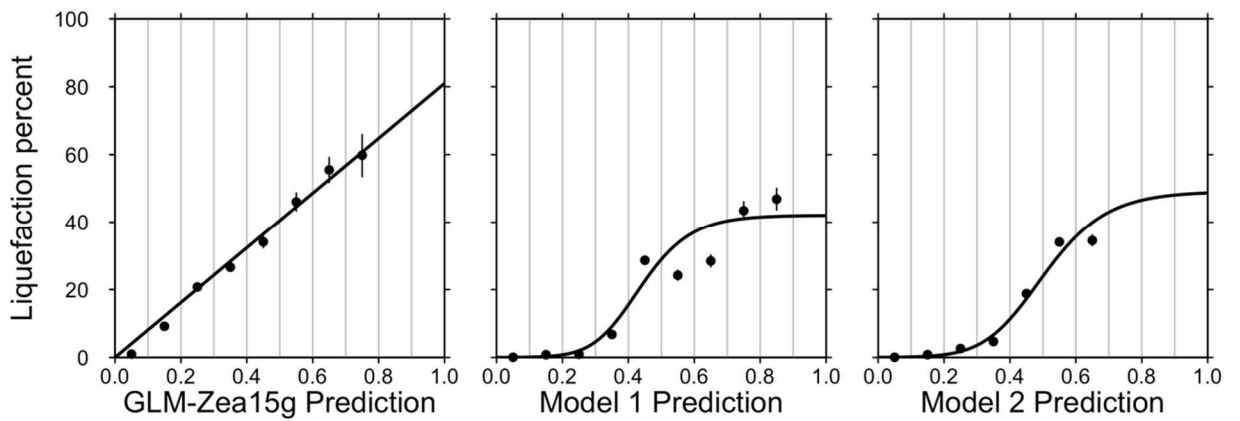


Figure 14. Areal percentage of liquefaction as a function of model probabilities. In each panel, the dots show the estimated liquefaction percent with 95% confidence intervals for binned predicted probabilities. Vertical lines indicate the bin boundaries. The black lines are curves fit to the data.



Table 6. Parameters for relating model probabilities to areal liquefaction percent.

	Model 1	Model 2
a	42.08	49.15
b	62.59	42.40
c	11.43	9.165

### 3.5.3 Applicability of Model to Noncoastal Regions

While the goal of the geospatial liquefaction model presented here is for global use, we acknowledge that the model development was based on earthquakes in coastal regions. Our analysis of Model 2 in noncoastal regions provides promising results; however, uniform performance across all tectonic environments should not be expected. For example, the accuracy of predicting  $V_{S30}$  from slope may be less accurate in glaciated regions (Magistrale et al. (2012)). Model validation and development should continue as earthquakes occur and additional data become available.

## 3.6 Conclusion

To predict liquefaction extent immediately after an earthquake worldwide, we need a model that uses widely available geospatial parameters (e.g., Zhu et al. (2015)). In this paper, we update the Zhu et al. (2015) model by 1) expanding the database to include 27 events from six countries, 2) applying a sampling method to add incomplete dataset, 3) evaluating new explanatory variables, and 4) testing interaction terms. In model development, we compare 18 proxies for earthquake shaking, soil saturation and soil density. We find PGV performs better than PGA as a shaking parameter. The patterns of saturation proxies show different scales of details. At a regional scale, distance to the water body performs best. We find that considering interaction terms

between  $dr$  and  $dc$  improves the accuracy of the model. The model that performs best over the entire dataset includes PGV,  $V_{s30}$ ,  $dr$ ,  $dc$ , and precipitation. The model that performs best over the noncoastal dataset includes, PGV,  $V_{s30}$ ,  $wtd$ ,  $dw$ , and precipitation. The updated models offer an improved accuracy as compared to the Zhu et al. (2015) model. We validate the models and assess the resulting probability in terms of probability thresholds and the spatial extent of liquefaction. We find that the mapped probability of liquefaction can be used as an estimate of spatial extent within classes but should be adjusted due to the 50:50 class balance used herein. Overall, the footprint and overall degree of liquefaction is successfully recovered for test events to a degree that indicates our models should prove useful for global, near-real-time applications.

### 3.7 Data and Resources

The liquefaction data used in this paper were all compiled and digitized from published sources (listed in the references in Table 1) except the data for the 2010-2011 Darfield and Christchurch earthquakes from the Canterbury geotechnical database (<https://canterburygeotechnicaldatabase.projectorbit.com>; last accessed July 2014). The liquefaction data that we digitized for ten earthquakes in the US, Japan, China, and Taiwan are available from Zhu et al. (2016). The electronic data from all of the events in Table 1 where the reference is Wakamatsu (2011) is available in the CD that accompanies the book.

The ShakeMaps were obtained from the USGS earthquake archives (<http://earthquake.usgs.gov/earthquakes/search/>; last accessed April 2015). The digital elevation model was obtained from the Global Multiresolution Terrain Elevation Data 2010 ([http://topotools.cr.usgs.gov/gmted\\_viewer/viewer.htm](http://topotools.cr.usgs.gov/gmted_viewer/viewer.htm); last accessed December 2013). River networks and compound topographic index data were obtained from the HydroSHEDS database (<http://hydrosheds.cr.usgs.gov/dataavail.php>; last accessed

February 2014). Distance to the nearest coastline data were computed from the Distance to the Nearest Coast dataset (<http://oceancolor.gsfc.nasa.gov/cms/DOCS/DistFromCoast#>, last accessed January 2014). Mean annual precipitation data were obtained from the WorldClim database (<http://WorldClim.org>; last accessed March 2014). The aridity index data were obtained from the Global Aridity and PET dataset (<http://www.cgiar-csi.org/data/global-aridity-and-pet-database>; last accessed September 2014).

Analysis on geospatial datasets were performed using the Generic Mapping Tools software (<http://www.soest.hawaii.edu/gmt/>; Wessel and Smith, 1998) and the Geospatial Data Abstraction Library, available at <http://www.gdal.org/>. All other computations in this article were completed with the open source software R (R Development Core Team, 2012) available at <http://www.r-project.org/>. Figures were prepared using R and Geographic Information System program ArcGIS, v.10.

### **3.8 Acknowledgement**

This work was supported under National Science Foundation Grant Numbers 1300781 and the United States Geologic Survey, Department of the Interior, under USGS award number G16AP00014; we gratefully acknowledge this support. The views and conclusions contained in this document are those of the authors and should not be interpreted as necessarily representing the official policies, either expressed or implied, of the U.S. Government. The work has greatly benefited from discussions with David Wald and Keith Knudsen at the United States Geologic Survey. This work benefited from reviews by Kate Allstadt, David Wald, and two anonymous reviewers, as well as informal discussions with Ken Campbell.

## 4 Mapping Earthquake Induced Liquefaction Surface Effects from the 2011 Tohoku Earthquake Using Satellite Imagery<sup>3</sup>

### Abstract

Earthquake induced soil liquefaction is an important secondary hazard during earthquakes and can lead to significant damage to infrastructure. Mapping liquefaction surface effects after an earthquake is an important component of post-event data cataloging. These liquefaction inventories are then used by researchers to investigate the causes and effects of soil liquefaction. Post-earthquake liquefaction data collection historically relies on field investigation. Because the spatial extent of field investigations is often limited by time and expense, many areas where liquefaction may have occurred are neglected, and the resulting liquefaction inventories are often spatially limited and incomplete. The use of pre- and post-earthquake satellite images can enable spatially continuous/exhaustive mapping of liquefaction that can subsequently be checked by field investigation and visual interpretation of true color composite satellite images or high resolution aerial imagery. We develop a workflow for mapping earthquake-induced surface effects of liquefaction using optical satellite images from the WorldView-2 satellite with 2 m spatial resolution and eight spectral bands. We use an approach that combines change detection with inputs that are sensitive to surface moisture and soil characteristic and supervised classification. We find that change vector analysis using the change magnitude based on the components of the Tasseled Cap Transformation is more effective than using individual spectral bands alone. We test and verify the proposed method in the Urayasu region in Japan affected by the 2011 Tohoku earthquake, comparing the

---

<sup>3</sup> Zhu, J., L. G. Baise, M. Koch (in preparation). Mapping Earthquake Induced Liquefaction Surface Effects from the 2011 Tohoku Earthquake Using Satellite Imagery, *Soil Dyn. Earth. Eng.*

results of the proposed automated classification with an existing dataset visually mapped from aerial photographs. The preferred classification uses the decision tree classification with the change of magnitude, wetness, and NDWI and results in a producer's accuracy for liquefaction of 70% within the training dataset. The decision tree is applied across Urayasu City using a mask to block out buildings and vegetation. The results are qualitatively evaluated at several locations indicating that liquefaction surface effects can be identified on exposed surface such as bare soil and pavement but may not be visible on the high-resolution images in dense urban areas where buildings, and shadows obstruct the satellite view.

## 4.1 Introduction

Soil liquefaction often occurs as a secondary hazard during earthquakes and can lead to significant infrastructure damage. Liquefaction hazard on a regional scale can be mapped for loss estimation and rapid response using predictive models (e.g., Zhu et al 2016). Mapping liquefaction surface effects after an earthquake is important in both guiding emergency response and providing an inventory of liquefaction from the event. These inventories are then used by researchers to study soil liquefaction, refine and validate liquefaction models, and ultimately mitigate liquefaction-related damage for future events. Post-earthquake liquefaction data collection historically relies on field investigations carried out by reconnaissance teams such as the Geotechnical Extreme Events Reconnaissance (GEER) teams. Field reconnaissance teams investigate sites with reported liquefaction surface effects, and as a result, the liquefaction inventories are often severely biased toward liquefaction observations. Because the spatial extent of this type of investigation is often limited by time and expense, many areas where liquefaction may have occurred are neglected (Chleborad and Chuster, 1990; Youd and House, 1978). A spatially complete and unbiased catalog of liquefaction surface effects is critical for evaluating spatial extent of liquefaction. Zhu et al. (2016) have demonstrated that regional liquefaction models can be developed to predict spatial extent of liquefaction when spatially complete liquefaction inventories are available; however, complete liquefaction inventories are rare as they require the integration of detailed interpretation of aerial images and field reconnaissance. To improve the size and scope of liquefaction inventories, we need an approach that supplements field reconnaissance with classification from high-resolution satellite imagery to document liquefaction surface effects after an earthquake over broad regions.

Over the past decade, significant progress has been made in developing and launching high resolution spaceborne optical imaging sensors such as the WorldView-2 (WV-2; launched 2009) and Pléiades-1A (launched in 2011). WorldView-2 produces images with 2 m spatial resolution and eight spectral bands. These sensors provide great opportunities for timely and accurate mapping of post-earthquake damage. Remote sensing imagery can greatly benefit field reconnaissance in reducing spatial incompleteness and sampling bias in the liquefaction data collection. Compared with field investigations, remote sensing imagery is cost effective and can be collected over a broad region, including locations that are not accessible by field personnel. Furthermore, satellite imagery can be used to produce a spatially continuous map, and thus unbiasedly preserve observations of both liquefaction occurrence and nonoccurrence.

Remote sensing imagery has been integrated into post-earthquake liquefaction data collection for some recent earthquakes such as the 2001 Bhuj (Ramakrishnan et al 2006), 2011 Christchurch, New Zealand earthquake (Cubrinovski et al., 2011; Green et al., 2011), and the 2011 Tohoku earthquake (Toida and Yazamaki, 2012). Many of these applications (Toida and Yamazaki, 2012; Hamada et al., 1995) relied on visual interpretation using aerial photos with limited spectral information, which can be expensive and time consuming (Saito et al 2005). Using more spectral information combined with automated image analysis methods such as change detection or classification can greatly increase detectability of ground affected areas while reducing cost and efforts and have been used by some researchers (Oommen et al, 2013; Morgenroth et al., 2016). Morgenroth et al. (2016) has applied a rule-based classification on air-borne imagery acquired after the 2011 Christchurch earthquake. While their study demonstrates the feasibility of using an automated algorithm to map the surface effects of liquefaction based on a single post-event image, their model did

not perform well on pavements due to the spectral similarity between wet liquefaction and nonliquefied pavements. The proposed method extends their work by incorporating spectral change information between pre- and post-earthquake images. Oommen et al. (2013) has applied change detection using Landsat ETM+ data to map liquefaction surface effects in rural regions for the 2001 Bhuj earthquake based on a spectral variable that is sensitive to soil moisture content. In the proposed method herein, we extend the change detection method used by Oommen et al. (2013) by applying it in Urayasu City for the 2011 Tohoku earthquake using WorldView-2 imagery. By using the WorldView-2 data, we have a higher spatial resolution (2 m) and more spectral bands in the visible and near infrared region of the spectrum than the Landsat ETM+ data. In this study, we test and combine multiple variables (e.g. brightness, greenness, and wetness from the Tasseled cap transformation) in the change detection and classification to map liquefaction.

The objective of this Chapter is to investigate the applicability of a change detection analysis in combination with a supervised classification method in an urban environment to identify liquefaction-induced surface effects. The study area is Urayasu city in Japan which is heavily damaged after the 2011 Tohoku earthquake. We take advantage of the very high spatial resolution optical satellite images (WorldView-2) for Urayasu City in Japan before and after the 2011 Tohoku earthquake. We use eight spectral bands from the WorldView-2 data and their transformations in the change detection and classification. We validate the method across 4000 validation points in Urayasu City where liquefaction surface effects have been visually mapped by others (Toida and Yamazaki 2012), and independently validated by us using the post-earthquake WorldView-2 image displayed in true color composite. We evaluate individual spectral bands from WorldView-2 as well as spectral variables from the Tasseled cap transformation in the change detection. We



compare two supervised classification methods (decision tree and maximum likelihood classification) to map liquefaction and nonliquefaction within the test areas. Finally, we select a classification method based on accuracy metrics and apply the preferred classification method based on accuracy metrics across Urayasu City. In addition to the quantitative validation, we use the true color composite to qualitatively evaluate the classification performance because it is created by combining the spectral bands (visible red, blue green bands) that most closely resemble the range of vision of the human, and we find it easier to identify liquefaction surface effects than other band combinations. The qualitative evaluation is used to understand the model performance as compared to field mapping and to provide insight into future implementations of satellite-imagery based liquefaction mapping classifications.

## **4.2 Study Area and Data**

The study area is the Urayasu City in Chiba Prefecture, a densely populated urban region, located on the coast of Tokyo Bay in Japan. A map of this region is shown in Figure 1a. The city was built on land that was reclaimed between 1966 and 1985 (Yasuda et al 2012). The strong ground motion resulting from the 2011 Mw 9.0 Tohoku earthquake, combined with the soil condition and the shallow water table depth resulted in extensive liquefaction across Urayasu City. Many houses, roads, lifeline facilities, and river embankments were severely damaged by soil liquefaction. Surface effects due to liquefaction were widely observed both on soil and pavement (Bhattacharya et al 2011).

Liquefaction surface effects such as sand boils, ejected sand, and standing water were captured by a high-resolution WorldView-2 sensor that overpassed the affected area one week after the event. In this study, we use two WorldView-2 (WV-2) images before and after the Tohoku earthquake occurred on March 11, 2011 to identify

changes of the land surface in Urayasu due to soil liquefaction. The details of the images are summarized in Table 1. The spatial resolution is 0.5 m for panchromatic bands and 2 m for multispectral bands. The sensor measured radiance in eight multispectral bands distributed along the visible to near-infrared range of wavelengths (400 nm – 1040 nm).

Liquefaction surface effects in the Urayasu region have been mapped by several studies (MLITT 2011, Toida and Yamazaki 2012). A field survey was conducted by MLITT (2011) immediately after the event and resulted in a map of each road segment within Urayasu City classified as liquefied or not. Toida and Yamazaki (2012) also created a liquefaction map by visual inspection using aerial photos at 25cm resolution taken six days after the earthquake. The Toida and Yamazaki (2012) map is shown in Figure 1b, and shows mapped liquefaction as polygons. In an urban area, liquefaction inventories are limited to the visible surface including parking lots, soil, sidewalks, and roads. Buildings and vegetation can create holes in the dataset.

The Toida and Yamazaki (2012) data were created from visual inspections, and were not field-validated for the entire region. In order to develop a high quality validation dataset, we choose to visually validate the liquefaction data from Toida and Yamazaki (2012). Because the original digital files of the liquefaction map depicted in Figure 1 in Toida and Yamazaki (2012) are not publicly available, we extracted the liquefaction data from this figure by first georeferencing it, and then digitizing the liquefaction marked areas from the figure. Rather than using the entire region depicted on this map, we choose to randomly select 4000 locations (2000 liquefaction points and 2000 nonliquefaction points) within Urayasu city where we could visually confirm the results (liquefaction or nonliquefaction) from Toida and Yamazaki (2012) using the post-earthquake WV-2 image displayed in true color composite (red, green, blue

bands). We dismiss any locations where the ground surface was not visible (obstructed by buildings or tree crowns) and/or we could not visually confirm the liquefaction occurrence or nonoccurrence from WV-2 images. By vetting the validation points against the true color composite, we could evaluate the proposed supervised classification methods against high quality validation data.

Table 1 Summary of the satellite images and their characteristics

	Date	Sensor	Spatial resolution	Radiometric resolution
Pre-event*	2011/02/13	WorldView-2	Pan:0.5m, Multispectral: 2m	Coastal (400–450 nm), Blue (450–510 nm), Green (510–580 nm), Yellow (585–625 nm), Red (630–690 nm), Red Edge (705–745 nm), NIR1 (770–895 nm), NIR2 (860–1040 nm), Pan (450–800 nm).
Post-event*	2011/03/18	WorldView-2		

\*The Tohoku earthquake occurred on March 11, 2011.

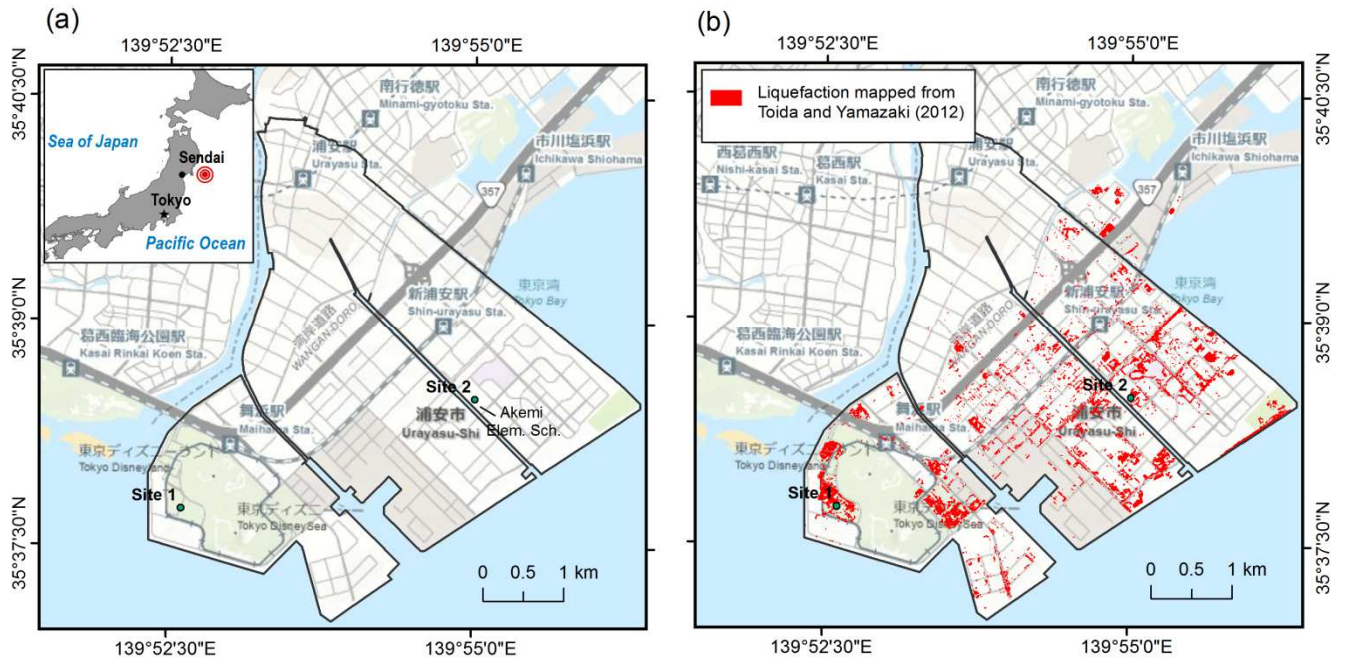


Figure 1 a) Topographic map of the Urayasu city and b) Topographic map with mapped liquefaction polygons digitized from Toida and Yamazaki (2012). Site 1 is a parking lot in the Tokyo Disneyland. Site 2 is an open field near Akemi Elementary School.

## **4.3 Methods**

In order to map liquefaction surface effects, we use spectral variables representing the surface change between the pre- and post-earthquake images and a supervised classification model to map the liquefaction occurrences and nonoccurrences. The approach presented here includes several steps: image preprocessing, spectral variable selection, change detection, classification model development and accuracy assessment, and finally masking the areas where ground surface is not visible from the satellite. These steps are described in the following subsections.

### **4.3.1 Image Preprocessing**

In a satellite image, the intensity of the electromagnetic radiation for each pixel is represented as a digital number. To improve the interpretability of the data and compare data over multiple time periods, we first perform radiometric calibration to convert digital number values to spectral radiance. Most change detection methods (e.g., image differencing, change vector analysis) are sensitive to the spectral differences between images due to variation of atmospheric and illumination conditions. We therefore perform atmospheric correction to remove the effects of the atmosphere and to obtain surface reflectance values. We use the Fast Line-of-Sight Atmospheric Analysis of Spectral Hypercubes (FLAASH; Adler-Golden et al 1998, Anderson et al 2002) module implemented in ENVI, which uses the atmospheric conditions and aerosol properties at the time the image was acquired to estimate and remove the effects of scattering and absorption in the atmosphere. After the atmospheric correction, we still observe consistent differences in reflectance values on invariant objects such as roads that were not affected by the earthquake. To further

match the atmospheric and illumination conditions between two images, we perform a relative radiometric normalization using the Iteratively Re-weighted Multivariate Alteration Detection (IR-MAD) (Canty and Nielsen, 2008).

#### **4.3.2 Spectral Variable Selection**

We investigate candidate variables that can be derived from spectral information and used to identify liquefaction surface effects. Liquefaction is often associated with change in surface moisture and/or ejected sand; therefore, we have focused on variables which are sensitive to the changes in surface moisture or soil characteristic. The spectral variables considered in this study are summarized in Table 2, and include spectral bands, spectral index, and components from spectral transformation.

We consider the change in red (630–690 nm) and near infrared band (NIR; 770 – 895nm) of the electromagnetic spectrum. The red band contains information related to soil characteristics (Bishop and McBratney 2001). The reflectance in the near infrared band is inversely related to the surface moisture because water absorbs the energy in this band (Knipling, 1970). For a spectral index, we consider the normalized difference water index (NDWI) defined in Wolf (2010), which is a spectral ratio of the coastal band (400–450 nm) and longer near infrared band (860–1040 nm). The NDWI contrasts the coastal band with the longer infrared bands to determine the amount of moisture being held by the vegetation or soil. The longer infrared bands are the most sensitive to soil and plant moisture, therefore, the contrast of the coastal band with the longer infrared bands highlights moisture levels within a scene (Crist and Cicone, 1984).

Additionally, we consider components from a spectral transformation. The eight spectral bands from WV-2 are often highly correlated due the wide frequency range of

the ground and reflective materials. Linear combinations of the spectral bands can reduce the correlation yet still be able to describe the majority of the variability in the eight bands. The Tasseled Cap Transformation (Kauth and Thomas, 1976), which was first developed for Landsat TM data and then adapted to WV-2 data (Yarbrough et al 2014), provides such linear combinations and links them with known physical characteristics: soil brightness, vegetation greenness, and soil/vegetation wetness. Brightness is correlated to difference in soil reflectance (and therefore may identify soil ejecta). Greenness contains mainly vegetation-specific information, whereas wetness is linked to surface moisture content (Nackaerts et al 2015). A previous study by Oommen et al. (2013) has used the wetness axes of the tasseled cap transformation to identify areas with increased moisture as a result of liquefaction. We use all three components from the Tasseled Cap Transformation.

### **4.3.3 Change Detection**

For change detection methods, we consider both univariate image differencing (UID) and change vector analysis (CVA; Malia, 1980). In UID analysis, the change is calculated as the difference of a variable between the pre-earthquake and post-earthquake images. We calculate the change values between the pre- and post-earthquake images for the six spectral variables in Table 2. Additionally, we consider CVA because a previous study by Nackaerts et al. (2012) applied CVA in detecting landcover change and found CVA provides better accuracy than UID. The CVA approach defines a change vector between two points in an n-dimensional (n number of spectral variables) feature space, representing two observations of the same pixel over two different times as shown in Figure 2. The change vector's length represents the magnitude of the change event in the spectral feature space, while its direction corresponds to the type of change. When applying CVA, the spectral variables should not be correlated with each other. As discussed above, the individual spectral bands,

such as red and near infrared bands, are correlated, while the three components from the tasseled cap transformation are not correlated yet contain the majority information in eight spectral bands. Therefore, we apply CVA to the three output components (brightness, greenness, and wetness) from the tasseled cap transformation. By using CVA to define a change vector in terms of brightness, greenness, and wetness, we can evaluate the change magnitude across the three spectral indicators as a single metric. We calculate the change angle between each pair of tasseled cap transform components, so three components result in three change angles.

Table 2 Candidate spectral variables. The physical characteristics including soil characteristic and surface moisture that each variable is sensitive to are indicated by black circles.

Variable Description	Soil characteristic	Surface moisture
Red	•	
Near infrared (NIR)		•
Brightness	•	
Greenness		•
Wetness		•
Normalized difference water index (NDWI)		•

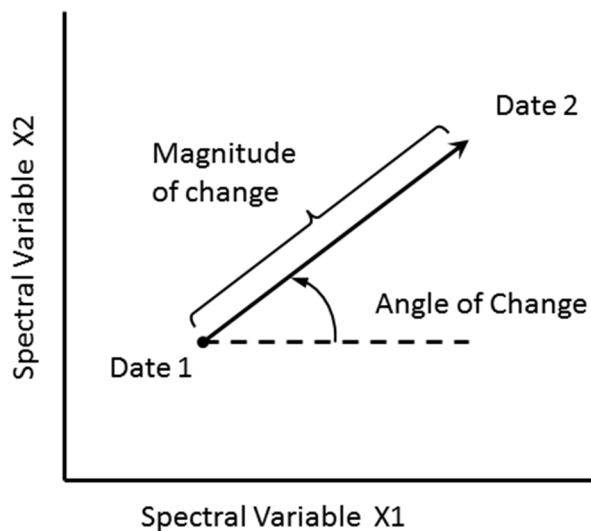


Figure 2 Illustration of a change vector (reproduced from Figure 1 in Malia, 1980).

#### 4.3.4 Classification

We will evaluate two separate pixel-based classification algorithms to classify liquefaction and nonliquefaction: maximum likelihood and decision tree. These are discussed in the following subsections.

##### *Maximum Likelihood Classification*

The maximum likelihood classification (MLC) is a conventional parametric statistical classifier and has been widely applied for land cover mapping from remotely sensed imagery. MLC assumes that the distribution of the spectral data within a given class follows a multivariate Gaussian distribution, with a log likelihood function (or discriminant function) defined as (Richards, 1999)

$$g_i(x) = \ln p(\omega_i) - \frac{1}{2} \ln |\Sigma_i| - \frac{1}{2}(x - m_i)^T \Sigma_i^{-1}(x - m_i)$$

Where:

$i$  = class

$x$  = n-dimensional data (where n is the number of bands)

$p(\omega_i)$  = probability that class  $\omega_i$  occurs in the image and is assumed the same for all classes

$|\Sigma_i|$  = determinant of the covariance matrix of the data in class  $\omega_i$

$\Sigma_i^{-1}$  = its inverse matrix

$m_i$  = mean vector

Each pixel is assigned to the class that has the highest likelihood. The probability density functions are used to classify a pixel by computing the probability of the pixel belonging to each class. The parameters in a MLC model are the mean vector and variance-covariance matrix, which can be estimated from training samples.



### *Decision tree*

A decision tree classifier is a powerful alternative to the conventional MLC classifier. The decision tree classifier is a non-parametric classifier that makes no statistical assumptions regarding the distribution of data. A decision tree consists of a root node, a number of intermediate nodes and finally a set of end nodes, representing different classes. Each path from the root node to a end node represents a set of rules. The decision rules can be determined based on expert knowledge or automatically selected via data mining algorithms. We use the Classification and Regression Tree (CART) algorithm (Breiman et al., 1984). At each node, the CART algorithm selects an attribute and a decision threshold that maximize the distinction among the classes and minimize the diversity within each class, and removes unnecessary nodes through the pruning procedure, producing the shortest tree possible (Witten et al., 2000). Due to its non-parametric nature, decision trees are more flexible when the data are not normally distributed. Another advantage of the decision tree classification is that it can generate understandable rules, and therefore each resulting branch can be easily visualized and interpreted. This can lead to subcategories of liquefaction surface effects in the classification based on subtle differences in spectral characteristics: wet surface effect versus dry surface effect.

#### **4.3.5 Model Development and Accuracy Assessment**

When developing a classification model (decision tree or maximum likelihood classification), we use 10-fold cross validation to select candidate subsets of change indicators using the ten-fold cross validation technique. Ten-fold cross validation is an iterative process. The complete dataset is first split into ten subsets of equal size. In each iteration, one subset is withheld and decision tree or a maximum likelihood classifier is fit to the other nine subsets using the chosen

change indicators. The performance measures are calculated on the held-out subset. This is repeated ten times so that each subset is held out for testing exactly once. The testing data set is always independent from the classification training data set in order to avoid any possible biases. This technique is effective in comparing the performance of different combinations of change vectors while avoiding overfitting to a particular dataset.

To assess classification accuracy and compare between decision tree and maximum likelihood, we use all pixels in the validation dataset (4000 point where 2000 are labeled as liquefaction and 2000 are labeled as nonliquefaction). Confusion matrices were calculated by comparing the model prediction with the validated liquefaction or nonliquefaction produced by visual interpretation from aerial photos (Toida and Yamazaki, 2012). The confusion matrix can be summarized by the producer's accuracy, the user's accuracy, and the overall accuracy. The producer's accuracy is the number of pixels correctly classified in a particular category as a percentage of the total number of pixels actually belonging to that category in the validation dataset. The user's accuracy is calculated as the number of correctly classified pixels to the total number of pixels classified as a particular class. The overall accuracy is not the best measure when class imbalance exists (i.e. the percentage of liquefaction is different from nonliquefaction), as the optimal model can result from classifying all locations by the majority class.

#### **4.3.6 Masking**

In order to apply the classification models across the entire image, we will need to develop a mask which eliminates areas where ground surface is not visible from the

satellite and identifies the regions that can be classified with the proposed method and the data. These areas include building rooftops, trees, shadowed area, and water bodies. We first use the OpenStreetMap (OSM; Weber and Haklay 2008) to mask the building rooftops, trees and water bodies. Because shadows have contrasting spectral characteristics, we identify the shadowed areas using a spectral index, shadow detection index (Shahi et al 2014), which is a function of blue, near infrared 1 and near infrared 2 bands.

## **4.4 Results and Discussion**

### **4.4.1 Liquefaction characteristics**

In the True color composites of the WV-2 image, we mainly observe two different liquefaction surface effects: dry sand boils on pavement and wet sand on soil. To illustrate the observed liquefaction characteristics, we use two example sites. Site 1 is a parking lot in the Tokyo Disneyland district. Figure 3a-c shows the pre- and post-earthquake WV-2 images and the validation points for the Tokyo Disneyland parking lot. Site 2 is an agricultural field next to the Akemi elementary school, and was not vegetated between the periods when the WV-2 images were taken. Figure 4a-c shows the pre- and post-earthquake WV-2 images and the validation points for the Akemi elementary school field. At site 1, liquefaction occurred on the paved ground, where we observe white surface from the post-earthquake image (Figure 3b) indicating dry sand boils. At site 2, liquefaction occurred on soil, where we observe dark brown surface, indicating wet ejected soil or pooled water. We include validation points on both pavement and bare soil to ensure that the classification was effective on pavement and soil.



Figure 3 True color composite of the WV-2 image a) before the 2011 Tohoku earthquake, b) after the 2011 Tohoku earthquake, and c) overlain with validation data for a parking lot (lat 139.877, lon 35.629) in the Tokyo Disneyland. Liquefaction is indicated by the exposed dry sand that appears in yellow tones in the post-earthquake image.



Figure 4 True color composite of the WV-2 image a) before the 2011 Tohoku earthquake, b) after the 2011 Tohoku earthquake, and c) overlain with validation data for an agricultural field (lat 139.917, lon 35.642). Liquefaction is indicated by the wet soil that appears in dark brown in the post-earthquake image.

#### 4.4.2 Change detection analysis

We first calculate the change of the variables in Table 2 between the pre- and post-earthquake images for the entire Urayasu region. The maps of the change in six variables for site 1 are shown in Figure 5 a-f. Similar maps for site 2 are shown in Figure 6 a-f. For comparison, we also show the validated liquefaction points in red from Toida and Yamazaki (2012). As discussed above, liquefaction on the ground

surface is evidenced by dry ejected sand on pavement and wet ejected sand, or pooled water on soil. At site 1, the dry ejected sand shows up as high brightness (red color in Figure 5a) and low wetness (red color in Figure 5f). At site 2, the wet ejected sand shows up as low brightness (green color in Figure 6a) and high wetness (blue color in Figure 6f).

We then apply change vector analysis, and calculate the magnitude of the change vector using all three components from the tasseled cap transformation. The distributions of the magnitude of the change vector for liquefied points and nonliquefied points are shown as boxplots in Figure 7. Although the distributions of the change magnitude overlap, liquefied points overall have higher values of the change magnitude than nonliquefied points showing that the magnitude of the change vector can be used as a predictor. The median of the change magnitude for liquefied points is 1972, whereas the median of the change magnitude for nonliquefied points is 1233. The median of the liquefied change magnitude distribution is coincident with the lower quartile of the nonliquefied change magnitude distribution.

In addition to the variables from the tasseled cap transformation, we test the change in the red and near infrared spectral bands, as well as the NDWI index. The distributions for each of these change variables as well as the wetness and brightness change from the tasseled cap transformation parsed by liquefied and nonliquefied labels are also shown in Figure 7. Similar to the distribution of the change magnitude,

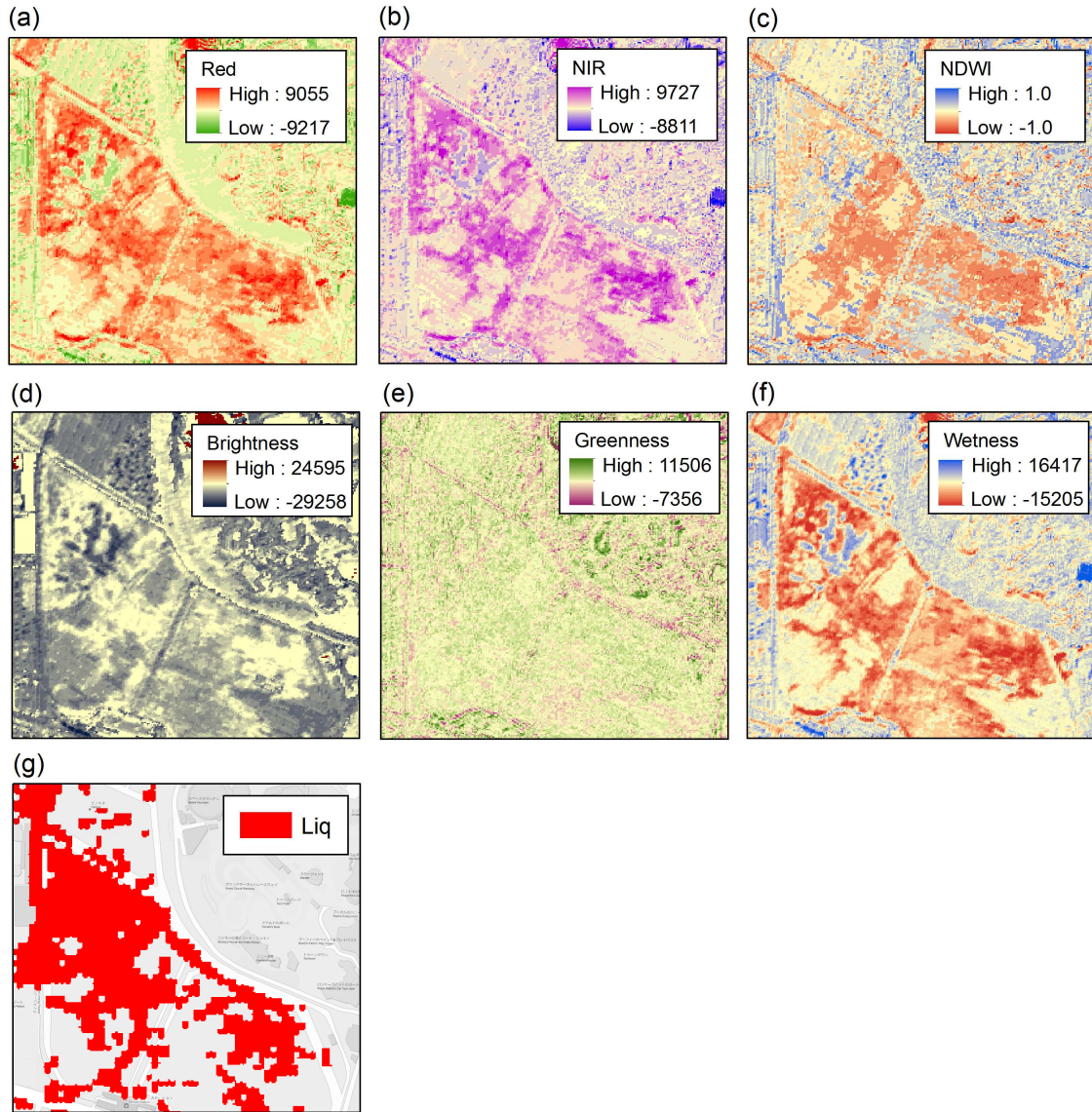


Figure 5 Maps of a) red, b) NIR, c) NDWI, c) brightness, d) greenness, f) wetness and g) mapped liquefaction from Toida and Yamazaki (2012) for the Disney Land parking lot site (Site 1). The high brightness areas and low wetness areas coincide with dry ejected sand on pavement. High means that the spectral variable value in the post-earthquake image is higher than that in the pre-earthquake image. Liquefaction at this site appears correlate to lower NDWI value and lower wetness value, which means low moisture content.



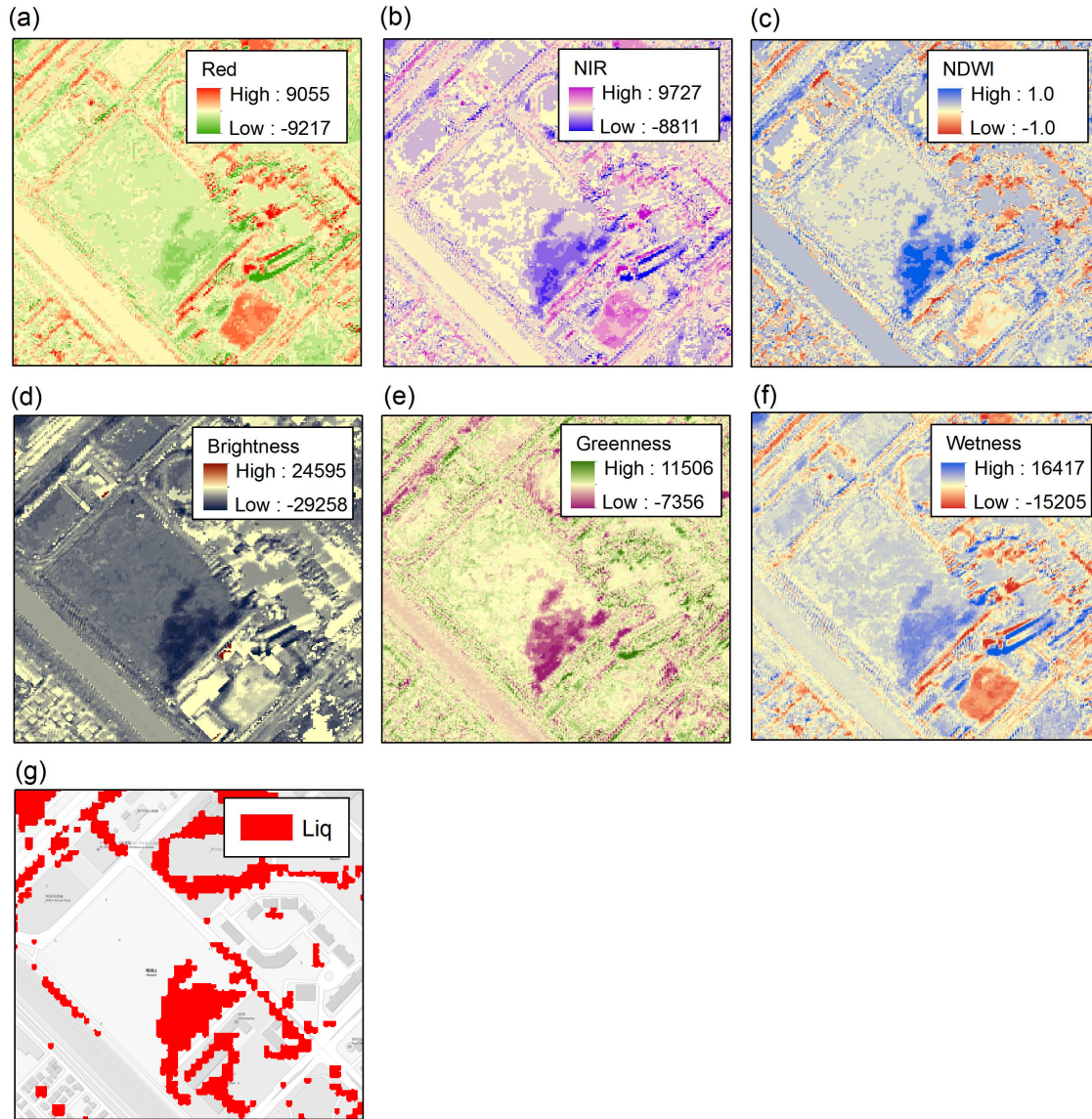


Figure 6 Maps of a) red, b) NIR, c) NDWI, c) brightness, d) greenness, f) wetness and g) mapped liquefaction from Toida and Yamazaki (2012) for the agricultural field site (Site 2) . The low brightness and high wetness spots on the parking lot are coincident with wet ejected sand. High means that the spectral variable value in the post-earthquake image is higher than that in the pre-earthquake image. Liquefaction at this site appears correlate to higher NDWI value and higher wetness value, which means high moisture content.

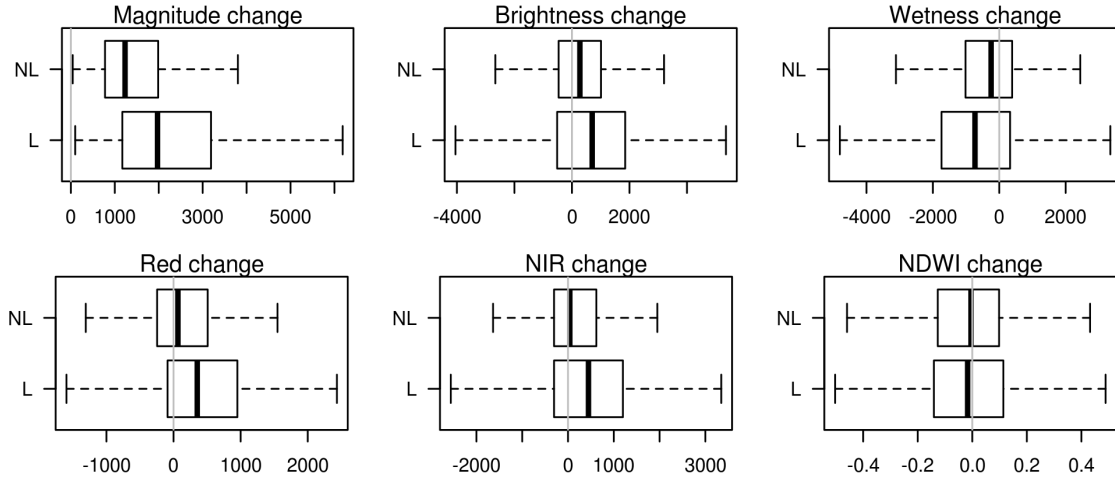


Figure 7 Box and whisker plot of the change magnitude for liquefaction and nonliquefaction points for the entire dataset. In a box and whisker plot, the ends of the box are the upper and lower quartiles, and vertical black line inside the box marks the median. The whiskers are the two lines outside the box that extend to the highest and lowest observations. The vertical grey line indicates no change between the pre- and post-earthquake images.

#### 4.4.3 Maximum likelihood classification

Using the training data, we develop maximum likelihood classifiers with different subsets of change variables and compare their average accuracy across ten-fold cross validation. The maximum likelihood classifier with the highest accuracy includes the change of wetness, brightness, red band, NIR band, and NDWI. The accuracy assessment for the maximum likelihood classifier is summarized in Table 4. The overall accuracy and producer's accuracy of the model is 0.63 and 0.54 respectively.



Table 4 Accuracy assessment confusion matrix for the maximum likelihood classification

		Reference data			User's Accuracy
		Liq	Nonliq	Total	
Prediction	Liq	1089	561	1650	0.66
	Nonliq	911	1439	2350	0.61
	Total	2000	2000		Overall accuracy=0.63
	Producer's Accuracy	0.54	0.72		

#### 4.4.4 Decision Tree

Ten-fold cross validation is also used for training the decision tree classifiers. We input change values for six spectral variables in Table 2, and the final tree is selected by maximizing the accuracy. The change variables selected in the final tree are the change of magnitude, wetness, and NDWI as shown in Figure 8. The decision thresholds for each variable were automatically selected by the CART algorithm (Breiman et al 1984) that maximizes the impurity between two classes at each node. The decision tree is pruned so that optimal complexity can be achieved. The accuracy assessment is shown in Table 5 and results in an overall accuracy of 0.64 and a producer's accuracy of 0.70.

The decision tree method has the benefit that the thresholds are identified and the statistics of the branches are visible to the user. From the decision tree, the change magnitude is the primary classifier where large change in the magnitude ( $>2363$ ) leads to a liquefaction label. Above a lower change magnitude threshold ( $>1101$ ), the change in wetness identifies liquefied locations where there is low wetness (dry ejected sand) and the NDWI identifies liquefied locations where there is high wetness (wet ejected sand). As a result, the decision tree can be used directly to map subclasses of liquefaction based on the branch.

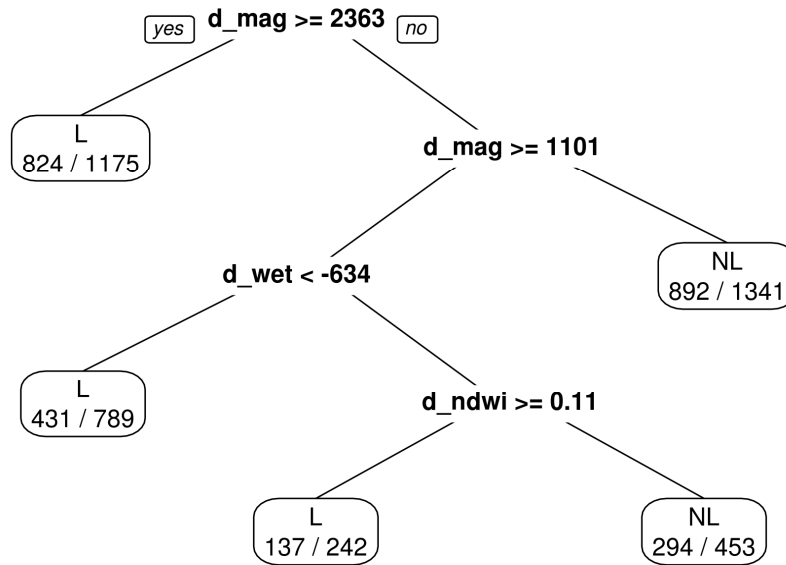


Figure 8 Decision tree to classify liquefaction and nonliquefaction

Table 5 Accuracy assessment confusion matrix for the decision tree

		Reference data			User's Accuracy
		Liq	Nonliq	Total	
Prediction	Liq	1392	814	2206	0.63
	Nonliq	608	1186	1794	0.66
	Total	2000	2000	4000	Overall accuracy = 0.64
Producer's Accuracy		0.70	0.59		

#### 4.4.5 Comparison of classifiers

The overall accuracy of the decision tree method is higher than the maximum likelihood method. The user's accuracy represents how many of the predicted liquefied points are correctly labeled. The user's accuracy of the maximum likelihood method is higher than the decision tree (66% vs. 63%). The producer's accuracy represents how many of the training points are correctly labeled. The producer's

accuracy of the decision tree method is higher than the maximum likelihood method (70% vs. 54%). For the purposes of liquefaction mapping, producer's accuracy is very important, because the producer's accuracy tells us how sites that actually liquefied are classified: 70% as liquefied and 30% as nonliquefied for the decision tree method. The decision tree method has high producer's accuracy for the liquefied points whereas the maximum likelihood method has high producer's accuracy for nonliquefied sites. This is a common tradeoff for classifiers between maximizing true positives (site is correctly labeled as liquefied) or minimizing false positives (site that is falsely predicted as nonliquefied). In addition to comparing accuracy assessment, the other difference is in the model form. The decision tree has a far simpler model form that can be visualized with the decision tree and implemented easily with the relevant thresholds. The decision tree also has the benefit of potentially identifying subclasses through the different tree branches (e.g. dry ejected soil, vs. wet ejected soil). Because we prefer a model with high producer's accuracy and we like the interpretation of the branches of the decision tree as subclasses, we choose the decision tree classifier as our preferred classifier in this study.

#### **4.4.6 Liquefaction Maps**

To visually evaluate the classifier across the Urayasu region, we produce a classification map using the decision tree method as shown in Figure 9. A mask is applied to the region (shown as white) and the decision tree classifier is applied to the remaining unmasked pixels. Prior to mapping the results, a majority filter is applied to remove salt and pepper effect (isolated labels) and to spatially smooth the results. The resulting liquefaction class is mapped as red.

Figure 10 shows additional maps which identifies the subclasses from the

branches of the decision tree (red=liquefaction branch separated by  $\text{change\_magnitude} \geq 2363$ ; yellow=liquefaction branch separated by  $\text{change\_wetness} < -634$  and  $\text{change\_magnitude} < 2363$  and

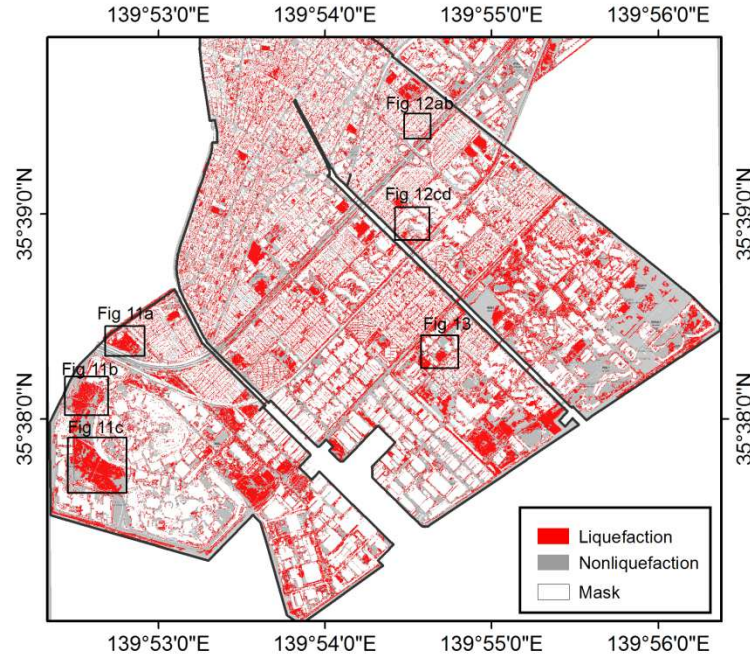


Figure 9. Maps of surface effects predicted using the proposed method in Urayasu City showing examples from three land cover types: road, parking lot, and bare soil.

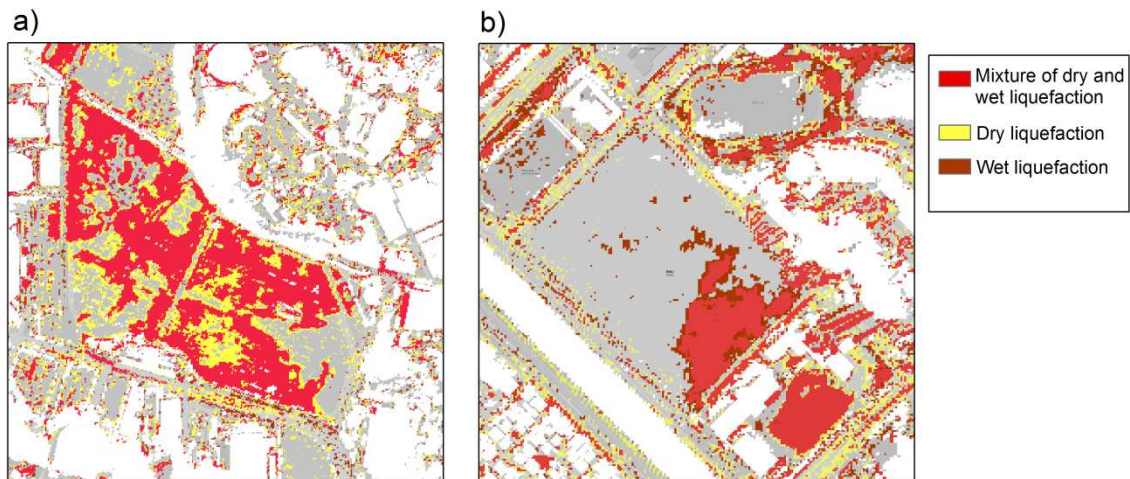


Figure 10. Maps of subclasses from the branches (red=liquefaction branch separated by  $\text{change\_magnitude} \geq 2363$ ; yellow=liquefaction branch separated by  $\text{change\_wetness} < -634$  and  $\text{change\_magnitude} < 2363$  and  $\text{change\_magnitude} \geq 1101$ ; brown=liquefaction branch separated by  $\text{change\_NDWI} \geq 0.11$  and  $\text{change\_wetness} \geq -634$  and  $\text{change\_magnitude} < 2363$  and  $\text{change\_magnitude} \geq 1101$ ) of the decision tree for a) site 1 and b) site 2.

#### 4.4.7 Discussion

The proposed change detection procedure is effective in identifying spectral differences between pre-event and post-event images that are sensitive to moisture content and surface material change. The model performs well on paved surfaces (road and parking lot) in open areas, which are not affected by buildings. Figure 11 shows three examples, where the spatial pattern of predicted liquefaction agrees well with that from Toida and Yamazaki (2012). Notice that there are differences when comparing the prediction produced by the decision tree and Toida and Yamazaki (2012) data pixel by pixel, which partly explains the relative high error rate in Table 5. The overall pattern of liquefaction extent is well captured.

The application of the model is limited in densely built up areas or areas with tall buildings. Figure 12 ab shows the comparison of the predicted liquefaction with mapped polygon from Toida and Yamazaki (2012) on the post-earthquake WV-2 image and OpenStreetMap for an area with dense buildings. Figure 12 cd shows a similar comparison for an area with tall buildings. For an area with dense building, the application is problematic for two reasons. First, as shown in Figure 12a, narrow roads where liquefaction may occur are difficult to see from the satellite, and the spectral value for a pixel can represent an average of multiple objects such as building and road. Second, because of different viewing geometry between the pre- and post-earthquake images, the shadows from the buildings shift locations between two images. As a result, the changes of shadows are mistakenly predicted as liquefaction. Although we have used a spectral index to mask the shadows, not all shadows have been successfully detected.

The application of the model is also problematic for areas with tall buildings. As shown in Figure 12c, the model mispredicts liquefaction at many locations of building

roofs. We used the building data from the OpenStreetMap to mask the buildings, but the viewing geometry from the satellite impacts how the building roofs appear on the post-earthquake WV-2 image. Specifically, in Figure 12c the building rooftops do not

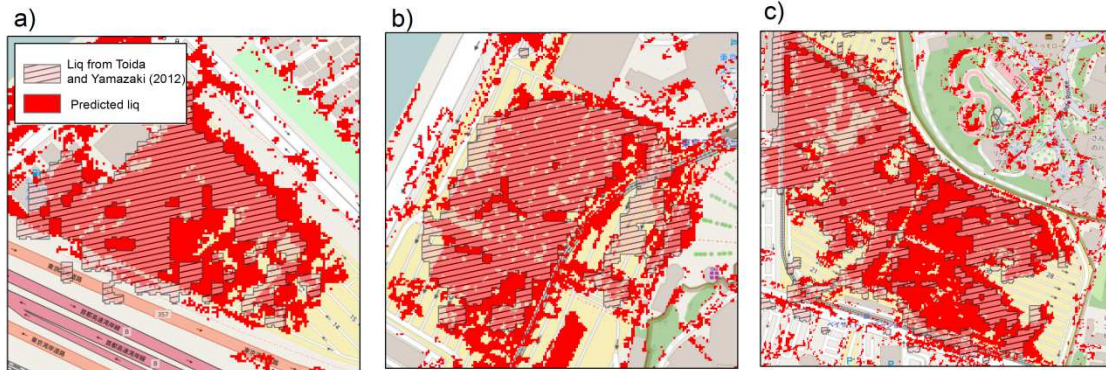


Figure 11 Comparison of predicted liquefaction with digitized liquefaction from Toida and Yamazaki (2012) for three pavement areas.



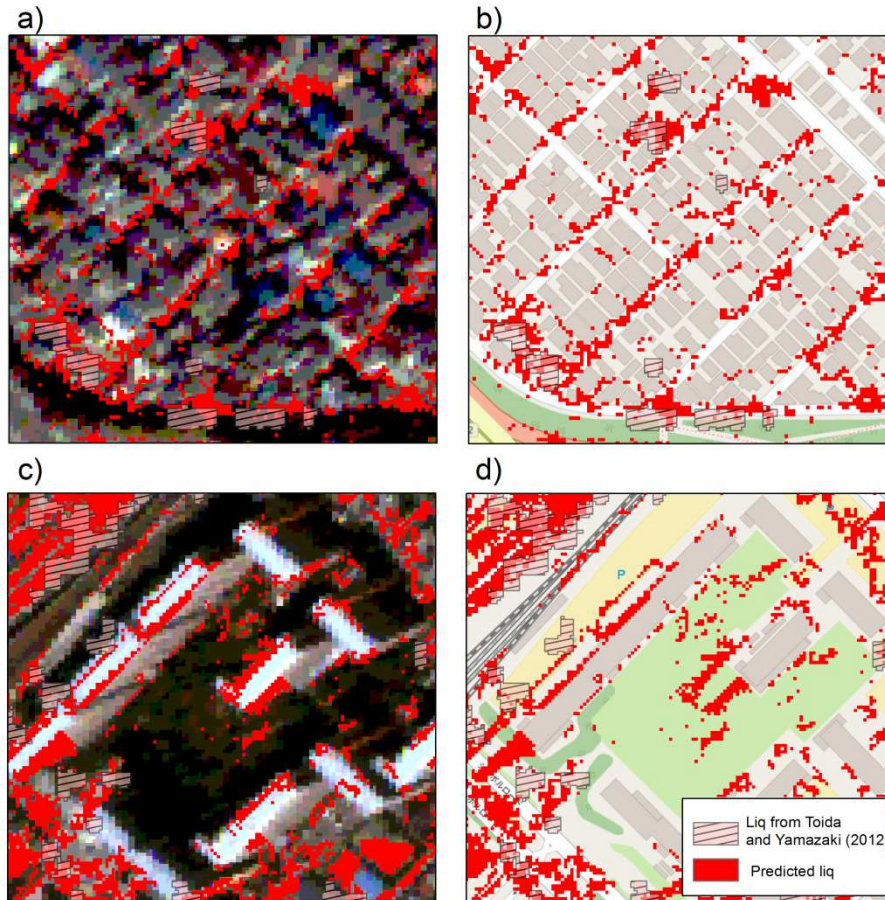


Figure 12 Comparison of predicted liquefaction and mapped liquefaction form Toida and Yamazaki (2012) on a) post-earthquake WV-2 image and b) OpenStreetMap for an area with dense buildings. Same comparison on c) post-earthquake WV-2 image and d) OpenStreetMap for an area with tall buildings.

match the building locations in OpenStreetMap in Figure 12d and the rooftops edges are mapped as liquefaction. This may be addressed if an advanced land cover classification can be performed for each image separately, so the shadows and building can be more accurately masked. A surface elevation model can also be useful to correctly detect and mask the buildings.

Another main source of false prediction is non-liquefaction-related factors that can result in a change in moisture content or surface material. For example, on paved ground, change can be caused by moving vehicles on the road, or relocated vehicles in

a parking lot. On soil, heavy rainfall and irrigation can contribute to the change in moisture content between the two images. Change of vegetation can also cause false prediction. Figure 13 shows an example of this case. As shown in Figure 13c, the model prediction for the field in the center does not agree with the mapped results from Toida and Yamazaki. When the pre- and post-earthquake WV-2 images, the field appears green in the pre-earthquake image, but white in the post-earthquake image, indicating that the vegetation condition has changed between the two periods. The change in surface reflectance due to the change in vegetation results in false prediction.

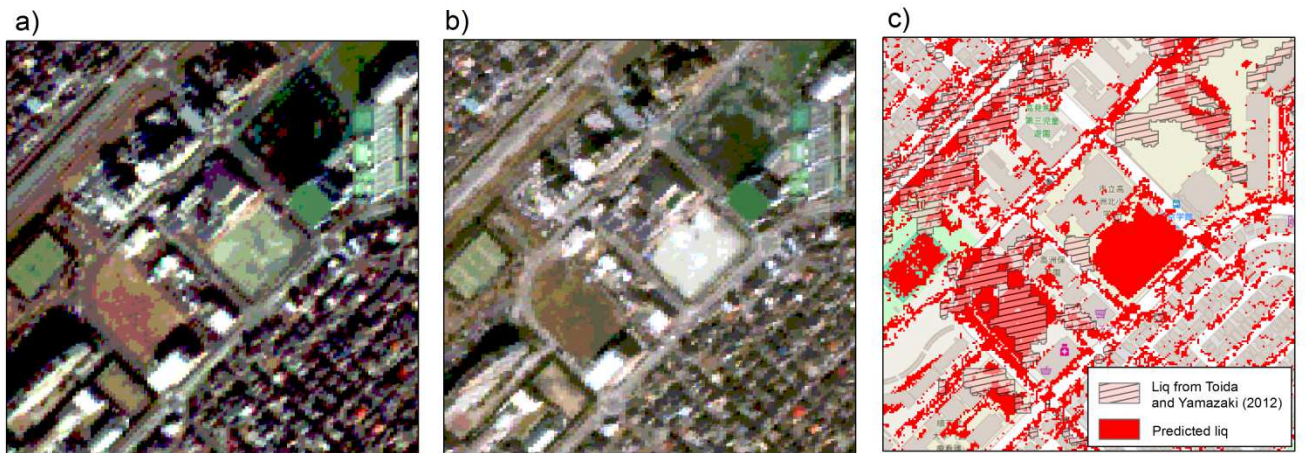


Figure 13 a) pre-earthquake WV-2 image, b) post-earthquake WV-2 image, and c) comparison of predicted liquefaction and mapped liquefaction from Toida and Yamazaki for an area where change of vegetation occurred between the pre- and post-earthquake images.



## 4.5 Conclusion

Developing and validating liquefaction hazard models requires liquefaction data with accurate measures of the aerial extent of individual liquefaction surface manifestations, which is often achieved by the manual interpretation from post-earthquake aerial photos. The high spatial resolution (2 m) of the WorldView-2 images and automated classification techniques based on change in spectral indicators allow detailed mapping of liquefaction surface effects. We use both a maximum likelihood classification and a decision tree classification to map the surface effects of liquefaction caused by the 2011 Tohoku earthquake. The results are evaluated with training data derived from visual inspection of high resolution aerial photography (Toida and Yamazaki, 2012). We study the spectral separability between liquefaction and nonliquefaction using change variables that are sensitive to change in moisture content and surface material such as brightness and wetness from the tasseled cap transformation as well as changes in the Red and NIR spectra bands, and changes in the NDWI index. We observe different spectral signatures for dry ejected sand (high brightness, low wetness) and wet ejected sand (low brightness, high wetness). The decision-tree and Maximum likelihood approach classified liquefaction and nonliquefaction with an overall accuracy of 63% and 64% respectively. The decision tree classification is preferred due to the higher producer's accuracy for liquefaction (70%, fewer false negatives) and the simple implementation and interpretation of the model. The decision tree branches allow for subclass identification, which is useful in interpretation of the map. Classification errors occurred in areas where other factor such as rain and irrigation change the moisture content, or areas that are densely covered by tall buildings. The study demonstrates that change detection techniques such as change vector analysis, in combination with classification on high spatial resolution satellite imagery with multiple spectral bands, can be an effective tool in

mapping liquefaction surface effects; however, urban areas continue to be challenging. The change in magnitude of the change vector including brightness, greenness, and wetness is the most effective classifier of the individual change variables; however, change in the wetness, brightness, red, NIR, spectral bands and the NDWI index can contribute to the classification. The proposed classification method is efficient and can be quickly applied over a broad region. The proposed automated classification method can be used in combination with a field survey and visual interpretation of true-color composite images or aerial imagery to ensure broader coverage and higher resolution than possible with most field surveys alone.

## 5 Summary

### 5.1 Research findings

The dissertation addresses liquefaction hazard mapping at a regional scale. The improvements to the liquefaction mapping focus on two aspects including 1) predictive hazard mapping and 2) post-liquefaction cataloging.

Chapter 2 and Chapter 3 address the predictive mapping of liquefaction hazard. In Chapter 2, I present an approach to estimation of earthquake induced liquefaction from globally available geospatial proxies and earthquake-specific parameters. I compile a liquefaction database that includes observations of the presence/absence of liquefaction and geospatial explanatory variables from two earthquakes in Kobe, Japan, and two earthquakes in Christchurch, New Zealand.

I derive two liquefaction models with explanatory variables that include magnitude adjusted peak ground acceleration, shear-wave velocity, compound topographic index, and a newly defined normalized distance parameter (distance to coast divided by the sum of distance to coast and distance to the basin inland edge). I evaluate both models across all four earthquakes as well as the 2010 Haiti earthquake. I conclude that these models provide first-order approximations of the extent of liquefaction, appropriate for use in rapid response, loss estimation, or scenario simulations. Because the presence/absence of liquefaction has been mapped so that the database is unbiased with respect to the areal extent of liquefaction, the probability predicted by the models can be interpreted as the spatial extent of liquefaction.

In Chapter 3, I update the work in Chapter 2 to improve the performance and the generality of the geospatial liquefaction model. The updates include 1) expanding the liquefaction database to 27 earthquake events across 6 countries, 2) addressing

the sampling of nonliquefaction for incomplete liquefaction inventories, 3) testing interaction effects between explanatory variables, and 4) overall improving model performance. I compare 18 proxies for earthquake shaking, soil saturation and soil density. I find PGV performs better than PGA as a shaking parameter. The patterns of saturation proxies show different scales of details. At a regional scale, distance to the water body performs best. I find that considering interaction terms between distance to river and distance to coast improves the accuracy of the model. The model that performs best over the entire dataset includes PGV, Vs30, distance to river, distance to coast, and precipitation. The model that performs best over the noncoastal dataset includes, PGV, Vs30, water table depth, distance to water body, and precipitation. The updated models offer an improved accuracy as compared to the model in Chapter 2. I validate the models and assess the resulting probability in terms of probability thresholds and the spatial extent of liquefaction. I find that the mapped probability of liquefaction can be used as an estimate of spatial extent within classes but should be adjusted due to the 50:50 class balance used. Overall, the footprint and overall degree of liquefaction is successfully recovered for test events to a degree that indicates our models should prove useful for global, near-real-time applications.

Chapter 4 addresses post-liquefaction cataloging. In Chapter 4, I present an approach that uses change detection techniques in combinations with classification on high spatial resolution satellite imagery to map the surface effects of liquefaction caused by the 2011 Tohoku earthquake. For change detection methods, I use both univariate image differencing and change vector analysis. For classification methods, I compare a maximum likelihood classification and a decision tree classification. The results are evaluated with training data derived from visual inspection of high resolution aerial photography

(Toida and Yamazaki, 2012). The decision-tree and Maximum likelihood approach classified liquefaction and nonliquefaction with an overall accuracy of 63% and 64% respectively. The decision tree classification is preferred due to the higher producer's accuracy for liquefaction (70%, fewer false negatives) and the simple implementation and interpretation of the model. The decision tree branches allow for subclass identification, which is useful in interpretation of the map. The proposed approach is efficient and can be quickly applied over a broad region, and therefore can be an effective tool in mapping liquefaction surface effects; however, urban areas continue to be challenging. The proposed approach can be used in combination with a field survey and visual interpretation of true-color composite images or aerial imagery to ensure broader coverage and higher resolution than possible with most field surveys alone.

## **5.2 Recommendations for future research**

The models in Chapter 2 and 3 are ready to be implemented to calculate probability of liquefaction immediately after an earthquake, which can be interpreted as the aerial extent of liquefaction. A loss estimation framework that takes account of the probability predicted by the models is needed to estimate losses from liquefaction-induced effects such as differential settlement and horizontal displacement or monetary losses.

Soil saturation is the factor that is most difficult to characterize using the geospatial proxies that are globally available. I find the global layer of mapped water table depth by Fan et al does not perform better than proxies based on the proximity to water bodies (e.g., distance to river, distance to water bodies) in differentiating between liquefied and nonliquefied areas. Development of more detailed or more accurate maps of water table depth will be useful to improve the

prediction of liquefaction using the geospatial models.

The generalization of the geospatial models to noncoastal regions can be improved through future work by collecting more liquefaction data from noncoastal areas and identifying additional proxies that work for the noncoastal environment.

The liquefaction map detected from satellite images at very high spatial resolution using the method in Chapter 4 is at a much higher resolution than the maps from field reconnaissance or predicted from empirical models. Although detailed information on individual mapped liquefaction features is valuable, the fine resolution can pose a challenge when we want to use the product in combination with field reconnaissance results, or when we want to use the product to validate empirical models. Future research is needed in developing methods for aggregating liquefaction features detected from satellite images and interpreting the catalogues at different spatial scales. Perhaps, the aggregation of liquefaction features can be performed within an area outlined based on building footprints or objects segmented based on spectral characteristics.

## Bibliography

- Adler-Golden, S.; Berk, A.; Bernstein, L.S.; Richtsmeier, S.; Acharya, P.K.; Matthew, M.W.; Anderson, G.P.; Allred, C.L.; Jeong, L.S.; Chetwynd, J.H. FLAASH, a MODTRAN4 atmospheric correction package for hyperspectral data retrievals and simulations. In Proceedings of the 7th Annual JPL Airborne Earth Science Workshop, Pasadena, CA, USA, 12–16 January 1998; Green, R.O., Ed.; 9–14.
- Akaike, H., 1973. Information theory as an extension of the maximum likelihood principle. Second International Symposium on Information Theory. B. N. Petrov, and F. Csaki, (Eds.), Akademiai Kiado, Budapest.
- Allen, J., Ashford, S., Bowman, E., Bradley, B., Cox, B., Cubrinovski, M., Green, R., Hutchinson, T., Kavazanjian, E., Orense, R., Pender, M., Quigley, M., and Wotherspoon, L., 2010. Geotechnical Reconnaissance of the 2010 Darfield (New Zealand) Earthquake, GEER Association Report No. GEER-024, ed. R. A. Green and M. Cubrinovski.
- Allen, J., S., Bradley, B., Bradshaw, A., Bray, J., Cubrinovski, M., DePascale, G., Green, R. A., Orense, R., O'Rourke, T., Pender, M., Rix, G., Wells, D., Wood, C., and Wotherspoon, L., 2011. Geotechnical Reconnaissance of the 2011 Christchurch, New Zealand Earthquake, GEER Association Report No. GEER-027, ed. Green R. A., Cubrinovski M., and Wotherspoon, L.
- Allen, T. I., and Wald D. J., 2009. On the Use of High-Resolution Topographic Data as a Proxy for Seismic Site Conditions ( $V_{s30}$ ), *Bull. Seism. Soc. Am.* **99**, 935–943.
- Allen, T. I., Wald, D. J., Hotovec, A. J., Lin, K., Earle, P. S., and Marano, K. D., 2008. An Atlas of ShakeMaps for selected global earthquakes, U.S. Geol. Surv. Open-File Report 2008-1236, 34 pp.
- Anderson, G.P.; Felde, G.W.; Hoke, M.L.; Ratkowski, A.J.; Cooley, T.W.; Chetwynd, J.H., Jr.; Gardner, J.A.; Adler-Golden, S.M.; Matthew, M.W.; Berk, A.; et al. MODTRAN4-based atmospheric correction algorithm: FLAASH (fast line-of-sight atmospheric analysis of spectral hypercubes). In Algorithms and Technologies for Multispectral, Hyperspectral, and

- Ultraspectral Imagery VIII (Proceedings of SPIE); Shen, S.S., Lewis, P.E., Eds.; Society of Photo Optics: Orlando, FL, USA, 2002; pp. 65–71
- Andrus, R. D., and Stokoe II, K. H. (2000). Liquefaction resistance of soils from shearwave velocity. *J. Geotech. Geoenviron. Eng.*, 126(11), 1015-1025.
- Atkinson, G. M., and Boore, D. M., 2011. Modifications to existing ground-motion prediction equations in light of new data, *Bull. Seismol. Soc. Am.* 101, 1121-1135.
- Beavan, J., Fielding, E., Motagh, M., Samsonov, S., and Donnelly, N., 2011. Fault Location and Slip Distribution of the 22 February 2011 Mw 6.2 Christchurch, New Zealand, Earthquake from Geodetic Data, *Seismol. Res. Lett.* **82**, 789–799.
- Baise, L. G., D. Daley, J. Zhu, E. M. Thompson, and K. Knudsen (2012). Geospatial liquefaction hazard model for Kobe, Japan and Christchurch, New Zealand, *Seismol. Res. Lett.* 83, 458.
- Beven, K. J. and Kirkby, M. J. (1979). A physically based, variable contributing area model of basin hydrology, *Hydrol. Sci. Bull.* 24, 43–69.
- Bhattacharya, S., Hyodo, M., Goda, K., Tazoh, T., and Taylor, C. A. (2011). Liquefaction of soil in the Tokyo Bay area from the 2011 Tohoku (Japan) earthquake. *Soil Dynamics and Earthquake Engineering*, 31(11), 1618-1628.
- Bishop, T. F. A., & McBratney, A. B. (2001). A comparison of prediction methods for the creation of field-extent soil property maps. *Geoderma*, 103(1), 149-160.
- Boore, D. M., and Atkinson, G. M., 2008. Ground-motion prediction equations for the average horizontal component of PGA, PGV, and 5%-damped PSA at spectral periods between 0.01 s and 10.0 s, *Earthquake Spectra* 24, 99–138.
- Boulanger, R. and I. Idriss (2015). CPT-based liquefaction triggering procedure, *J. Geotech. Geoenviron. Eng.*, 10.1061/(ASCE)GT.1943-5606.0001388, 04015065.
- Brankman, C. M., and L. G. Baise (2008). Liquefaction susceptibility mapping in Boston, Massachusetts, *Engineering and Environmental Geoscience XIV*, 1–16. Bradley, B. A., 2010. *NZ-specific pseudo-spectral acceleration ground motion prediction equations based on foreign models*, University of Canterbury, Department of Civil Engineering, 324 pp.



- Bray, J. D., R. Sancio, A. M. Kammerer, S. Merry, A. Rodriguez-Marek, B. Khazai, S. Chang, A. Bastani, B. Collins, E. Hausler, D. Dreger, W. J. Perkins, and M. Nykamp (2001). Some observations of the geotechnical aspects of the February 28, 2001, Nisqually Earthquake in Olympia, South Seattle, and Tacoma, Washington. *Pacific EQ. Engrg. Res. Cen.*:<http://peer.berkeley.edu/nisqually/geotech/index.html>, March 8, 2001. Brankman, C. M., and Baise, L. G., 2008. Liquefaction Susceptibility Mapping in Boston, Massachusetts, *Engineering and Environmental Geoscience XIV*, 1–16.
- Breiman, Leo; Friedman, J. H.; Olshen, R. A.; Stone, C. J. (1984). Classification and regression trees. Monterey, CA: Wadsworth & Brooks/Cole Advanced Books & Software. ISBN 978-0-412-04841-8.
- Brier, G. W. (1950). Verification of forecasts expressed in terms of probability. *Monthly weather review* 78, 1-3.
- Brown, L. J., Beetham, R. D., Paterson, B. R., and Weeber, J. H., 1995. Geology of Christchurch, New Zealand, *Environmental and Engineering Geoscience* 1, 427–488.
- Brown, L. J., and Weeber, J. H., 1992. Geology of the Christchurch Urban Area, Lower Hutt, New Zealand, Institute of Geological and Nuclear Sciences.
- Byrne, G.F., Crapper P.F., and Mayo K.K, 1980, Monitoring land-cover change by principal component analysis of multitemporal Landsat data, *Remote Sensing of the Environment*, 10, 175-184.
- Canty, M. J. (2014). Image analysis, classification and change detection in remote sensing: with algorithms for ENVI/IDL and Python. Crc Press.
- Canty and Nielsen, 2008 M.J. Canty, A.A. Nielsen Automatic radiometric normalization of multitemporal satellite imagery with the iteratively re-weighted MAD transformation. *Remote Sensing of Environment*, 112 (3), 1025–1036
- Cao, Z., L. Hou, H. Xu, and X. Yuan (2010). Distribution and characteristics of gravelly soil liquefaction in the Wenchuan Ms 8.0 earthquake. *Earthquake Engineering and Engineering Vibration*, 9, 167-175.
- Cetin, O., 2000. Ph.D. Dissertation, University of California, Berkeley.

- Cetin, K. O., Seed, R. B., Der Kiureghian, A., Tokimatsu, K., Harder Jr, L. F., Kayen, R. E., and Moss, R. E. (2004). Standard penetration test-based probabilistic and deterministic assessment of seismic soil liquefaction potential, *J. Geotech. Geoenviron. Eng.*, 130, 1314-1340.
- Chang, D. H.; Islam, S., 2000. Estimation of soil physical properties using remote sensing and artificial neural network, *Remote Sensing of Environment*, 74, 534–544.
- Chen, R. and Harmsen, S., 2012. Probabilistic Ground Motion Calculations and Implementation of PGA Scaling by Magnitude for Assessing Liquefaction Hazard, Technical Document 2012-1, Seismic Hazard Zonation Program.
- Chleborad, A. F., R. L. Schuster (1998). Ground failure associated with the Puget Sound region earthquakes of April 13, 1949, and April 29, 1965, in Assessing earthquake hazards and reducing risks in the Pacific Northwest: U.S. Geological Survey Professional Paper 1560.
- Chleborad, A. F., Schuster, R. L. (1990). Ground failure associated with the Puget Sound region earthquakes of April 13, 1949, and April 29, 1965, U.S. Geological Survey Open File Report 90-687.
- Chu, D. B., J. P. Stewart, S. Lee, J. S. Tsai, P. S. Lin, B. L. Chu, R. B. Seed, S. C. Hsu, M. S. Yu, and M. C. Wang (2004). Documentation of soil conditions at liquefaction and non-liquefaction sites from 1999 Chi–Chi (Taiwan) earthquake, *Soil Dynam. Earthquake Eng.*, 24, 647-657.
- Coppin, P., Jonckheere, I., Nackaerts, K., Muys, B. and Lambin, E. (2004). Review Article: Digital change detection methods in ecosystem monitoring: a review, *International Journal of Remote Sensing*, 25 (9), 1565-1596.
- Coppin, P.R. and BAUER, M.E., 1994, Processing of multitemporal Landsat TM imagery to optimize extraction of forest cover change features. *IEEE Transactions on Geoscience and Remote Sensing*, 918–927.
- Cubrinovski, M., Bray, J. D., Taylor, M., Giorgini, S., Bradley, B., Wotherspoon, L., and Zupan, J., 2011. Soil liquefaction effects in the central business district during the February 2011 Christchurch earthquake, *Seismol. Res. Lett.* 82, 893–904.

- Elliott, J. R., Nissen, E. K., England, P. C., Jackson, J. A., Lamb, S., Li, Z., Oehlers, M., and Parsons, B., 2012. Slip in the 2010-2011 Canterbury earthquakes, New Zealand, *J. Geophys. Res.*, 117, B03401.
- Environment Canterbury Regional Council, 2012. <http://ecan.govt.nz/services/online-services/monitoring/groundwater-levels/Pages/central-canterbury-plains.aspx>, last accessed December 2012.
- Estabrooks, A., T. J., and N. Japkowicz (2004). A multiple resampling method for learning from imbalanced data sets, *Computational intelligence*, 20, 18-36.
- Fan, Y., H. Li, G. Miguez-Macho (2013). Global patterns of groundwater table depth, *Science* 339, 940-943
- Faris, A., 2004. Ph.D. Dissertation, University of California, Berkeley.
- Farr, T. G., and Kobrick M., 2000. Shuttle Radar Topography Mission produces a wealth of data, *Eos Trans. AGU*, 81, 583–585.
- Green, R.A., Olson, S.M., Cox, B.R., Rix, G.J., Rathje, E., Bachhuber, J., French, J., Lasley, S., and Martin, N., 2011a. Geotechnical aspects of failures at Port-au-Prince seaport during the 12 January 2010 Haiti Earthquake, *Earthquake Spectra*, 27, S43–S65.
- Green, R. A., Wood, C., Cox, B., Cubrinovski, M., Wotherspoon, L., Bradley, B., Algie, T., Allen, J., Bradshaw, A., and Rix, G., 2011b. Use of DCP and SASW tests to evaluate liquefaction potential: Predictions vs. observations during the recent New Zealand earthquakes, *Seismol. Res. Lett.*, 82, 927–938.
- Hamada M., Isoyama, R., and Wakamatsu, K., 1995. The 1995 Hyogoken-Nanbu (Kobe) Earthquake: Liquefaction, Ground Displacement and Soil Condition in the Hanshin Area, Assoc. for Development of Earthquake Prediction, Tokyo, 194 p.
- Hanson, C., and Araham, P., 2009. Depth and spatial variation in groundwater chemistry – Central Canterbury Plains, Report No. R09/39.
- Holzer, T. L., Bennett, M. J., Noce, T. E., Padovani, A. C., and Tinsley, J. C., III, 2006. Liquefaction hazard mapping with LPI in the greater Oakland, California, area, *Earthquake Spectra*, 22, 693–708.

- Holzer, T. L., Noce, T. E., and Bennett, M. J., 2009. Scenario liquefaction hazard maps of Santa Clara Valley, Northern California, *Bull. Seism. Soc. Am.*, 99, 367–381.
- Huzita, K., and Maeda, Y., 1985. Geology of the Osaka-Seinambu District, Scale 1:50,000, Geological Survey of Japan.
- Hamada, M., R. Isoyama, and K. Wakamatsu (1995). The 1995 Hyogoken-Nanbu (Kobe) earthquake: Liquefaction, ground displacement and soil condition in the Hanshin Area, Assoc. for Development of Earthquake Prediction, Tokyo, 194 p.
- Hamada, M. and Wakamatsu, K., 1995. Liquefaction, ground deformation and their caused damage to structures. The 1995 Hyogoken-Nanbu Earthquake—Investigation into Damage To Civil Engineering Structures, 45-92.
- Hastie, T., R. Tibshirani, and J. Friedman (2001). The elements of statistical learning: Data mining, inference and prediction. Springer Series in Statistics.
- Holzer, T. L., M. J. Bennett, T. E. Noce, A. C. Padovani, and J. C. Tinsley III (2006). Liquefaction hazard mapping with LPI in the greater Oakland, California, area, *Earthquake Spectra*, 22, 693–708.
- Holzer, T. L., T. E. Noce, M. J. Bennett, J. C. Tinsley, and L. I. Rosenberg (2005). Liquefaction at Oceano, California, during the 2003 San Simeon earthquake, *Bull. Seism. Soc. Am.*, 95, 2396-2411.
- Holzer, T. L., T. E. Noce, and M. J. Bennett (2009). Scenario liquefaction hazard maps of Santa Clara Valley, Northern California, *Bull. Seism. Soc. Am.*, 99, 367–381.
- Idriss, I. M., and Boulanger, R. W., 2008. Soil liquefaction during earthquakes. Monograph MNO-12, Earthquake Engineering Research Institute, Oakland, CA, 261 pp.
- Ishihara, K., 1996. Soil Behavior in Earthquake Geotechnics, Oxford University Press Inc., New York, NY, 350 pp.
- Ishitsuka, K., Tsuji, T., and Matsuoka, T. (2012). Detection and mapping of soil liquefaction in the 2011 Tohoku earthquake using SAR interferometry. *Earth, planets and space*, 64(12), 1267-1276.

- Jensen, J.R., 1981, Urban change detection mapping using Landsat digital data. *The American Cartographer*, 8, 127–147.
- Jensen, J. R. (2007). *Remote Sensing of the Environment: An Earth Resource Perspective*, 2nd Edition, Upper Saddle River: Prentice-Hall, 592 p.
- Juang, C. H., and Jiang, T. (2000). Assessing probabilistic methods for liquefaction potential evaluation. *Proceedings, GeoDenver Conference - Soil Dynamics and Liquefaction 2000*, American Society of Civil Engineers, Reston, VA, USA, 148-162.
- Kayen, R. E., 2011. Personal communication.
- Kayen, R., R. E. S. Moss, E. M. Thompson, R. B. Seed, K. O. Cetin, A. D. Kiureghian, Y. Tanaka, and K. Tokimatsu (2013). Shear-wave velocity–based probabilistic and deterministic assessment of seismic soil liquefaction potential, *J. Geotech. Geoenviron. Eng.*, 139, 407-419.
- Kleinbaum, D. G., and M. Klein (2010). *Logistic regression: a self-learning text*. Springer Science & Business Media.
- Knipling, E. B. (1970). Physical and physiological basis for the reflectance of visible and near-infrared radiation from vegetation. *Remote Sensing of Environment*, 1(3), 155-159.
- Knudsen, K. and J. Bott (2011). Geologic and geomorphic evaluation of liquefaction case histories for rapid hazard mapping, 2011, *Seismol. Res. Lett.*, 82, 334.
- Kothari R., and Islam S., 1999. Spatial Characterization of Remotely Sensed Soil Moisture Data Using Self Organizing Feature Maps, *IEEE Transactions on Geoscience and Remote Sensing*, 37, 1162–1165.
- Lambert, M., Gaudin, J., and Cohen, R., 1987. *Geologic Map of Haiti, South-East Region: Port-au-Prince*, Centre d’Études et de Réalisations Cartographiques Géographiques (CERCG), National Center for Scientific Research (CNRS), Paris, France.
- Lance D. Yarbrough, Kumar Navulur & Rachana Ravi (2014) Presentation of the Kauth–Thomas transform for WorldView-2 reflectance data, *Remote Sensing Letters*, 5:2, 131-138, DOI: 10.1080/2150704X.2014.885148

- Laurikkala, J. (2001). Improving identification of difficult small classes by balancing class distribution. In Conference on Artificial Intelligence in Medicine in Europe (pp. 63-66). Springer Berlin Heidelberg.
- Lunetta, R.S. (1998). Applications, Project Formulation, and Analytical Approach. Remote Sensing Change Detection: Environmental Monitoring Methods and Applications (R.S. Lunetta and C.D. Elvidge, editors), Ann Arbor Press, Chelsea, MI, 1- 19.
- Magistrale, H., Y. Rong, W. Silva, and E. Thompson (2012). A site response map of the continental U.S., Proceedings Fifteenth World Conference on Earthquake Engineering Lisbon, Portugal.
- Malila, W. A. Change vector analysis: an approach for detecting forest changes with Landsat. 1980.385
- Matsuoka, M., K. Wakamatsu, M. Hashimoto, S. Senna, and S. Midorikawa (2015). Evaluation of liquefaction potential for large areas based on geomorphologic classification, *Earthquake Spectra*, 31, 2375-2395.
- Maurer, B. W., R. A. Green, M. Cubrinovski, and B. A. Bradley (2015). Assessment of CPT-based methods for liquefaction evaluation in a liquefaction potential index framework, *Geotechnique*, 65, 328–336
- Ministry of Land, Infrastructure, Transport and Tourism (MLITT) of Kanto Region Development Bureau and Japanese Geotechnical Society (2011). Investigation of liquefaction phenomena of Kanto region in Great East Japan Earthquake, (in Japanese), <http://www.ktr.mlit.go.jp/bousai/bousai00000061.html>.
- Moehle, J. P., J. Bray, G. Fenves, F. Filippou, S. Mahin, T. McEvilly, M. Riemer, B. Romanowicz, R. Seed, N. Sitar, C. Thewalt (1994). Preliminary report on the seismological and engineering aspects of the January 17, 1994 Northridge Earthquake. UCB/EERC-94-01, Earthquake Engineering Research Center, Berkeley, California, January, 72 p.
- Morgenroth, J., Hughes, M. W., and Cubrinovski, M. (2016). Object-based image analysis for mapping earthquake-induced liquefaction ejecta in Christchurch, New Zealand. *Natural Hazards*, 82(2), 763-775.
- Moss, R., 2003. Ph.D. Dissertation, University of California, Berkeley.

- Moss, R. E., E. M. Thompson, D. S. Kieffer, B. Tiwari, Y. M. Hashash, I. Acharya, B. R. Adhikari, D. Asimaki, K. B. Clahan, B. D. Collins and S. Dahal (2015). Geotechnical effects of the 2015 magnitude 7.8 Gorkha, Nepal, earthquake and aftershocks. *Seismol. Res.Lett.*, 86, 1514-1523.
- Moore, I. D., Grayson, R. B., and Ladson, A. R., 1991. Digital terrain modeling: A review of hydrological, geomorphological and biological applications, *Hydrol. Processes* 5, 3–30.
- Nackaerts K. , K. Vaesen , B. Muys and P. Coppin (2005) Comparative performance of a modified change vector analysis in forest change detection, *International Journal of Remote Sensing*, 26:5, 839-852, DOI: 10.1080/0143116032000160462
- Olson, S., 2001. Ph.D. Dissertation, University of Illinois, Urbana-Champaign.
- Oommen T., Baise L. G., and Vogel R. M., 2011. Sampling bias and class imbalance in maximum likelihood logistic regression, *Mathematical Geosciences*, 43, 99–120.
- Oommen, T., L. G. Baise, and R. M. Vogel (2010). Validation and application of empirical liquefaction models, *J. Geotech. Geoenviron. Eng.*, 136, 1618-1633.
- Oommen, T., L. G. Baise, and R. M. Vogel (2011). Sampling bias and class imbalance in maximum likelihood logistic regression, *Mathematical Geosciences*, 43, 99–120.
- Oommen, T., Baise, L.G., Gens, R., Prakash, A., and Gupta, R.P. (2013). Documenting Earthquake-induced Liquefaction Using Satellite Remote Sensing Image Transformations, *Environmental and Engineering Geoscience*, 19, 303-318.
- Orense, R.P., Kigota, T., Yamada, S., Cubrinovski, Hosono, Y., Okamura, M., and Yasuda, S., 2011. Comparison of Liquefaction Features Observed during the 2010 and 2011 Canterbury Earthquakes, *Seismol. Res. Lett.*, 82, 905-918.
- Palmer S. P., S. L. Magsino, E. L. Bilderback, J. L. Poelstra, D. S. Folger, and R. A. Niggemann (2004). Liquefaction susceptibility and site class maps of Washington State, by county: Washington Division of Geology and Earth Resources Open File Report 2004-20.
- R Development Core Team (2016). R: A language and environment for statistical computing, R Foundation for Statistical Computing, Vienna, Austria, ISBN 3-900051-07-0.

- Ramakrishnan, D., Mohanty, K.K., Nayak, S.R. and Chandran, R.V., 2006. Mapping the liquefaction induced soil moisture changes using remote sensing technique: an attempt to map the earthquake induced liquefaction around Bhuj, Gujarat, India. *Geotechnical & Geological Engineering*, 24(6), 1581-1602.
- Rathje, E., Bachhuber, J., Cox, B., French, J., Green, R., Olson, S., Rix, G., Wells, D., and Suncar, O., 2010. Geotechnical Reconnaissance of the 2010 Haiti Earthquake, GEER Association Report No. GEER-021.
- Rathje, E., Bachhuber, J., Dulberg, R., Cox, B., Kottke, A., Wood, C., Green, R., Olson, S., Wells, D., and Rix, G., 2011. Damage Patterns in Port-au-Prince during the 2010 Haiti Earthquake, *Earthquake Spectra*, 27, S117–S136.
- Richards, J.A., 1999, Remote Sensing Digital Image Analysis, Springer-Verlag, Berlin, p. 240.
- Riley, S. J., DeGloria S. D., and Elliot R., 1999. A terrain roughness index that quantifies topographic heterogeneity, *Intermountain Journal of Sciences* 5, 23–27.
- Robertson, P. K., and Wride, C. E. (1998). Evaluating cyclic liquefaction potential using the cone penetration test. *Canadian Geotechnical Journal*, 35(3), 442-459.
- Saito, K., Spence, R., and de C Foley, T. A. (2005). Visual damage assessment using high-resolution satellite images following the 2003 Bam, Iran, earthquake. *Earthquake Spectra*, 21 (S1), 309-318.
- Seed, H. B., and Idriss, I. M. (1971). Simplified procedure for evaluating soil liquefaction potential. *J Soil Mech found Div ASCE*, 97(SM9), 1249-73.
- Shahi, Kaveh and Mohd Shafri, Helmi Zulhaidi and Taherzadeh, Ebrahim (2014) A novel spectral index for automatic shadow detection in urban mapping based on WorldView-2 satellite imagery. *International Journal of Computer, Control, Quantum and Information Engineering*, 8 (10). 1642-1645.
- Silva M.P.S., G. Câmara, M.I.S. Escada and R. Souza. (2008) Remote Sensing Image Mining: Detecting Agents of Land Use Change in Tropical Forest Areas. *Int. Journal of Remote Sensing*, 29, 16, 4803-4822.



- Singh, A., 1989, Digital change detection techniques using remotely-sensed data. *International Journal of Remote Sensing*, 10, 989–1003.
- Strahler, A. N., 1952. Hypsometric (area-altitude) analysis of erosional topology, *Geol. Soc. Am. Bull.* **63**, 1117–1142.
- Swets, J. A., 1973. Relative operating characteristic in psychology, *Science* **182**, 990–1000.
- Singh, R. P., S. Bhoi, and A.K. Sahoo (2002). Changes observed in land and ocean after Gujarat earthquake of 26 January 2001 using IRS data, *Int. J. Rem. Sens.* 23, 3123-3128.
- Stewart, J. P., J. D. Bray, R. B. Seed, and N. Sitar, editors (1994). Preliminary report on the principal geotechnical aspects of the January 17, 1994 Northridge earthquake, Rpt. No. UCB/EERC-94/08, Earthquake Engineering Research Center, University of California.
- Stewart, J. P., R. B. Seed, and J. D. Bray (1996). Incidents of ground failure from the 1994 Northridge earthquake. *Bull. Seism. Soc. Am.*, 86(1B), S300-S318.
- Tarboton, D. G., Bras R. L., and Rodriguez-Iturbe I., 1991. On the extraction of channel networks from digital elevation data, *Hydrol. Processes*, 5, 81–100.
- Thompson, E. M., D. J. Wald, K. Allstadt and M. Hearne (2016). Combining case history observations with different completeness levels in empirical ground-failure models, *Seismol. Res. Lett.*, 87, 2B, 578.
- Tinsley, J. C., III, J. A. Egan, R. E. Kayen, M. J. Bennett, A. Kropp, and T. L. Holzer (1998). Appendix: Maps and descriptions of liquefaction and associated effects: in Holzer, T.L., ed., The Loma Prieta, California, Earthquake of October 17, 1989 – Liquefaction: U.S. Geological Survey Professional Paper 1151-B
- Toida, R, Yamazaki, F. (2012) Analysis of Liquefaction Damage in Urayasu City in the 2011 Tohoku, Japan Earthquake Using Aerial Photographs
- Wakamatsu, K. (2011). Historic liquefaction sites in Japan, 745-2008, University of Tokyo Press.
- Wald, D. J., 1996. Slip history of the 1995 Kobe, Japan, earthquake determined from strong motion, teleseismic, and geodetic data, *J. Phys. Earth*, 44, 489–503.
- Wald, D. J., and T. I. Allen (2007). Topographic slope as a proxy for seismic site conditions and amplification, *Bull. Seism. Soc. Am.*, 97, 1379-1395.

- Weber P., M. Haklay, (2008). OpenStreetMap: User-Generated Street Maps, *IEEE Pervasive Computing*, 7, 12-18, October-December 2008, doi:10.1109/MPRV.2008.80
- Weiss, G. and F. Provost (2001). The effect of class distribution on classifier learning: An empirical study. Technical Report ML-TR-44, Department of Computer Science, Rutgers University.
- Werner, M., 2001. Shuttle Radar Topography Mission (SRTM), Mission overview, *J. Telecomm.*, 55, 75–79.
- Wessel, P., and W. H. F. Smith (1998). New, improved version of Generic Mapping Tools released, *Eos Trans. AGU*, 79, 579
- Wilson, M. F., B. O’Connell, C. Brown, J. C. Guinan, and A. J. Grehan (2007). Multiscale terrain analysis of multibeam bathymetry data for habitat mapping on the continental slope, *Marine Geodesy*, 30, 3-35.
- Witter, R. C., K. L. Knudsen, J. M. Sowers, C. M. Wentworth, R. D. Koehler, C. E. Randolph, S. K. Brooks, and K. D. Gans (2006). Maps of quaternary deposits and liquefaction susceptibility in the Central San Francisco Bay Region, California: U.S. Geological Survey Open-File Report 06-1037 (<http://pubs.usgs.gov/of/2006/1037/>)
- Wolf, A. F. (2012). Using WorldView-2 Vis-NIR multispectral imagery to support land mapping and feature extraction using normalized difference index ratios. *Proc. SPIE 8390, Algorithms and Technologies for Multispectral, Hyperspectral, and Ultraspectral Imagery XVIII*, 83900N.
- Worden, C. B., Wald, D. J., Allen, T. I., Lin, K., Garcia, D., and Cua, G., 2010. A revised ground-motion and intensity interpolation scheme for ShakeMap, *Bull. Seismol. Soc. Am.*, 100, 3083–3096.
- Worden, C. B., D. J. Wald, T. I. Allen, K. Lin, D. Garcia, and G. Cua (2010). A revised ground-motion and intensity interpolation scheme for ShakeMap, *Bull. Seismol. Soc. Am.*, 100, 3083–3096.
- U. S. Geological Survey (USGS), 1996. HYDRO1K Elevation Derivative Database. Earth Resources Observation and Science (EROS) Data Center (EDC), Sioux Falls, South Dakota,

USA.

Available

at

[http://eros.usgs.gov/#/Find\\_Data/Products\\_and\\_Data\\_Available/gtopo30/hydro](http://eros.usgs.gov/#/Find_Data/Products_and_Data_Available/gtopo30/hydro).

U.S. Geological Survey, the Southern California Earthquake Center, and the California Division of Mines and Geology (2000). Preliminary report on the 16 October 1999 M7.1 Hector Mine, California, earthquake, *Seismol. Res.Lett.*, 71, 11-23.

Van Den Eeckhaut, M., J. Hervás, C. Jaedicke, J. P. Malet, L. Montanarella, and F. Nadim (2012). Statistical modelling of Europe-wide landslide susceptibility using limited landslide inventory data, *Landslides*, 9, no. 3, 357-369.

Witten I. and H. Frank, Data mining: practical machine learning tools and techniques with java implementations 1999, Morgan Kaufman, San Francisco

Youd, T.L., and Hoose, S.N. (1978). Historic ground failures in northern California associated with earthquakes: U.S. Geological Survey Professional Paper, 993.

Youd, T. L., Idriss, I. M., Andrus, R. D., Arango, I., Castro, G., Christian, J. T., Dobry, R., Finn, W. D. L., Harder, L. F., Hynes, M. E., Ishihara, K., Koester, J. P., Liao, S. S. C., Marcuson, W. F., Martin, G. R., Mitchell, J. K., Moriwaki, Y., Power, M. S., Robertson, P. K., Seed, R. B., and Stokoe, K. H. 2001. Liquefaction Resistance of Soils: Summary Report from the 1996 NCEER and 1998 NCEER/NSF Workshops on Evaluation of Liquefaction Resistance of Soils”, *J. Geotech. Geoenviron. Eng.*, 127, 817–833.

Youd, T. L., and Perkins, D. M., (1978). Mapping liquefaction-induced ground failure potential, *J. Geotech. Engrg. Div.*, 104(GT4) Proceedings Paper No. 13659, 433–446.

Youd, T. L., and Perkins, D. M., 1987. Mapping of liquefaction severity index, *J. Geotech. Engrg. Div.*, 11, 1374–1392.

Youd, T. L., I. M. Idriss, R.D. Andrus, I. Arango, G. Castro, J. T. Christian, R. Dobry, W. D. L. Finn, L. F. Harder, M. E. Hynes, K. Ishihara, J. P. Koester, S. S. C. Liao, W. F. Marcuson, G. R. Martin, J. K. Mitchell, Y. Moriwaki, M. S. Power, P. K. Robertson, R. B. Seed, and K. H. Stokoe (2001). Liquefaction resistance of soils: Summary report from the 1996 NCEER and 1998 NCEER/NSF workshops on evaluation of liquefaction resistance of soils, *J. Geotech. Geoenviron. Eng.*, 127, 817–833.

- Zhu, J., L. G. Baise, and E. M. Thompson (2016). Liquefaction observations from ten earthquakes in the US, Japan, China, and Taiwan, U.S. Geological Survey data release, <http://dx.doi.org/10.5066/F7NC5ZB8>.
- Zhu, J., L. G. Baise, E. M. Thompson, and H. Magistrale (2014). Testing national and regional geospatial liquefaction models in the United States. 10th U.S. National Conference on Earthquake Engineering. 21-25 July 2014. Anchorage, Alaska.
- Zhu, J., L. G. Baise, E. M. Thompson, D. J. Wald, and K. L. Knudsen (2013). A geospatial liquefaction model for rapid response and loss estimation, *Seismol. Res.Lett.*, 84, 313.
- Zhu, J., D. Daley, L. G. Baise, E. M. Thompson, D. J. Wald, and K. L. Knudsen (2015). A geospatial liquefaction model for rapid response and loss estimation, *Earthquake Spectra*, 31, 1813-1837.